



저작자표시-비영리-변경금지 2.0 대한민국

이용자는 아래의 조건을 따르는 경우에 한하여 자유롭게

- 이 저작물을 복제, 배포, 전송, 전시, 공연 및 방송할 수 있습니다.

다음과 같은 조건을 따라야 합니다:



저작자표시. 귀하는 원저작자를 표시하여야 합니다.



비영리. 귀하는 이 저작물을 영리 목적으로 이용할 수 없습니다.



변경금지. 귀하는 이 저작물을 개작, 변형 또는 가공할 수 없습니다.

- 귀하는, 이 저작물의 재이용이나 배포의 경우, 이 저작물에 적용된 이용허락조건을 명확하게 나타내어야 합니다.
- 저작권자로부터 별도의 허가를 받으면 이러한 조건들은 적용되지 않습니다.

저작권법에 따른 이용자의 권리는 위의 내용에 의하여 영향을 받지 않습니다.

이것은 [이용허락규약\(Legal Code\)](#)을 이해하기 쉽게 요약한 것입니다.

[Disclaimer](#)

이학박사 학위논문

에너지 수확을 위한 유기 반도체 단
분자의 활용

Applications of organic semiconducting small
molecules for energy harvesting

2021년 08월

서울대학교 대학원

화학부 유기화학 전공

전 용 준

에너지 수확을 위한 유기 반도체 단분자의 활용

Applications of organic semiconducting small
molecules for energy harvesting

지도 교수 홍 종 인

이 논문을 이학박사 학위논문으로 제출함
2021년 08월

서울대학교 대학원 화학부
유기화학 전공
전 용 준

전용준의 이학박사 학위논문을 인준함
2021년 06월

위 원 장 최 태 림

부위원장 홍 종 인

위 원 이 성 훈

위 원 임 종 우

위 원 김 성 현

Abstract

Applications of organic semiconducting
small molecules for energy harvesting

Yongjun Jeon

Major in Organic Chemistry

Department of Chemistry

Seoul National University

Organic semiconducting small molecules have attracted great attention as alternative semiconductor materials because of their low production cost, easy structural modification and flexible structure compared to inorganic materials. Organic semiconductors have been applied in various fields such as photovoltaic cells, light-emitting devices, and thermoelectric devices. This thesis presents several ways to improve the energy

harvesting efficiency of organic photovoltaic cells and organic thermoelectric generators.

Part 1 provides a brief overview of the necessity of research on renewable energy, and the recent trend of renewable energy generators.

Part 2 introduces applications of organic semiconductor materials for organic photovoltaic cells. Section 1 describes a brief background knowledge of organic photovoltaic cells. In particular, the working mechanism of organic photovoltaic cells and the modulation method of each step of the mechanism are presented. Measurement method of photovoltaic cells and its analysis method are also described. Section 2 presents a study on three electron donor-electron acceptor-electron donor (D-A-D)-type compounds as electron donor materials for organic photovoltaic cells. These electron donor molecules with a push-pull structure are designed to induce broad photon absorption due to intramolecular charge transfer, and to have good intermolecular interactions due to their relatively flat structures, resulting in effective electron transfer. Section 3 presents a study

on modulating the morphology of the active layer in photovoltaic cells to enhance photon-to-current conversion efficiency by applying an electric field on the small molecule active layer. Though an electric field causes morphological changes in the active layer, however, these changes lead to phase separation in the active layer, lowering photon-to current conversion efficiency.

Part 3 is focused on the effect of hybridization of carbon nanotubes (CNTs) and organic semiconductor materials on the thermoelectric performance. Section 1 describes a brief overview of the thermoelectric effect, and the energy filtering effect which is often used for enhancing the Seebeck coefficient. Section 2 provides a study of changes in the Seebeck coefficient, electrical conductivity, and power factor by the hybridization of CNTs with organic small molecules (OSMs). We found that the morphology of organic small molecules and their interactions with CNTs have a large impact on the thermoelectric parameters of CNTs/OSMs hybrid films. In particular, mild charge transfer interactions between the CNT bundles and OSMs facilitate charge carrier transport between them, thereby showing approximately 2-fold

increase in the Seebeck coefficient and power factor of the CNTs/OSMs film compared to the CNTs/OSMs film with weaker intermolecular interactions between them. Section 3 presents a study on the effect of the bond type between CNTs and organic semiconductor molecules on the thermoelectric parameters. Thermoelectric parameters of compounds formed by the amide bond between CNTs and organic semiconductor molecules are compared with those of the mixture of CNTs and organic semiconductor molecules. Covalently bonded compounds enable controlling of the electron transfer pathway. However, the amide group between CNTs and organic semiconductor materials disturbs electron flows between CNTs and organic semiconductor materials and lowers the Seebeck coefficient with negative doping.

This study reveals that the amide bond with a relatively large electron density is not appropriate for increasing the Seebeck coefficient in covalently bonded CNTs/organic semiconductor hybrid materials.

Keywords : Energy harvesting, Thermoelectric generators,
Photovoltaic cells, Organic semiconductor

Student Number : 2011-20304

Contents

Part 1. Introduction.....	1
1.1 The trend of global energy consumption...	2
1.2 Renewable energy	5
Part 2. Organic photovoltaics	13
2.1 Photovoltaic cells	14
2.1.1 The photovoltaic effect in the organic solar cell	18
2.1.2 Measurement of the photovoltaic effect...	25
2.2 Vacuum-depositable thiophene and benzothiadiazole based donor materials for organic solar cells.....	37
2.2.1 Introduction.....	37
2.2.2 Experimental methods.....	39
2.2.3 Results and discussion	46
2.2.4 Conclusion.....	57
2.2.5 References and notes	58

2.3	Electric field assisted molecular ordering for solution-processable organic solar cells.....	61
2.3.1	Introduction.....	61
2.3.2	Experimental methods.....	63
2.3.3	Results and discussion	71
2.3.4	Conclusion.....	77
2.3.5	References and notes.....	77
Part 3.	Organic thermoelectrics.....	78
3.1	Basic theories for the thermoelectric.....	79
3.1.1	Thermoelectric effect	87
3.1.2	Energy filtering effect.....	96
3.1.3	Organic thermoelectric generators.....	100
3.2	Twisted small organic molecules for high thermoelectric performance of single-walled carbon nanotubes/small organic molecule hybrids through mild charge transfer interactions	103
3.2.1	Introduction.....	103
3.2.2	Experimental methods.....	106
3.2.3	Results and discussion	115
3.2.4	Conclusion.....	139

3.2.5	References and notes	140
3.3	Effect of covalent functionalizing on CNT surface in thermoelectric effect.....	148
3.3.1	Introduction.....	148
3.3.2	Experimental methods.....	150
3.3.3	Results and discussion	155
3.3.4	Conclusion.....	159
3.3.5	References and notes	160
국문 초록		163

Part 1. Introduction

1.1 The trend of global energy consumption

Humanity has been using fire since ancient times. Humanity has overcome numerous environmental problems by using fire. However, only two centuries ago, it was not until the 1st industrial revolution that humanity began to convert the heat (fire) into other energy types. In the 1st industrial revolution, the heat converted only into mechanical energy. Moreover, in the early 20th century, with the invention of commercial power plants and electric motors, humanity began to take advantage of a new type of energy called electricity. Due to the advantages of electricity compared to traditional biomass, such as ease of transportation, convertibility, and storage, electricity has become a major energy source in daily life. Since then, energy consumption has gradually increased until the information and communication industries emerged in the 1950s.

As shown in **Figure 1.1.1**, Global energy consumption, which doubled from 12,101 TWh in 1900 to 27,972 TWh in 1950, quadrupled from 27,972 TWh in 1950 to 112,265 TWh in 2000.

Enormously, in the same period, global electricity consumption increased by 500%, from 2560 TWh in 1950 to 15,555 TWh in 2000. Moreover, from 2000 to 2019, global energy consumption is increased by 40%, and in the same period, electricity production is increased by 74%. It means that global electricity demand is increased more than other energy sources. Primarily, considering the most amount of oil is used for the operation of combustion engines, electricity becomes the most familiar energy type for daily life in just one century. As per the report from International Energy Outlook 2019 (IEOP2019), this dramatic increasing trend in global energy consumption will grow by nearly 50% between 2019 and 2050.¹ Humanity predicts that if this trend continues, fossil fuels will run out in the next few decades. This prediction makes attention to the development of renewable energy sources

¹ “International energy outlook 2020”. Published online at eia.gov. Retrieved from: ‘<https://www.eia.gov/outlooks/ieo/pdf/ieo2020.pdf>’ [Online Resource]

and energy recycling, like solar cells, wind power, etc. Fortunately, global energy resource reserves continue to grow due to advances in technology and further exploration. However, one of these days, reserves of fossil fuel will run out. In preparation for that occasion, energy recycling technology is needed to increase the efficiency of the harvesting of renewable energy and the use of energy.

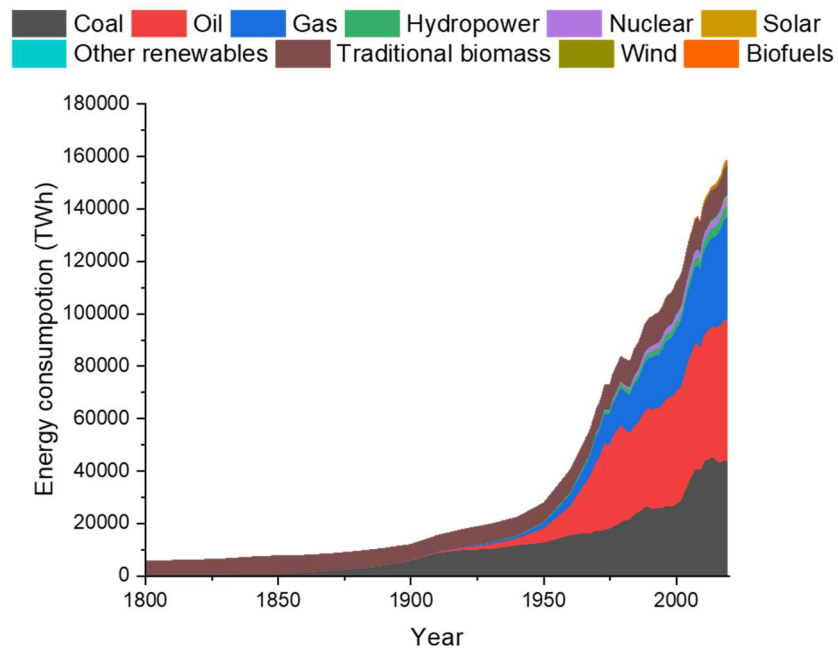


Figure 1.1.1 Global energy consumption trend colored by resource type.²

² “Energy consumption by source, World”. Published online at

1.2 Renewable energy

As mentioned in the previous section, the steep increment of global energy consumption and its prediction for upcoming decades make attention to renewable energy likes solar cells and wind power. In this section, the type of renewable energies and their basics will be described.

In human history, the most traditional renewable energy resources are water and wind. For thousands of years before the invention of electricity, humanity used wind power and waterpower by converting them into mechanical forces via windmills and watermills. Recently, humanity used them for producing electricity by wind and water power generation, not for mechanical power.

OurWorldInData.org. Retrieved from:
'<https://ourworldindata.org/grapher/energy-consumption-by-source-and-region>' [Online Resource]

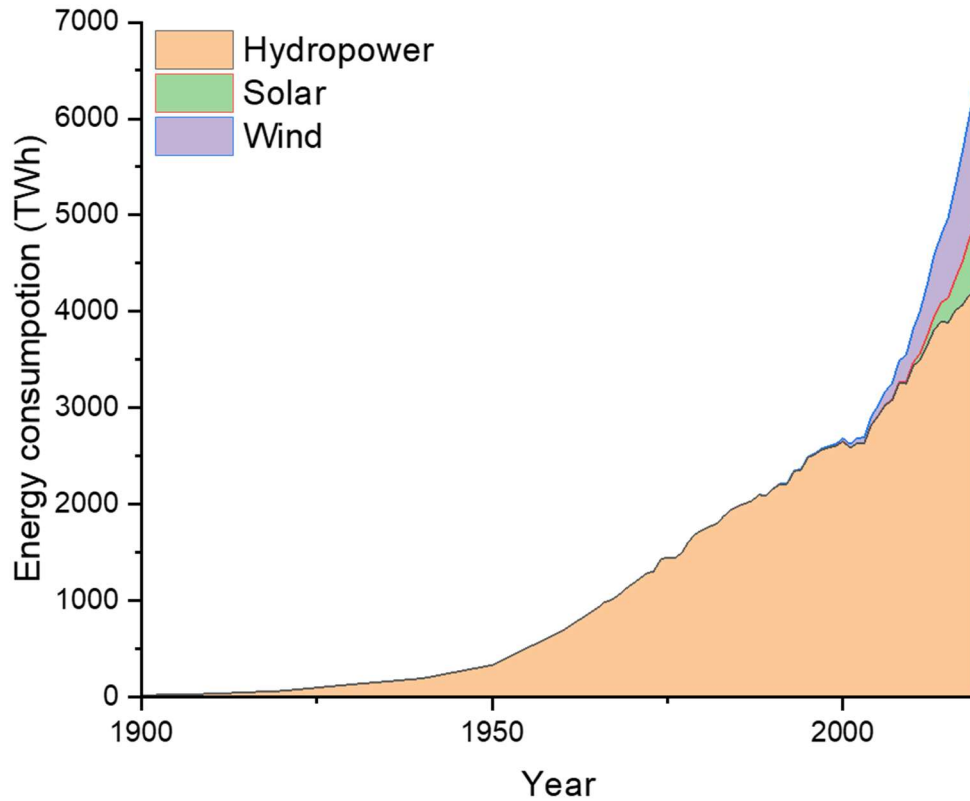


Figure 1.2.1 Global trend of major renewable energy consumption³

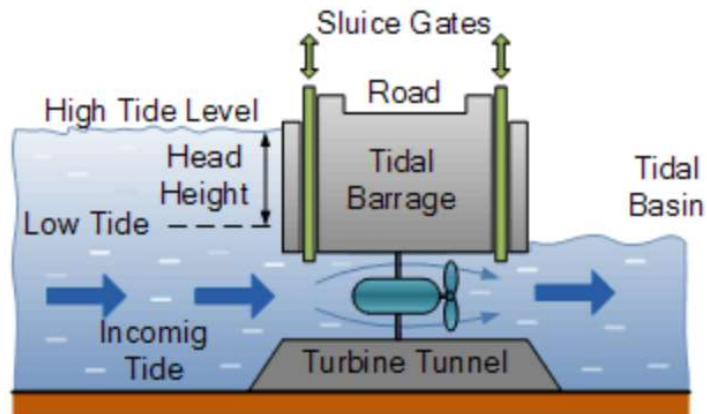
Figure 1.2.1 shows the global trend of renewable energy consumption. Water power is the primary energy source in

³ “Energy consumption by source, World”. Published online at OurWorldInData.org. Retrieved from: ‘<https://ourworldindata.org/grapher/energy-consumption-by-source-and-region>’ [Online Resource]

renewable energies (60%). Wind power occupies 20%, and solar energy occupies 11%.

Water power generators (water turbines, hydroelectric generators) can be placed only following the water flows because water turbines convert the potential energy and kinetic energy of water into electrical power. Therefore, water turbines have geographical limitations. However, unlike the wind turbine, a water turbine can store redundant energy as the potential energy of water with a reservoir like a dam. Therefore, many numbers of water turbines are designed for multipurpose. Also, there are some particular types of water power generators, called tidal power generators and wave power generators.

Tidal Barrage Flood Generation



Tidal Barrage Ebb Generation

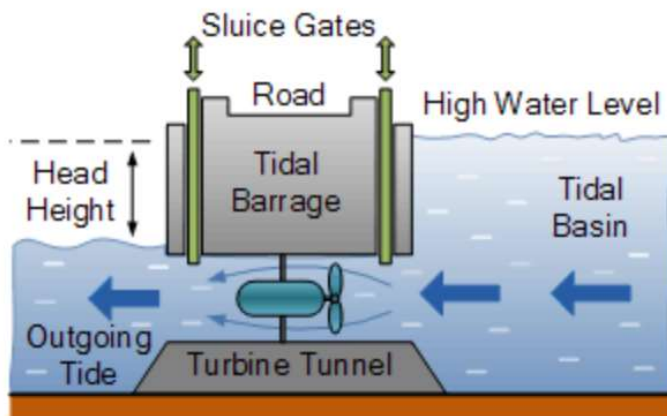


Figure 1.2.2 Schematic illustration of tidal power generator⁴

⁴ “How does tidal energy work”. Published online at www.ourworldofenergy.com. Retrieved from: ‘<https://www.ourworldofenergy.com/vignettes.php?type=other-renewables-energy&id=9>’ [Online Resource]

Tidal power generators produce electrical power using tidal power, which is made by the revolution of the moon. **(Figure 1.2.2)** Unlike traditional water power, tidal energy cannot be stored, but its periodicity covers this disadvantage. However, tidal power generators have a significant problem with its geographical requirements. Tidal power generators require tidal flats for using tidal. It is a very rare terrain, and it is of great environmental importance. Installation of the tidal generator causes severe destruction of ecosystems on the tidal flat.

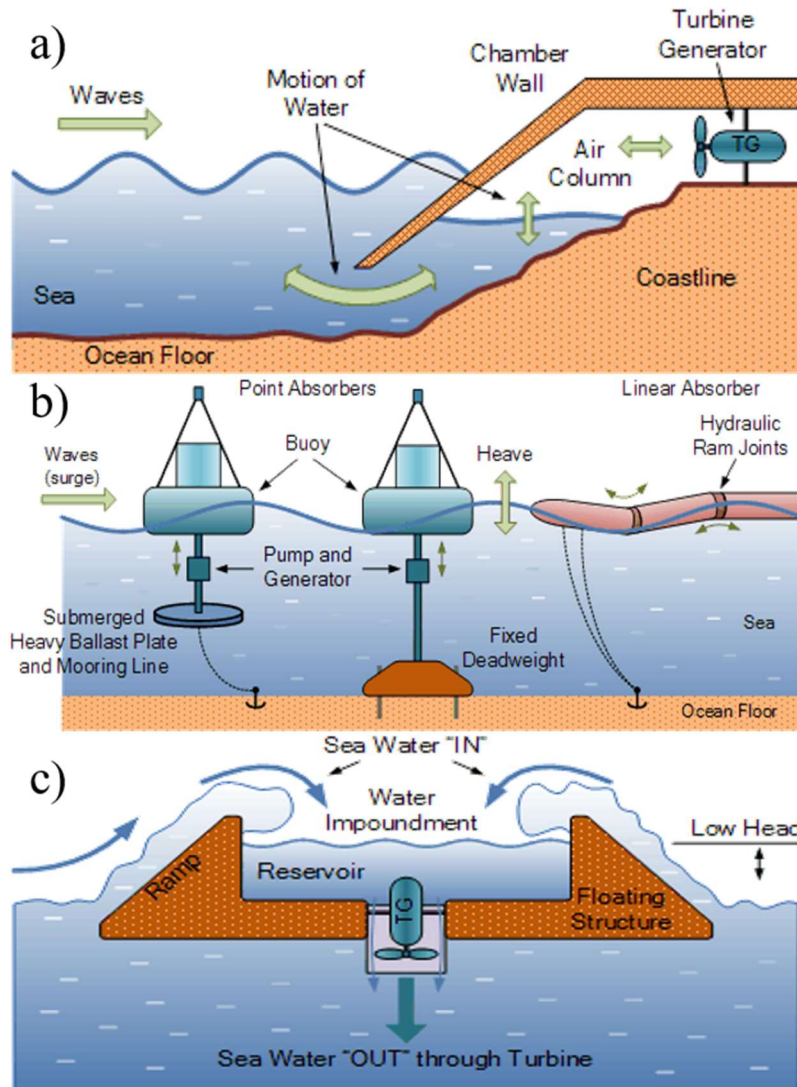


Figure 1.2.3 Schematic illustration of wave power generators⁵

⁵ “Wave energy devices”. Published online at www.alternative-energy-tutorials.com. Retrieved from: ‘<https://www.alternative-energy-tutorials.com/wave-energy/wave-energy-devices.html>’
[Online Resource]

a) Oscillating water column type. b) Wave profile type. c) Wave capture type.

Wave power generators convert upper and lower movement caused by a wave into electrical power. It is the most recently proposed technology (the first test was performed in 2003)⁶ Wave power generators are proposed in three types. **(Figure 1.2.3)** The oscillating water column type uses the airflow induced by the wave. Wave profile type uses a wave as the mechanical energy source. Wave capture type is the application of traditional water turbines.

Wind power generators (wind turbines) convert wind power to electrical power. Therefore, wind turbines can be placed anywhere because wind presents anywhere. A single wind turbine requires a small space. However, for producing massive electrical power, wind turbines require large spatial intervals between each other. It makes the wind power plant occupies a large scale of space.

⁶ “The european marine energy centre ltd”. Published online at www.emec.org.uk. Retrieved from: ‘<http://www.emec.org.uk/about-us/>’ [Online Resource]

Solar energy is an upcoming candidate for renewable energy. Solar energy is converted light, which comes from the sun, into electrical power directly using photovoltaic effect or indirectly via solar thermal energy. Solar energy does not cause noise pollution or destruction of rare environments. Also, renewable energies, which are mentioned, eventually originated from the sun. It means solar energy is practically infinite. If humanity becomes to use solar energy as a primary energy source, humanity will be free from the concern of the depletion of energy.

Part 2. Organic photovoltaics

2.1 Photovoltaic cells

Solar cells are one of the electric power generation methods which do not use mechanical power mediating. Therefore, it does not use the turbine for producing electric power and occupy much smaller space than other electric power generators through mechanical force. Furthermore, it does not use fossil fuels for operating. For these reasons, solar cells have been getting attention since several decades ago. Especially, energy sources, one of the characteristics of solar power, make it useful in unusual cases like challenging to transport the resources needed for power generation.

In **Figure 2.1.2**, a brief history of organic solar cells is presented. The origin of solar cells is the discovery of the photovoltaic effect. Since then, there is no notable discovery or development of solar cells before 1954. In 1954, "Bell Labs Innovations" reported the solar cell using silicon, which shows nearly 4% conversion efficiency.



Figure 2.1.1 Solar panels attached to the satellite (Skylab 4)⁷

After silicon-based solar cells achieved their conversion efficiency of about 11%, solar cells get attention as an alternative electric power generator. In the case of organic materials, Ching Wan Tang makes a breakthrough by developing a two-layer structure called a bilayer structure or planar heterojunction structure.⁸ This separated structure helps the separation of the exciton, resulting in significant enhancement of photoconversion

⁷ Published online at nasa.gov. Retrieved from:
'<https://www.nasa.gov/content/overhead-view-of-skylab-from-orbit>' [Online Resource]

⁸ Tang, C. W. Two-layer organic photovoltaic cell. *Appl Phys Lett* 48, 183–185 (1986).

efficiency. After this notable discovery, materials that are used in organic solar cells have one of two roles, donor material, which absorbs light and produces exciton or acceptor, which accelerates the separation of the exciton. Moreover, in 1995, N. C. Sariciftci reported C₆₀ as an excellent acceptor material in organic solar cells.⁹

⁹ Sariciftci, N. S. Role of Buckminsterfullerene, C₆₀, in organic photoelectric devices. *Prog Quant Electron* 19, 131–159 (1995).

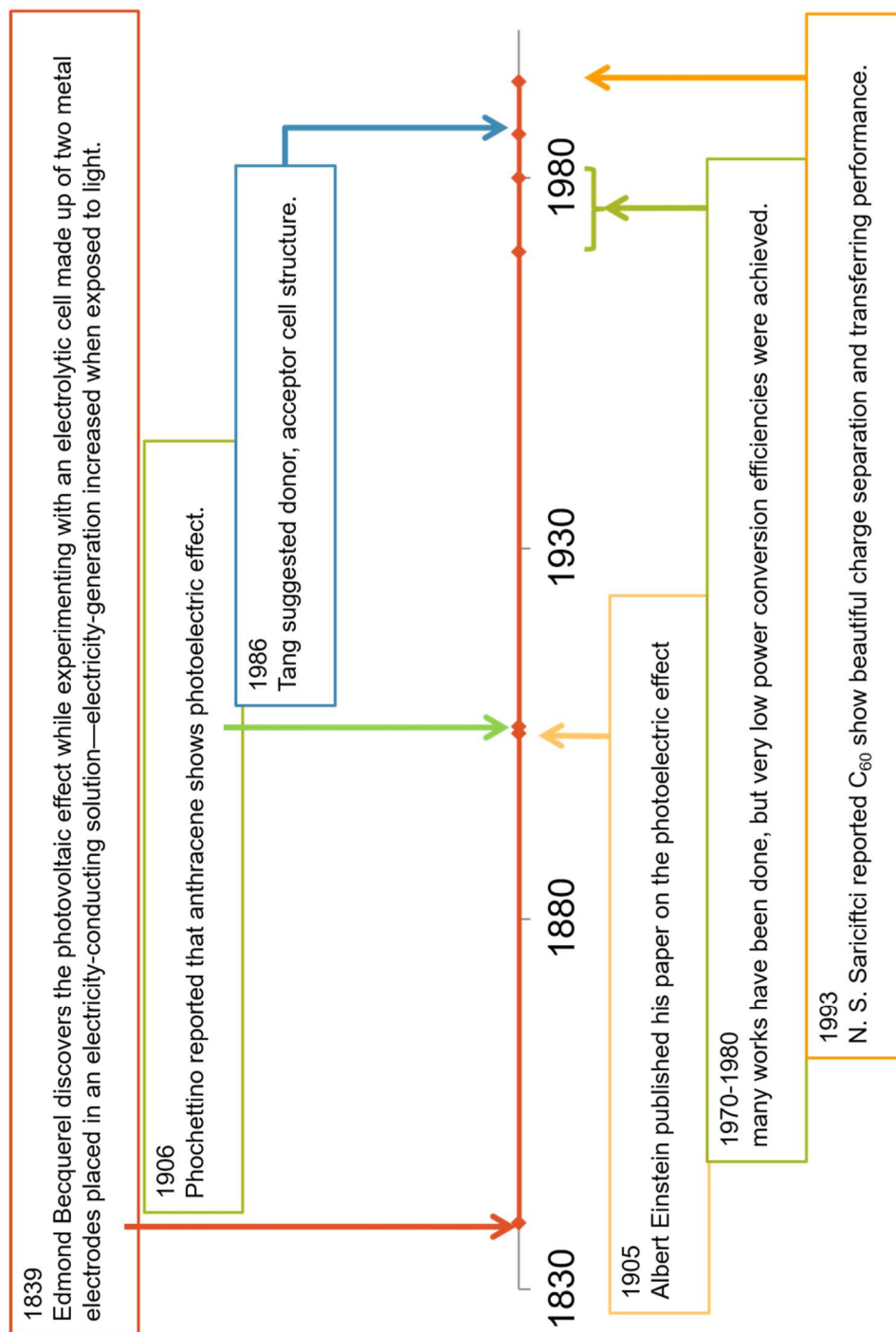


Figure 2.1.2 Brief history of organic solar cells

2.1.1 The photovoltaic effect in the organic solar cell

Solar cells produce electric power based on the photovoltaic effect. The photovoltaic effect is closed to the photoelectric effect, which was explained by Albert Einstein. The photovoltaic effect was reported by Edmond Becquerel in 1839 at first. He reported an increment of electric current with solar radiation. Like this, the photovoltaic effect means a phenomenon that produces an electromotive force from the radiation of light. The difference between the photoelectric effect and photovoltaic effect is the behavior of an electron in the material which absorbs light. In the photoelectric effect, absorbed light, a photon, expels an electron. However, in the photovoltaic effect, absorbed light induces an excited state of the material. If an electron in the excited state is transferred to other molecules, an electron exists in a higher energy state than other electrons. This electron in the higher energy state starts to conduct the circuit to get a more stable state following the thermodynamics. This electron flow is called photo-current, and the force which makes electron flow is called photo-electromotive

force (photo-potential). The photovoltaic effect consists of four steps of the mechanism. (**Figure 2.1.3**)

The first step is **Absorption**. (**Figure 2.1.3a**) In this step, photo-active material absorbs light(photon) and forms an excited state called an exciton. Absorption of light is occurring prominently in the electron donor material. Therefore, the absorption spectra and extinction coefficient of the electron donor material significantly affect this step. The more photons are absorbed, the more advantageous. Due to this reason, electron donor materials are required to have a wide absorption wavelength band and a high absorbance coefficient.

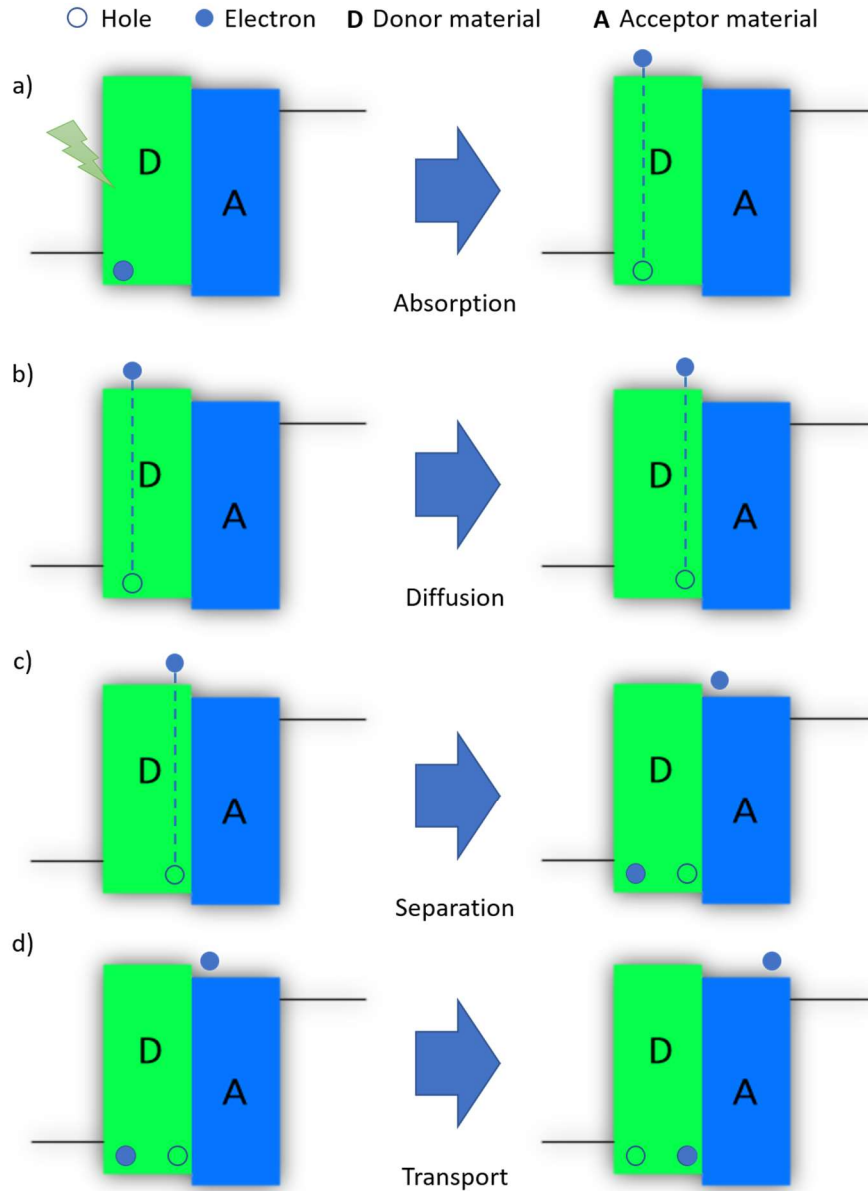


Figure 2.1.3 Four steps of the mechanism of the organic photovoltaic effect

Figure 2.1.4 shows that a high energy photon with a short wavelength exists less than a low energy photon, which has a long

wavelength. Photons present from 300 nm to 550 nm (half of the range in wavelength) have nearly half (48.6%) of energy compared to total photon energy from 300 nm to 800 nm. However, they occupy 38.8% of the total number of photons from 300 nm to 800 nm. Moreover, in the photon energy-based plot, this difference is more significant. From 4.14 eV to 2.69 eV (half of the range in energy, from 300 nm to 435 nm), photons in this range have 28.6% of total energy and occupy 21.2% of the total number. Because one photon only available to convert one electron, absorbing low energy photons is more efficient than high energy photons.

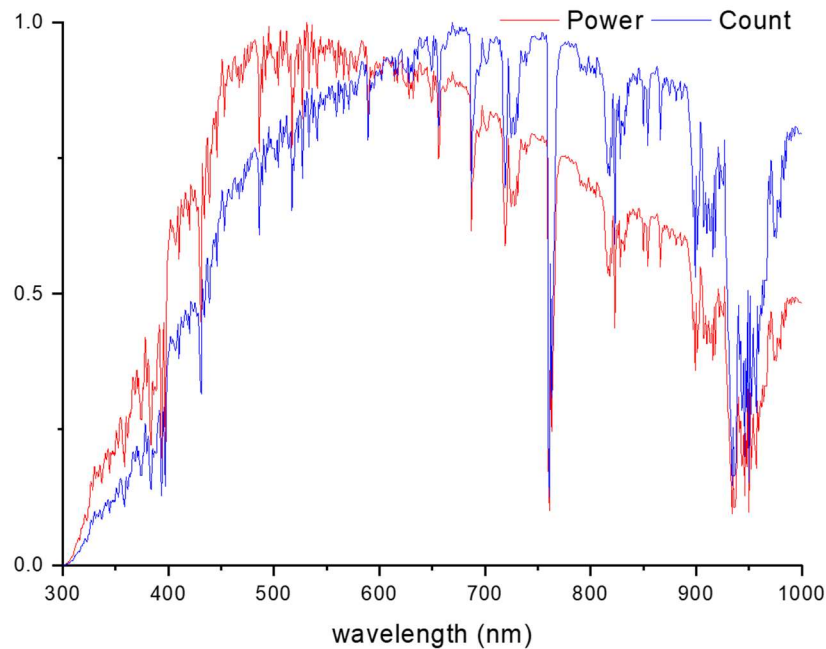


Figure 2.1.4 Normalized photon distribution of AM1.5G in the energy unit and count unit. This spectrum is drawn based on the public solar spectrum.¹⁰ The solid red line means the sum of photon energy varies by wavelength. The solid blue line means the sum of photon count varies by wavelength.

The second step is exciton **Diffusion**. (Figure 2.1.3b) In this step, an excited state formed the previous step, Absorption, moves to

¹⁰ Published online at www.nrel.gov. Retrieved from: ‘<https://www.pveducation.org/pvcdrom/appendices/standard-solar-spectra>’ [Online Resource]

the interface of electron donor and electron acceptor material. Transport of an excited state can occur through two mechanisms, Dexter electron transfer and Förster energy transfer. This transport occurred with no directional driving force. Due to this random walk trait, many of the produced excitons which do not reach the interface of electron donor and electron acceptor material stabilize to their ground state. A planar heterojunction structure, which is reported by Ching W. Tang, overcomes this phenomenon. Moreover, the bulk-heterojunction structure makes the photo-current conversion efficiency of organic photovoltaic cells higher.

(Figure 2.1.5)

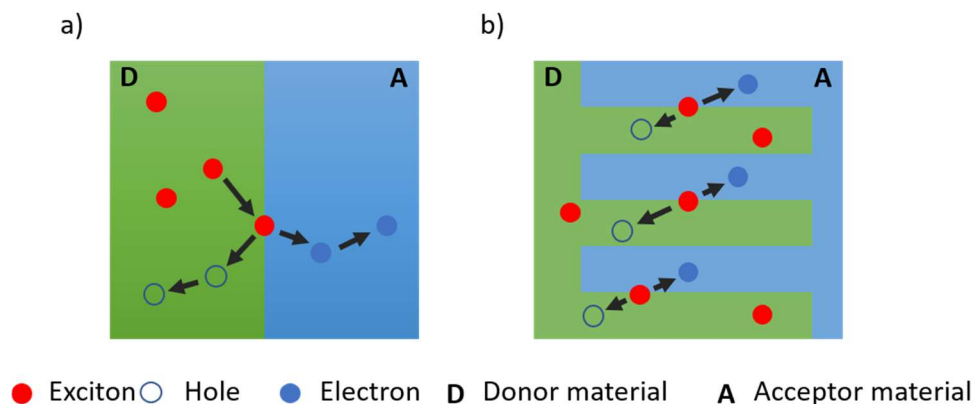


Figure 2.1.5 Schematic illustration of the diffusion and separation of exciton in a) planar heterojunction and b) bulk

heterojunction.

The third step is **Separation** (exciton dissociation). (**Figure 2.1.3c**) Diffused excitons to an interface of the electron donor and electron acceptor material are separated into a hole and an electron. In a detailed, excited electron in the electron donor material's LUMO state is transferred to the electron acceptor material's LUMO state. Then the donor material has a positive charge, and the acceptor material has a negative charge. At this point, the donor material, which becomes a positive ion, is called a hole. The acceptor material, which becomes a negative ion, is called an electron. (Actually, the hole is not a real particle. It just behaves like an electron, but its direction of movement is opposite to an electron. Also, the flow of the hole is in the same direction as the electric current. Therefore, a hole is used to explain electron flows in semiconductors easier.)

The last step is **Transport**. (**Figure 2.1.3d**) The separated hole and electron from the exciton in the previous 3rd step start to move to each electrode. The hole is heading to the anode, and the

electron is heading to the cathode. The movement of the hole and electron are affected by the electric field, which is made by two different electrodes, such as the Alumina electrode and the indium tin oxide electrode. In this step, the flow controlling of charge carriers (hole and electron) is important. If they collide with each other, (hole and electron) restore to exciton or stabilize the ground state. This phenomenon is called recombination. It is one of the major factors of lowering the efficiency of photovoltaic cells with inefficient exciton dissociation.

2.1.2 Measurement of the photovoltaic effect

To measure the efficiency of photovoltaic cells, we need a solar simulator to simulate the solar ray spectrum. The solar simulator makes light using black body radiation similar to the sun does. We can simulate the solar radiation with this device called solar simulator and modulate incident power to meet AM 1.5G condition. AM 1.5G means "Air Mass 1.5 Global". This specified standard named AM 1.5G defines the incident light spectrum and

its power per area, which can be absorbed by photovoltaic cells. This standard about spectrum and power per area equivalent to that of a solar zenith angle 48.2° . Especially, G(global) means that it includes both direct and diffuse radiation. Therefore, we modulate the power of incident light to 100 mW cm^{-2} before measuring the efficiency of photovoltaic cells.

After confirming the incident light condition, we apply an electric potential with a source meter against an electric potential produced from photovoltaic cells by the photovoltaic effect. And then, we gather an electrical current that varies to an electric potential applied with a source meter. We can get a voltage-current density curve as a result of this measurement, which is called the J-V curve. (J means electric current density). (**Figure 2.1.6**)

In Figure 2.1.6, the x-axis intercept of the lower placed curve, which means a curve for an illuminated condition, is called open circuit potential (V_{oc}). The y-axis intercept of that is called short circuit current density (J_{sc}). V_{oc} means that the maximum photo-potential which photovoltaic cells can produce. J_{sc} means that the maximum photo-current density which photovoltaic cells can

produce. An imaginary square, which is made by V_{oc} and J_{sc} , is the ideal power output of photovoltaic cells. The real biggest square made following the J-V curve is the real maximum power output that photovoltaic cells can produce. The ratio between the real maximum power output and ideal power output is called the fill factor. The fill factor is closed to 0.25 when the photovoltaic cells have no diode's trait results from the Schottky barrier. And the fill factor is closed to 1 when it works as ideal photovoltaic cells, which have infinite shunt resistance and zero series resistance.

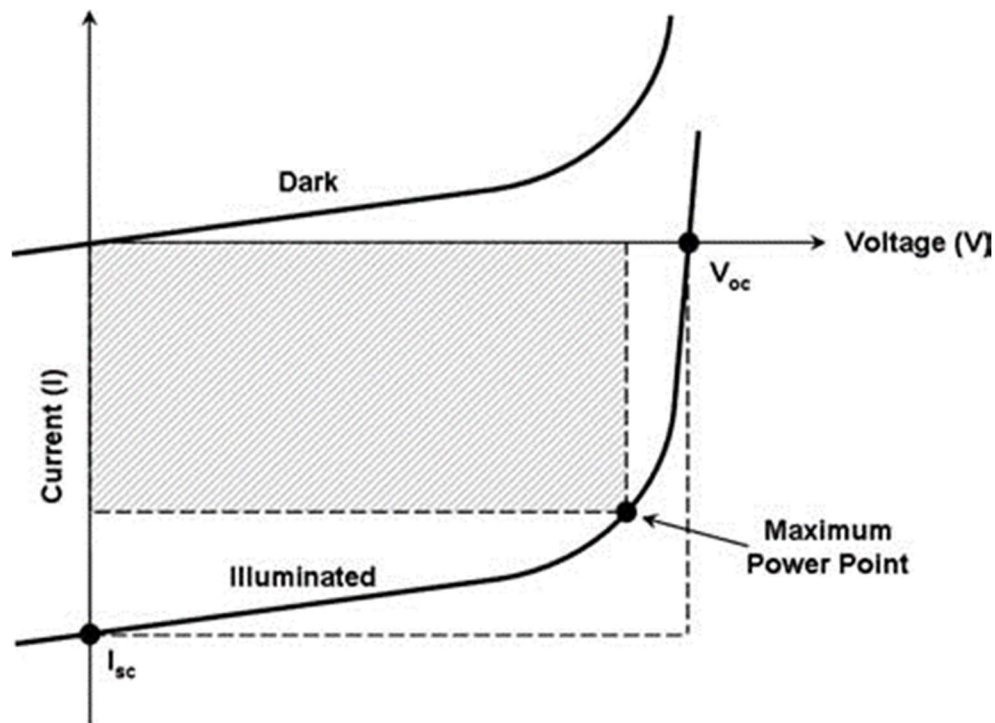


Figure 2.1.6 Graph of current versus voltage for photovoltaic

devices. The figure shows how the device characteristics change upon illumination. Key points on the graph are also indicated.¹¹

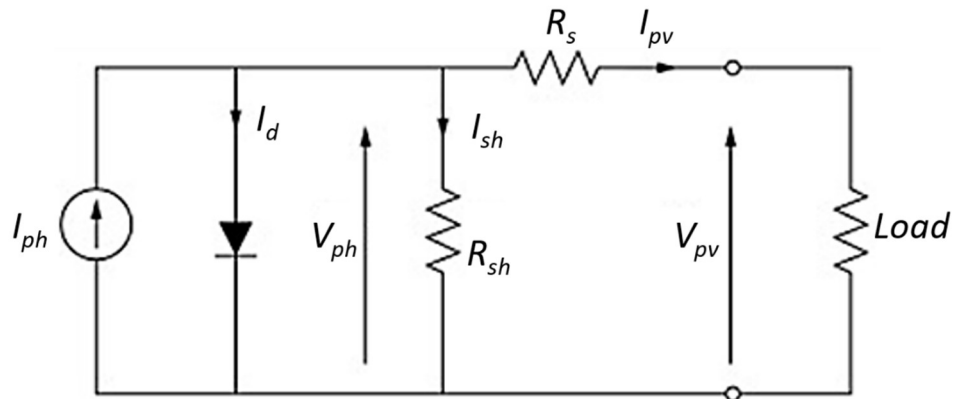


Figure 2.1.7 Single-diode electrical PV module equivalent circuit¹²

Figure 2.1.7 shows an equivalent circuit of a solar cell. In this equivalent circuit, R_s is the series resistance (Ω). R_{sh} is the shunt

¹¹ Benanti, T. L. & Venkataraman, D. Organic Solar Cells: An Overview Focusing on Active Layer Morphology. *Photosynth Res* **87**, 73–81 (2006)

¹² Rosa-Clot, M. & Tina, G. M. Submerged and Floating Photovoltaic Systems. 33–64 (2018) doi:10.1016/b978-0-12-812149-8.00003-x

resistance or parallel resistance (Ω). I_{ph} is a photogenerated current (A). I_d is internal diode current (A). I_{sh} is the shunt current, which means the current leakage. I_{pv} is measured current from outside of the photovoltaic cell. V_{pv} is measured current from outside of the photovoltaic cell. V_{ph} (V_d) is measured current from outside of the photovoltaic cell.

Following the equivalent circuit in **Figure 2.1.7**, we can define I_{ph} and V_{ph} , which cannot be measured directly.

$$I_{pv} + I_{sh} + I_d = I_{ph}$$

$$V_{pv} + I_{pv} \times R_s = V_{ph}$$

From several parameters in these equations, we can only measure I_{pv} and V_{pv} directly. I_d can be calculated from I_s , which means reverse saturation current in diode and measured directly in the dark-current condition. (J-V curve measurement without incident light) I_d is defined as the following equation.

$$I_d = I_0 \left(e^{\frac{V_{ph}}{nV_T}} - 1 \right)$$

V_T is the thermal voltage, which is defined as $V_T = \frac{k_B T}{q}$, V_T is nearly 0.025 V at room temperature.

In photovoltaic cells, the current diverted through the diode is a reverse flow. Therefore, I_d is the same as the I_s . In most cases, this I_d (I_s) has a minimal value than other current values, and it is ignorable. The following equation shows relationships between the photogenerated current (I_{ph}) and series resistance (R_s) and shunt resistance (R_{sh}) based on the measurable current (I_{pv}) and potential (V_{pv}).

$$I_{ph} = I_{sh} + I_{pv}$$

$$\begin{aligned} I_{ph} &= \frac{V_{ph}}{R_{Tot}} = \frac{V_{ph}}{\left(\frac{1}{R_s + \frac{V_{pv}}{I_{pv}}} + \frac{1}{R_{sh}} \right)} = \frac{V_{pv} + R_s \times I_{pv}}{\left(\frac{1}{R_s + \frac{V_{pv}}{I_{pv}}} + \frac{1}{R_{sh}} \right)} \\ &= (V_{pv} + R_s \times I_{pv}) \times \left(\frac{I_{pv}}{R_s \times I_{pv} + V_{pv}} + \frac{1}{R_{sh}} \right) \\ &= I_{pv} + \frac{R_s \times I_{pv} + V_{pv}}{R_{sh}} \end{aligned}$$

Based on this result, we can extract R_s and R_{sh} as the following equation with some assumptions.

At close to V_{oc} , we can ignore R_s term in V_{ph} and V_{pv} , due to load resistance is exclusively larger than R_s .

$$I_{pv} = I_{ph} - \frac{R_s \times I_{pv} + V_{pv}}{R_{sh}}$$

At close to the V_{oc} , I_{pv} is nearly zero. Therefore, we can assume that I_{pv} equal to I_{ph} .

Let

$$I_{pv} = I_{ph}$$

$$\frac{R_s \times I_{pv} + V_{pv}}{R_{sh}} = 0$$

$$R_s \times I_{pv} + V_{pv} = 0$$

$$-R_s \times I_{pv} = V_{pv}$$

$$I_{pv} = -\frac{1}{R_s} V_{pv}$$

Consequently, the slope of V_{pv} - I_{pv} (J-V curve) at close to the V_{oc} is $-\frac{1}{R_s}$. Similar to this, we can define R_{sh} at close to the J_{sc} .

$$I_{pv} = I_{ph} - \frac{R_s \times I_{pv} + V_{pv}}{R_{sh}}$$

$$I_{pv} = I_{ph} - \frac{R_s}{R_{sh}} I_{pv} - \frac{1}{R_{sh}} V_{pv}$$

$$I_{pv} + \frac{R_s}{R_{sh}} I_{pv} = I_{ph} - \frac{1}{R_{sh}} V_{pv}$$

$$\left(1 + \frac{R_s}{R_{sh}}\right) I_{pv} = -\frac{1}{R_{sh}} V_{pv} + I_{ph}$$

$$(R_{sh} + R_s) I_{pv} = -V_{pv} + R_{sh} \times I_{ph}$$

$$I_{pv} = -\frac{1}{(R_{sh} + R_s)} V_{pv} + \frac{R_{sh}}{(R_{sh} + R_s)} I_{ph}$$

Consequently, the slope of V_{pv} - I_{pv} (J-V curve) at close to the J_{sc} is $-\frac{1}{(R_{sh}+R_s)}$.

According to this theorem, we can explain the J-V curve. A steep slope at J_{sc} implies that there are some problems in separation and transport steps. A gentle slope at V_{oc} implies that there are some problems in the transport step.

There is one more thing to evaluate the photovoltaic cell. It is called the incident photon to current efficiency (IPCE). **IPCE** shows relationships between absorbed photon counts and converted charge carrier counts. Every photon has different energy according to its wavelength. Also, it makes a difference in photo-

induced excitation of material or transporting mechanism. Therefore, examining what photon is converted to a charge carrier is important. Measuring IPCE is similar to measuring the photoconversion efficiency of the photovoltaic cell. Differences in IPCE are the secondary incident light source and usage of the monochromated light source, not the full range.

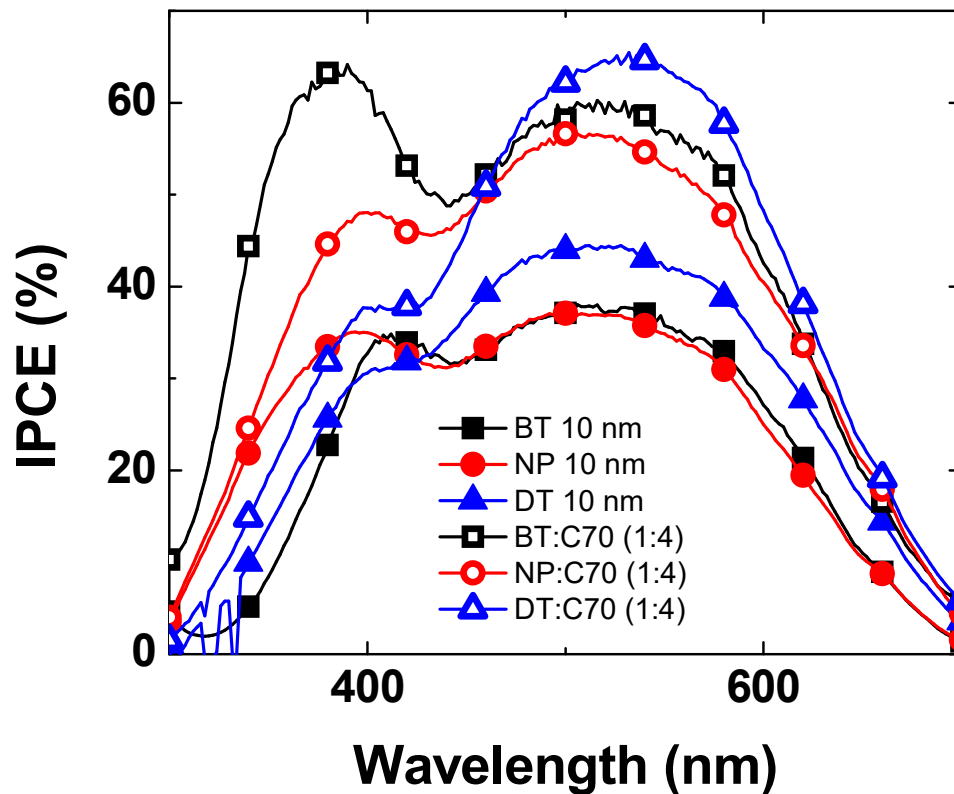


Figure 2.1.8 IPCE data for PHJ devices (active layer thickness: 10 nm) and BHJ devices (donor:C₇₀=1:4)

To calculate how many photons are converted into charge carriers, we must know how many photons are irradiated. We can calculate the irradiated light's power on the photovoltaic cell using a reference light spectrum of a light source like **Figure 2.1.3**.

According to the Planck-Einstein relation, the energy that a photon has is expressed as the following equation.

$$E = h\nu$$

E is the energy of a photon (eV), h is the Planck constant. ($4.135667696 \times 10^{-15}$ eV s⁻¹)

The frequency of a photon (ν) can be expressed with its wavelength.

$$\nu = \frac{C}{\lambda}$$

C is the speed of light (m s⁻¹), λ is the wavelength of a photon.

With this relation, the Planck-Einstein relation can be written in the following equation.

$$E = h \frac{C}{\lambda}$$

$$E = \frac{1239.8 \text{ eV} \cdot \text{nm}}{\lambda} = \frac{1.9864 \times 10^{-16} \text{ J} \cdot \text{nm}}{\lambda}$$

Only one photon can be converted into one charge carrier. Therefore, the maximum photo-current equal to irradiated photon counts, not related to the energy of the photon. In the measurement of the incident photon to current efficiency, the irradiated photon is monochromated, and we can calculate photon counts with specific wavelengths using a reference light spectrum of a light source like as the following equation.

$$\begin{aligned}
 IPCE(\lambda) &= \frac{\frac{I_{ph}}{1.602 \times 10^{-19} C}}{\frac{1239.8 eV \cdot nm}{\lambda}} \\
 &= \frac{I_{ph}}{1.602 \times 10^{-19} C} \frac{1.9864 \times 10^{-16} J \cdot nm}{P \times \lambda} \\
 &= 1.2398 \times 10^{-3} W \cdot nm/A \times \frac{I_{ph}}{P \times \lambda}
 \end{aligned}$$

P is the power of the incident light. λ is the wavelength of the incident light. I_{ph} is the photo-current of the incident light with secondary light.

The sum of the incident photon to current efficiency is slightly larger than the photo-current conversion efficiency. It results from secondary light, which is used for helping electron flow in the

photovoltaic cell. Without this secondary light, measuring the the incident photon to current efficiency is too hard due to its insufficient charge carrier concentration to flow.

2.2 Vacuum-depositable thiophene and benzothiadiazole based donor materials for organic solar cells

2.2.1 Introduction

Organic photovoltaics (OPVs) convert solar energy to electrical energy and thus have attracted considerable interest as a possible alternative to conventional inorganic photovoltaic technologies. OPV devices have several advantages such as mechanical flexibility, easy synthesis of active layer materials, light weight, and low manufacturing cost, compared to inorganic solar cells. Because of these advantages, intensive research toward the development of OPV devices has been conducted, in spite of their lower power conversion efficiency (PCE) than inorganic solar cells.

The PCE of p-n junction OPVs can be increased by facilitating exciton diffusion and exciton dissociation which can be addressed using the BHJ structure and fullerene derivatives, respectively.¹

Current studies on OPVs are usually focused on enhancing the PCE of OPVs using new electron donor materials. One general method for enhancing PCE using organic electron donors is improving light harvesting ability, which can be generally achieved by broadening absorption ranges and increasing molar extinction coefficients. Usually, broadening absorption ranges is easier and more efficient than increasing molar extinction coefficients.

In this paper, we designed and synthesized three D-A-D type organic electron donor molecules to increase light absorption ranges, consisting of 2,1,3-benzothiadiazole as an electron withdrawing core,²⁻³ and benzothiophene, naphthalene and thiophene as electron donating terminal groups. Two thiophenes were used as spacers between the electron withdrawing core and electron donating terminal groups, because oligothiophene is widely used for organic electronics due to its good hole/electron transporting ability.⁴⁻⁶ It is well known that intramolecular charge transfer (ICT) in a D-A type molecule makes narrow HOMO/LUMO energy level gap and thus induces broad and

strong absorption with bathochromic shift in addition to its own π - π absorption band.⁷ The three donor molecules (**NP**, **BT**, **DT**) have relatively wide absorption ranges caused by ICT and good intermolecular interaction due to their relatively flat structures. BHJ OPV devices fabricated using 1:4 **DT** and C₇₀ exhibited a maximum PCE of 4.13%.

2.2.2 Experimental methods

Instruments

¹H spectra were recorded in CDCl₃ or DMSO using an Advance 300 MHz or 500 MHz Bruker spectrometer. Mass spectra were obtained using a MALDI-TOF mass spectrometer from Bruker. Elemental analysis was performed with a Carlo-Erba model EA 1112 elemental analyzer. TGA was performed with a TA instrument model Q-5000 IR. UV-Vis spectra were recorded on a Beckman DU 650 spectrophotometer. Fluorescence spectra were recorded on a Jasco FP-7500 spectrophotometer. For solid-state measurements, the materials were thermally vapor deposited onto

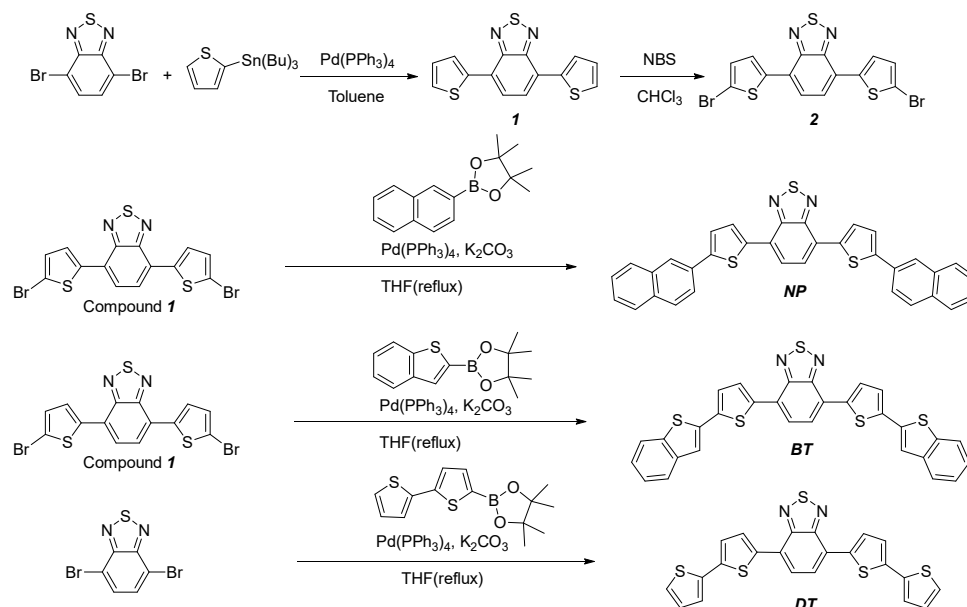
quartz plates in a vacuum chamber to form 40 nm thick films. The cyclic voltammetry (CV) apparatus used was a CH Instruments model 650B electrochemical workstation. Cyclic voltammograms were obtained at room temperature in a three-electrode cell with a working electrode (glassy carbon), a reference electrode (Ag/Ag^+ 0.01 M), and a counter electrode (Pt), in dichloromethane or dimethyl formamide containing tetrabutylammonium hexafluorophosphate (TBAPF_6 , 0.1 M) as a supporting electrolyte, at a scan rate of 100 mV/s. All potential were calibrated with the standard ferrocene/ferrocenium (Fc/Fc^+) redox couple. X-ray diffraction spectra were obtained by D8 ADVANCE with DAVINCI, BRUKER. Molecular structures at ground state and HOMO/LUMO energy levels were calculated using Gaussian 09 Rev. B01 with DFT/B3LYP method with a 6-31G basis set.

Reagents and materials

All chemicals, such as 4,7-dibromo-2,1,3-benzothiadiazole, 2-(tributylstannyl)thiophene, N-bromosuccinimide (NBS), were purchased from either Sigma-Aldrich or Toyko Chemical Industry

(TCI) and were used as received. 4,7-Bis(bromothiophen-2-yl)-2,1,3-benzothiadiazole (**1**) was synthesized according to the literature procedure.⁸

Synthesis



Scheme 2.2.1 Synthesis of BT, DT, NP

Compound 2. To a solution of **1** (410 mg, 1.36 mmol) in chloroform (30 ml), NBS (730 mg, 4.08 mmol) was added and the mixture was stirred for 12 h at room temperature. Precipitates formed were filtered by Büchner funnel to give 570 mg of **2** (yield: 91%).⁹

BT. A mixture of compound 1 (1.6 g, 3.5 mmol), 2-(benzo[b]thiophen-2-yl)-4,4,5,5-tetramethyl-1,3,2-dioxaborolane (1.6 g, 8.7 mmol), tetrakis(triphenylphosphine)palladium(0) (40 mg, 0.03 mmol) and potassium carbonate (3.4 g, 24 mmol) in THF/H₂O (100 ml/50 ml) was heated at 70 °C for 72 h. Then the reaction mixture was cooled to room temperature and vacuum filtered using Büchner funnel (yield: 1.20 g, 61%). The crude product was purified by sublimation. ¹H NMR (500 MHz, DMSO-D₆): δ (ppm) 7.40 (q, J = 8 Hz, 4H), 7.59 (s, 2H), 7.76 (s, 2H), 7.88 (d, J = 7.5 Hz, 2H), 7.91 (d, J = 8 Hz, 2H), 7.95 (d, J = 7.5 Hz, 2H), 8.17 (s, 2H). T_d: 401.92 °C. HRMS (FAB) m/z: calc. for C₃₀H₁₆N₂S₅ [M]⁺: 563.9917, found: 563.9908. Elemental Analysis calc.: C, 63.80; H, 2.86; N, 4.96; S, 28.39; found: C, 63.78; H, 2.84; N, 4.85; S, 28.46.

NP. A mixture of compound 1 (1 g, 2.2 mmol), 4,4,5,5-tetramethyl-2-(naphthalen-2-yl)-1,3,2-dioxaborolane (1 g, 5.5

mmol), tetrakis(triphenylphosphine)palladium(0) (25 mg, 0.02 mmol) and potassium carbonate (2.1 g, 15 mmol) in THF/H₂O (100 ml/50 ml) was heated at 70 °C for 72 h. Then the reaction mixture was cooled to room temperature and vacuum filtered using Büchner funnel (yield: 1.00 g, 83%). The crude product was purified by sublimation. ¹H-NMR (500 MHz, DMSO-D₆): δ (ppm) 7.55 (t, J = 18 Hz, 2H), 7.78 (s, 1H), 7.93 (d, J = 7 Hz, 2H) 8.00 (d, J = 4.5 Hz, 2H), 8.18 (s, 1H), 8.23(s, 1H), 8.29 (s, 1H). T_d: 432.87 °C. HRMS (FAB) m/z: calc. for C₃₄H₂₀N₂S₃ [M]⁺: 552.0789, found: 552.0789. Elemental Analysis calc.: C, 73.88; H, 3.65; N, 5.07; S, 17.40; found: C, 73.86; H, 3.59; N, 5.00; S, 17.49.

DT. A mixture of 4,7-dibromo-2,1,3-benzothiadiazole (100 mg, 0.34 mmol), 2,2'-bithiophene-5-boronic acid pinacol ester (250 mg, 0.85 mmol), tetrakis(triphenylphosphine)palladium(0) (20 mg, 0.02 mmol) and potassium carbonate (470 mg, 3.4 mmol) in THF/H₂O (50 ml/25 ml) was heated at 70 °C for 72 h. Then the reaction mixture was cooled to room temperature and vacuum

filtered using Büchner funnel (yield: 43 mg, 28%). The crude product was purified by sublimation. ^1H NMR (300 MHz, CDCl_3): δ (ppm) 8.07 (d, $J = 3.89$ Hz, 2H), 7.89 (2H), 7.33 (d, $J = 3.5$ Hz, 2H), 7.30 (d, $J = 3.72$, 4H), 7.09 (t, $J = 4.34$, 2H). T_d : 367.38 °C. HRMS (FAB) m/z : calc. for $\text{C}_{22}\text{H}_{12}\text{N}_2\text{S}_5$ $[\text{M}]^+$: 463.9604 found: 463.9603. Elemental Analysis calc.: C, 56.87; H, 2.60; N, 6.03; S, 34.50; found: C, 56.77; H, 2.53; N, 6.05; S, 34.66.

Device fabrication

We fabricated two types, planar heterojunction (PHJ) and bulk heterojunction (BHJ) devices with configurations of ITO (150 nm) / MoO_3 (5 nm) / Donor (10 nm) / C_{70} (40 nm) / BCP (8 nm) / Al (100 nm) and ITO (150 nm) / MoO_3 (5 nm) / Donor: C_{70} (1:1, 1:4; 50 nm) / C_{70} (40 nm) / BCP (8 nm) / Al (100 nm), respectively. On these devices, MoO_3 was used as a hole injection layer, fullerene derivatives as an acceptor, BCP (2,9-dimethyl-4,7-diphenyl-1,10-phenanthroline) as an exciton blocking layer, respectively. All layers were made using vacuum deposition.

Computational prediction of HOMO/LUMO energy level

To investigate the correlation between the molecular structure and the photophysical properties, we performed molecular orbital calculations using density functional theory (DFT). The ground state geometries and molecular orbital distribution of these molecules were optimized in vacuum using the DFT/B3LYP method with a 6-311G(d,p) basis set in the Gaussian09 package.

Figure 2.2.1 shows electron density distribution of HOMOs and LUMOs of three donor molecules. All of them have broad electron distribution at HOMO levels, and localized electron distribution in the core region of benzothiadiazole at LUMO levels. Calculations predicted that these donor molecules will show absorption bands resulting from ICT. HOMO and LUMO energy levels of donor molecules are stated on Table 1 and LUMO energy levels are high enough to transfer electron to acceptor molecule, C₇₀.¹⁰

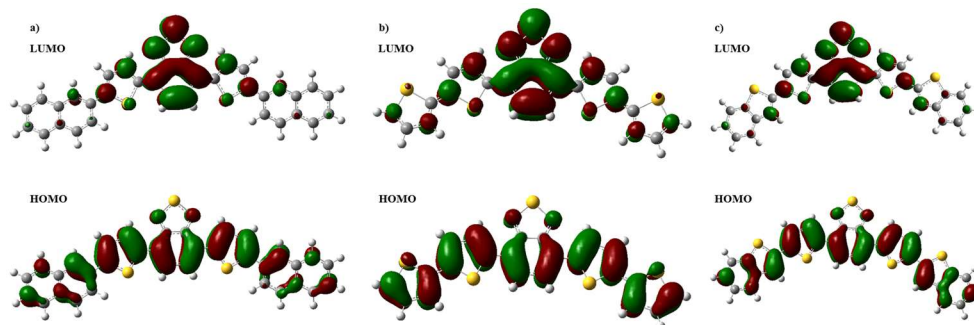


Figure 2.2.1 Molecular orbital surfaces of the HOMO and LUMO of a) NP, b) DT and c) BT, obtained by the DFT/B3LYP method with 6-311G(d,p) basis set

2.2.3 Results and discussion

Photophysical properties

New D-A-D type electron donor material **BT**, **NP** and **DT** were synthesized by the palladium catalysed Suzuki coupling reaction between compound 1 (for **NP** and **BT**) or 4,7-dibromo-2,1,3-benzothiadiazole (for **DT**) and aryl boronate according to **Scheme 2.2.1**. **Figure 2.2.2** shows the ultraviolet-visible absorption (UV-vis) and photoluminescence (PL) spectra of donor materials in solution and solid film. Three donor materials show first absorption maximum band at 356 nm (**DT**, **NP**) and 362 nm (**BT**)

due to $\pi - \pi^*$ transition of terminal groups and the second absorption maximum band at 502 nm (**DT**, **BT**) and 499 nm (**NP**) due to ICT. In solid state, there are no significant changes in first and second absorption bands, but band broadening is observed. It can be measured by the full width half maximum (FWHM). **NP** shows maximum at 518 nm with a FWHM of 142 nm (104 nm in solution), **DT** shows maximum at 527 nm with a FWHM of 148 nm (101 nm in solution) and **BT** shows maximum at 475 nm with a FWHM of 170 nm (106 nm in solution). In short, there is no significant difference in absorption ranges in solution or solid state between three molecules.

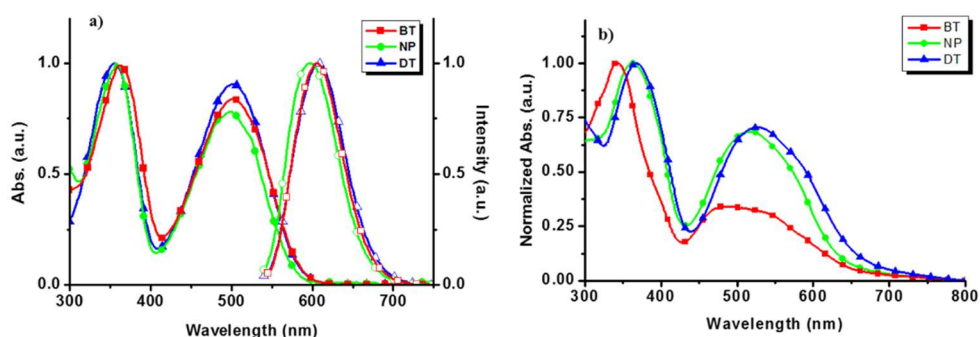


Figure 2.2.2 Absorption spectra and PL spectra of donor materials in a) CH_2Cl_2 and b) thin film. Filled shape indicates absorption spectra and empty shape indicates photoluminescence spectra. (square: BT, circle: NP, triangle:

DT)

Donors	λ_{abs} (nm) ^a	λ_{abs} (nm) ^b	FWHM (nm) ^a	FWHM (nm) ^b	ΔE_{opt} (eV) ^a	HOMO ^c (eV)	LUMO ^c (eV)	ΔE^c (eV)	HOMO ^d (eV)	LUMO ^d (eV)	ΔE^d (eV)
BT	362, 502	342, 475	106	170	2.2	-5.19	-3.17	2.20	-	-	-
DT	356, 502	367, 527	101	148	2.2	-5.13	-3.10	2.03	-5.28	-3.43	1.85
NP	356, 499	363, 518	104	142	2.23	-5.12	-3.01	2.11	-5.40	-3.50	1.90

Table 2.2.1 Optical, electrochemical and calculation data of BT, DT and NP. ^a In Solution; ^b in thin film; ^c calculated data; ^d experimental result of cyclic voltammetry.

Photovoltaic cell properties

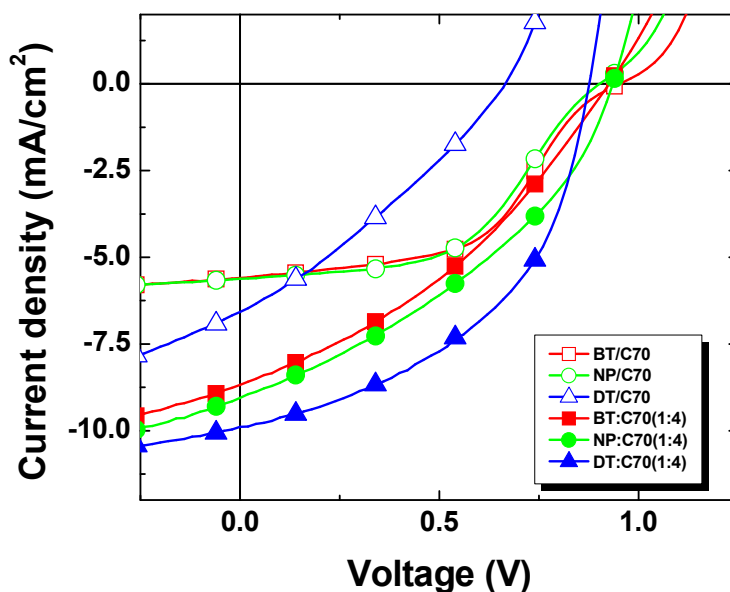


Figure 2.2.3 J-V characteristic plots for OPV devices. Empty shape indicates PHJ devices [ITO (150 nm) / MoO₃ (5 nm) / Donor (10 nm) / C₇₀ (35 nm) / BCP (8 nm) / Al (100 nm)]. Filled shape indicates BHJ devices [ITO (150 nm) / MoO₃ (5 nm) / Donor:C₇₀ (1:4; 50 nm) / BCP (8 nm) / Al (100 nm)]. (square: BT, circle: NP, triangle: DT)

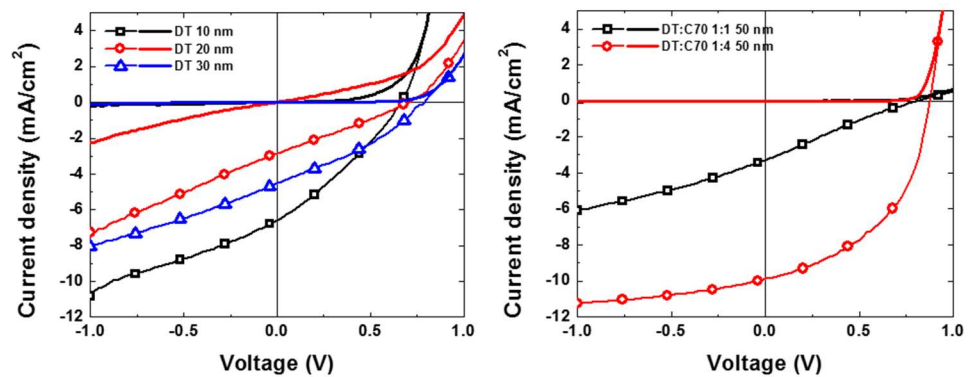


Figure 2.2.4 J-V characteristic plots for DT based devices (left: PHJ devices, right: BHJ devices).

	<i>PCE</i> / %	J_{SC} / mA/cm ²	V_{OC} / V	<i>FF</i>	$R_p A$ / Ωcm^2	$R_s A$ / Ωcm^2
DT 10 nm	1.32	6.58	0.67	0.30	6021.19	3.00
DT 20 nm	0.54	2.85	0.71	0.27	488.21	3.77
DT 30 nm	1.17	4.53	0.79	0.33	2.96×10^4	14.16
DT:C ₇₀ 1:1 50 nm	0.60	3.29	0.81	0.23	4.49×10^4	143.30
DT:C ₇₀ 1:4 50 nm	4.13	9.89	0.86	0.48	4.44×10^7	5.29

Table 2.2.2 OPV device performances for DT based devices

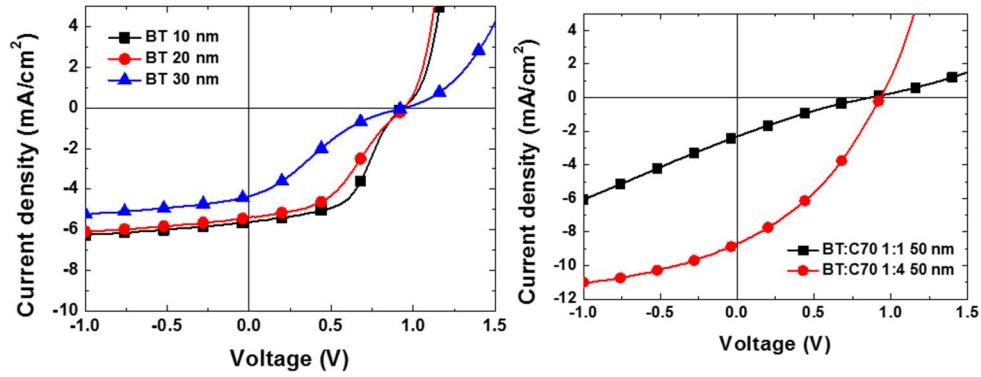


Figure 2.2.5 J-V characteristic plots for BT based devices (left: PHJ devices, right: BHJ devices).

	<i>PCE</i> /%	J_{SC} / mA/cm ²	V_{OC} / V	<i>FF</i>	$R_p A$ / Ωcm^2	$R_s A$ / Ωcm^2
BT 10 nm	2.69	5.61	0.94	0.51	3.09×10^7	2.30
BT 20 nm	2.15	5.40	0.96	0.41	6.45×10^7	5.51
BT 30 nm	0.66	3.57	0.95	0.19	12.14×10^7	315.62
BT:C ₇₀ 1:1 50 nm	0.35	2.03	0.86	0.20	4.14×10^7	367.49
BT:C ₇₀ 1:4 50 nm	2.81	8.60	0.94	0.35	12.53×10^7	13.36

Table 2.2.3 OPV device performances for BT based devices

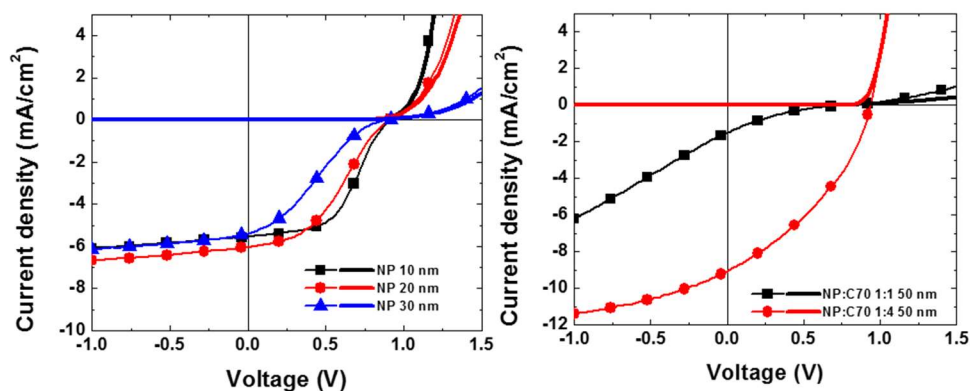


Figure 2.2.6 J-V characteristic plots for NP based devices (left: PHJ devices, right: BHJ devices).

	<i>PCE</i> /%	J_{SC} / mA/cm ²	V_{oc} / V	<i>FF</i>	R_pA / Ωcm^2	R_sA / Ωcm^2
NP 10 nm	2.56	5.62	0.92	0.50	7.39×10^7	3.56
NP 20 nm	2.16	6.04	0.91	0.39	8.71×10^7	20.62
NP 30 nm	1.36	5.46	0.88	0.28	4.57×10^7	218.41
NP:C ₇₀ 1:1 50 nm	0.13	1.10	0.77	0.16	4.57×10^7	1301.53
NP:C ₇₀ 1:4 50 nm	3.11	8.99	0.93	0.37	3.24×10^7	7.92

Table 2.2.4 OPV device performances for NP based devices

We fabricated PHJ and BHJ devices, as described in the experimental section. In the case of PHJ devices, donor layer thickness varies from 10 nm up to 40 nm. **Figure 2.2.3** shows the best current density vs. voltage (J-V) characteristics of PHJ devices fabricated using each donor material. **NP** and **BT** based

PHJ devices show higher performance at 10 nm rather than at thicker donor layer (**Figure 2.2.4-2.2.6** and **Table 2.2.2-2.2.4**). This is because **NP** and **BT** have too low HOMO energy level relative to transparent conducting oxide (TCO). This is also reflected in S-shaped curves at the intercept on the voltage axis as shown in **Figure 2.2.5-2.2.6**). Electrochemical experiment data also support that **NP** has deep HOMO relative to TCO (valence energy level -4.8 eV) (**Table 2.2.1**).¹¹ AFM images of **DT**, **NP** and **BT** films clearly indicate a greater tendency of **DT** to form large aggregates compared to **NP** and **BT**, which presumably results in less efficient exciton dissociation at the interface and thus lower fill factor and thus lower PCE in spite of higher current density (**Figure 2.2.9**).

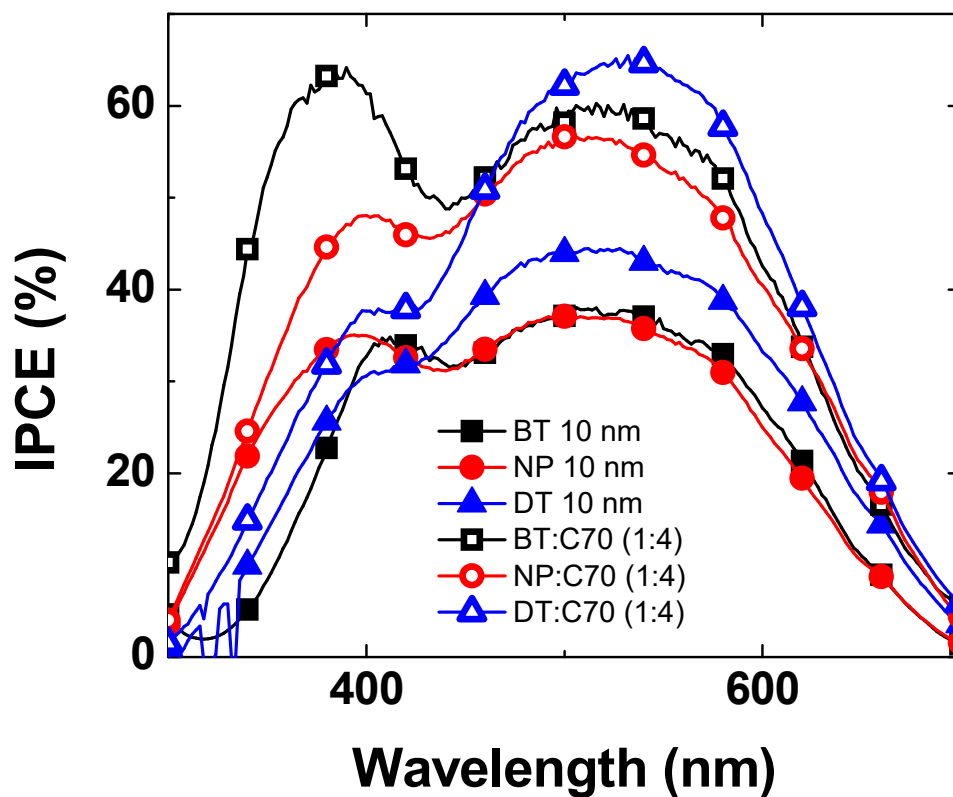


Figure 2.2.7 IPCE data for PHJ devices (active layer thickness: 10 nm) and BHJ devices (donor:C₇₀=1:4)

In general, PHJ devices show lower J_{sc} values compared to BHJ devices, because PHJ type devices have a narrower exciton dissociation area than BHJ ones.¹² Therefore, we fabricated co-deposited devices with C₇₀ to increase J_{sc} by increasing interfacial area between electron donor and electron acceptor. As expected,

co-deposited devices show higher J_{sc} values for all devices at blend ratio 1:4 = **BT** or **NP** or **DT**: C_{70} , compared to those of PHJ devices. This tendency is also observed in incident photon-to-current efficiency (IPCE) plots (**Figure 2.2.7**). Comparing **NP** and **BT** based BHJ devices with PHJ devices, the amount of increased PCE in the case of BHJ devices is always less than that of increased current density, because BHJ devices exhibit lower fill factor values. The low fill factor values result from increased series resistance of BHJ devices compared to PHJ devices (**Table 2.2.3-2.2.4**). For example, the series resistance of BT based BHJ device (**BT**: C_{70} = 1:4, 50 nm, $13.36 \Omega/cm^2$) is larger than that of **BT** based PHJ device (**BT** 10 nm/ C_{70} 35 nm, $2.30 \Omega/cm^2$) (**Table 2.2.3**). This tendency is also observed in the case of **NP** based devices (**Table 2.2.4**). The larger series resistance in case of **BT** and **NP** based BHJ devices is due to mixed layer itself. Co-deposited layers generate many interfaces in comparison with PHJ layers, which increases not only photo-current density,¹² but also electrical resistance owing to discrete domains, increased contact

resistance and longer electrical pathways.¹³ The fact that **DT** based BHJ devices display better PCE values than **NP** based BHJ devices can be rationalized by atomic force microscopy (AFM) images of **DT**:C₇₀ and **NP**:C₇₀ blended films as shown in **Figure 2.2.8**. The AFM images show clearly different domain sizes. **DT** + C₇₀ blended film with a larger domain compared to **NP** + C₇₀ blended film generates smaller interfacial area, which results in lower electrical resistance. The origin of different domain size was also investigated by X-ray diffraction (XRD) spectroscopy. The XRD spectrum of **DT** + C₇₀ blended film shows a well-preserved C₇₀ aggregation peak ($2\theta = 21^\circ$)¹⁴⁻¹⁵ compared to **NP** + C₇₀ blended film (**Figure 2.2.10**). This implies that C₇₀ preserves good crystalline morphology in **DT** + C₇₀ blended film.¹⁶

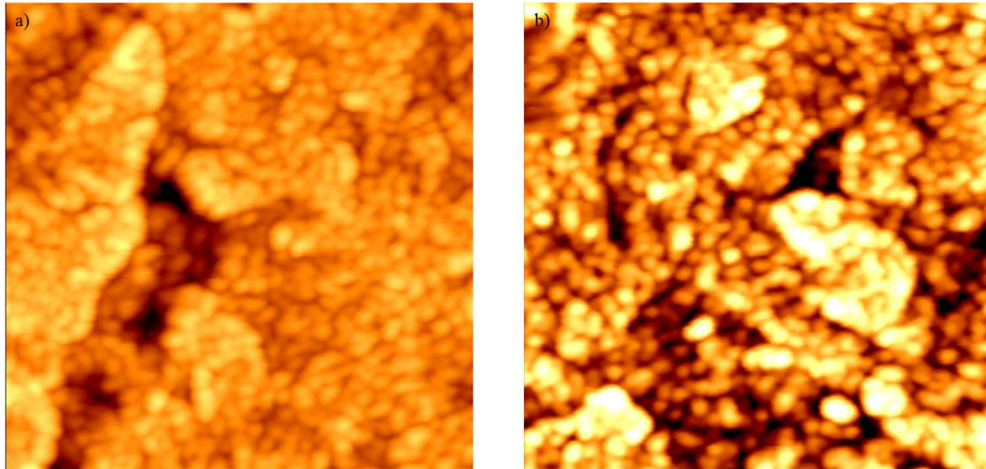


Figure 2.2.8 AFM images of a) DT:C₇₀, b) NP:C₇₀ deposited thin films. The film thickness is 50 nm, mixing ratio is 1:4 = donor:C₇₀, and scope range is 1000 nm×1000 nm.

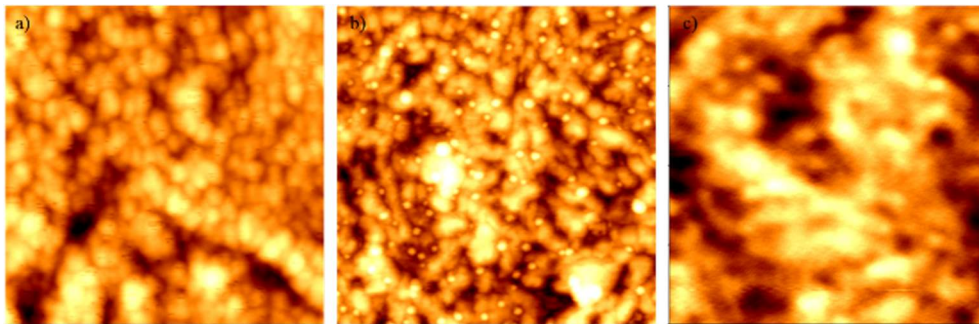


Figure 2.2.9 AFM images of a) NP, b) BT and c) DT films. The film thickness is 10 nm and scope range is 1000 nm×1000 nm

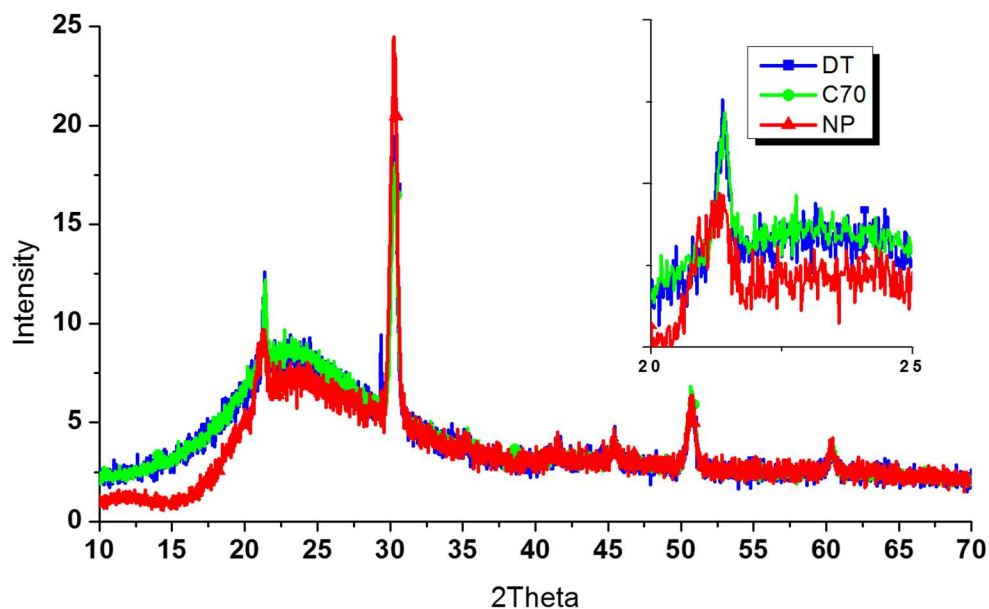


Figure 2.2.10 X-ray diffraction spectra for C₇₀, NP:C₇₀=1:4, DT:C₇₀=1:4 blended thin film on the ITO. (Inset: enlarged spectra range from 2 θ =20 to 25). Measuring condition: detector, LYNXEYE XE (0D mode); generator: 40 kV, 40 mA; 2 θ range : 10-70°; step: 0.02; scan speed: 0.5 sec/step; wavelength (λ): Cu K α 1 - 1.5418 Å

2.2.4 Conclusion

Three D-A-D type electron donor materials (NP, DT, BT), containing 2,1,3-benzothiadiazole as an electron withdrawing core, and benzothiophene, naphthalene and thiophene as electron donating terminal groups, were designed and synthesised for

vacuum-depositable small molecule organic solar cells. The maximum V_{oc} , J_{sc} and PCE values of the BHJ device based on DT:C₇₀=1:4 were 0.86 V, 9.89 mA · cm⁻², and 4.13%, respectively, under simulated AM 1.5 solar irradiation at 100 mW · cm⁻².

2.2.5 References and notes

1. (a) H. Hoppe and N. Sariciftci, *J. Mater. Res.*, 2004, **19**, 1924-1945; (b) G. Yu, J. Gao, J.C. Hummelen, F. Wudl, and A.J. Heeger, *Science*, 1995, **270**, 1789-1791; (c) N.S. Sariciftci, L. Smilowitz, A.J. Heeger, and F. Wudl, *Science*, 1992, 258, 1474-1476
2. A. Zitzler-Kunkel, M. Lenze, N. Kronenberg, A.-M. Krause, M. Stolte, K. Meerholz, and F. Würthner, *Chem. Mater.*, 2014, **26**, 4856-4866.
3. Y. Chen, Z. Du, W. Chen, S. Wen, L. Sun, Q. Liu, M. Sun, and R. Yang, *New Journal of Chemistry*, 2014, **38**, 1559-1564
4. R. Fitzner, E. Reinold, A. Mishra, E. Mena-Osteritz, H. Ziehlke, C. Körner, K. Leo, M. Riede, M. Weil, O. Tsaryova, A. Weiß, C. Uhrich, M. Pfeiffer, and P. Bäuerle, *Adv. Funct. Mater.*, 2011,

- 21**, 897–910.
5. R. Fitzner, E. Mena-Osteritz, K. Walzer, M. Pfeiffer, and P. Bäuerle, *Adv. Funct. Mater.*, 2015, **25**, 1845-1856
 6. H.-Y. Kong, D.-S. Chung, I.-N. Kang, E.-H. Lim, Y.-K. Jung, J.-H. Park, C.-E. Park, and H.-K. Shim, *Bulletin of the Korean Chemical Society*, 2007, **28**, 1945–1950.
 7. S. Roquet, A. Cravino, P. Leriche, O. Alévêque, P. Frère, and J. Roncali, *J. Am. Chem. Soc.*, 2006, **128**, 3459-3466
 8. Yamashita, Suzuki, and Tomura, *Synthetic Metals*, 2003, **133-134**, 341–343.
 9. X. Zhao, C. Piliago, B. Kim, D. Poulsen, B. Ma, D. Unruh, and J. Fréchet, *Chem. Mater.*, 2010, **22**, 2325-2332
 10. W. Zhou, S. Xie, S. Qian, T. Zhou, R. Zhao, G. Wang, L. Qian, and W. Li, *Journal of applied physics*, 1996, **80**, 459–463.
 11. V. Singh, CK Suman, and S. Kumar, Proc. of ASID '06, 8-12 Oct, *New Delhi*, 2006, **6**, 388
 12. P. Peumans, S. Uchida, and S. Forrest, *Nature*, 2003, 425, 158–162.

- 13.V. Coropceanu, J. Cornil, D. da Filho, Y. Olivier, R. Silbey, and J.-L. Brédas, *Chem. Rev.*, 2007, **107**, 926-952
- 14.M. Premila, C.S. Sundar, P.Ch. Sahu, A. Bharathi, Y. Hariharan, D.V.S. Muthu, A.K. Sood, *Solid State Commun.*, 1997, **104**, 237-242
- 15.Jun Sakai, Tetsuya Taima, Toshihiro Yamanari, Kazuhiro Saito, *Sol. Energ. Mat. Sol. C.*, 2009, **93**, 1149-1153
- 16.Li H., Earmme T., Subramaniyan S., Jenekhe S. A., *Adv. Energy Mater.*, 2015, **5**, 1402041

2.3 Electric field assisted molecular ordering for solution-processable organic solar cells

2.3.1 Introduction

Electricity becomes a more and more popular energy type of consumption. However, electricity is not the primary energy type gathered from nature, like oil and coal. Most of the electricity currently used globally is produced from other types of energy using primary energy resources. In this process, too many losses of energy have occurred. In detail, with combustion turbines, only about 40% of energy, and with nuclear fission reactors, about 60% of energy can be converted to electricity.

Furthermore, one of the advantages of electricity is the ease of energy storage. However, electricity also has a disadvantage in storing called electric discharge. Different from other energy types, stored electric energy makes discharge and disappeared naturally. Therefore, producing electric power directly without the consumption of primary energy resources is important for

sustainable development. Solar cells are one of the promising candidates for alternative electric power generator which use renewable energy resources. Solar cells do not require any raw material to produce electric power. The only requirement of solar cells for producing electric power is the incident light. Furthermore, light is an abundant energy resource, especially solar energy supplied from the sun. Its yearly supplied amount is 6000 times the global energy consumption in 2006.

Organic solar cells have a lower cost than inorganic solar cells, and energy level tuning for modulating absorption bandwidth is easier than inorganic solar cells. Despite the organic solar cell's low photoconversion efficiency, many researchers are paying attention to the organic photovoltaic cells for this reason. There are several well-known methods to achieve higher photoconversion efficiency on organic solar cells with organic small molecules. The first method is enhancing the absorption range of the electron donor material. It is the simplest and effective method. However, many numbers of organic electron donor material were reported with it. The second method is enhancing the exciton separation and

charge carrier transportation. Most of the recently reported achievements were included here. A well-ordered thin film structure is required to achieve a good charge carrier transporting ability and a good exciton separation ability.¹

In this paper, we designed and synthesized D-A type organic electron donor material and applied an electric field to express the ordered structure.

2.3.2 Experimental methods

Instruments

¹H spectra were recorded in CDCl₃ or DMSO using an Advance 300 MHz Bruker spectrometer. Mass spectra were obtained using a MALDI-TOF mass spectrometer from Bruker. Elemental analysis was performed with a Carlo-Erba model EA 1112 elemental analyzer. TGA was performed with a TA instrument model Q-5000 IR. UV-Vis spectra were recorded on a Beckman DU 650 spectrophotometer. Fluorescence spectra were recorded on a Jasco FP-7500 spectrophotometer. For solid-state measurements, the materials were thermally vapor deposited onto

quartz plates in a vacuum chamber to form 40 nm thick films. The cyclic voltammetry (CV) apparatus used was a CH Instruments model 650B electrochemical workstation. Cyclic voltammograms were obtained at room temperature in a three-electrode cell with a working electrode (glassy carbon), a reference electrode (Ag/Ag^+ 0.01 M), and a counter electrode (Pt), in dichloromethane or dimethyl formamide containing tetrabutylammonium hexafluorophosphate (TBAPF_6 , 0.1 M) as a supporting electrolyte, at a scan rate of 100 mV/s. All potential were calibrated with the standard ferrocene/ferrocenium (Fc/Fc^+ : -4.8 eV) redox couple. Molecular structures at ground state and HOMO/LUMO energy levels were calculated using Gaussian 09 Rev. B01 with DFT/B3LYP method with a 6-31G basis set.

Reagents and materials

All chemicals, such as 4-bromo triphenylamine, 5'-Bromo-2,2'-bithiophene-5-carboxaldehyde, and potassium carbonate were purchased from either Sigma-Aldrich or Toyko Chemical Industry

(TCI) and were used as received.

Device fabrication

We fabricated bulk heterojunction (BHJ) devices with configurations of ITO (150 nm) / PEDOT:PSS (50 nm) / active layer / LiF (1 nm) / Al (100 nm). PEDOT:PSS layer and active layer (composite film of electron donor and electron acceptor material mixture) were spin-coated. LiF interface treatment and Al electrode were vacuum deposited.

Electric field assist morphology modification

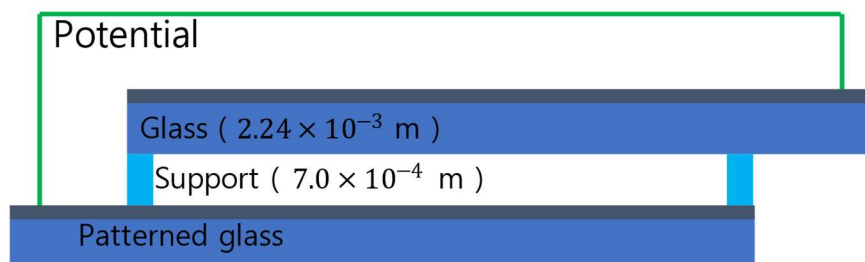


Figure 2.3.1 Schematic illustration of electric field generator; Patterned glass is OPV device.

ITO coated glass located on the OPV device which is made by procedure with glass support. An applied potential difference

between two ITO electrodes makes electric field (336 V m^{-1} @ 1 V).

An electric field is maintained during annealing process (130°C ,

15 min).

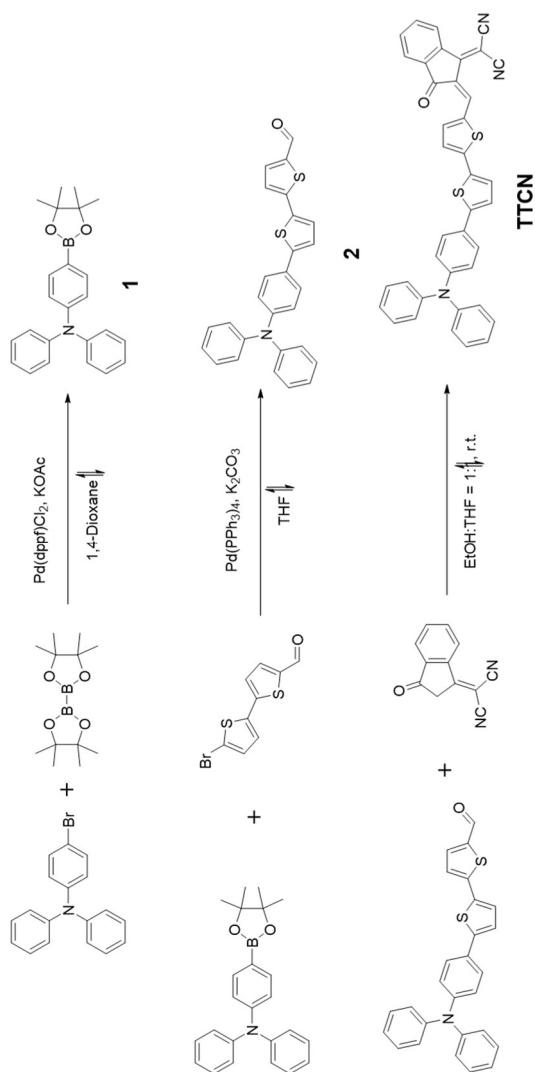
Synthesis

Compound 1 4-bromo triphenylamine (3.4 g, 10.5 mmol), Bis(pinacolato)diboron (2.23 g, 8.8 mmol), [1,1'-Bis(diphenylphosphino)ferrocene]palladium(II) dichloride (1.38 g, 1.7 mmol), and Potassium acetate (4.5 g, 45 mmol) were dissolved in 100 ml of 1,4-dioxane. The reaction mixture was refluxed overnight. After cooled to room temperature, the reaction mixture was separated with H_2O and MC. The separated solution was dried with magnesium sulfate anhydrous. The mixture was purified with column chromatography with hexane and EA. (1.9 g, 48.8%) $^1\text{H-NMR}$ (300 MHz, Acetone- D_6): 7.65 (d, $J = 8.4 \text{ Hz}$, 2H), 7.38 (d, $J = 5.1 \text{ Hz}$, 4H), 7.13 – 7.09 (m, 6H), 6.96 (d, 8.4 Hz , 2H), 1.35 (s, 12H)

Compound 2 Compound **1** (2 g, 5.4 mmol), 5'-Bromo-2,2'-bithiophene-5-carboxaldehyde (1.2 g, 4.5 mmol), and Tetrakis(triphenylphosphine)palladium(0) (260 mg, 0.2 mmol) were dissolved in 100 ml of THF. Sodium bicarbonate (1.6 g, 18 mmol) was dissolved in 20 ml of H₂O. sodium bicarbonate solution was added to reaction mixture and reaction mixture was refluxed overnight. After cooled to room temperature, reaction mixture was separated with H₂O and MC. Separated solution was dried with magnesium sulfate anhydrous. Mixture was purified with column chromatography with hexane and EA. (1.7 g, 88%)
¹H-NMR (300 MHz, Acetone-D₆): 9.94 (s, 1H) 7.94 (d, J = 4 Hz, 1H), 7.63 (d, J = 8.6 Hz, 2H), 7.54 (d, J = 3.9 Hz, 1H), 7.48 (d, J = 4 Hz, 1H), 7.43 (d, J = 3.9 Hz, 1H), 7.36 (dd, J = 7.3 Hz, J = 8.3 Hz, 4H), 7.14 (d, J = 7.6 Hz, 6H), 7.06 (d, J = 8.7 Hz, 2H)

TTCN Compound **2** (225 mg, 0.5 mmol) and 2-(3-oxo-indan-1-ylidene)-malononitrile (100 mg, 0.5 mmol) was dissolved in 50 ml of acetic anhydrous. The reaction mixture was refluxed overnight.

The reaction mixture was cooled to room temperature and quenched with H₂O, and filtered. The filtered reaction mixture was purified by excrudation with hexane MC. The product is dark blue solid. (200 mg, 63%) HRMS (FAB) m/z: calc. for C₃₀H₁₆N₂S₅ [M]⁺: 613.1283, found: 613.1281. T_d: 295°C, T_m: 254°C



Scheme 2.3.1 Synthetic scheme of TTCN

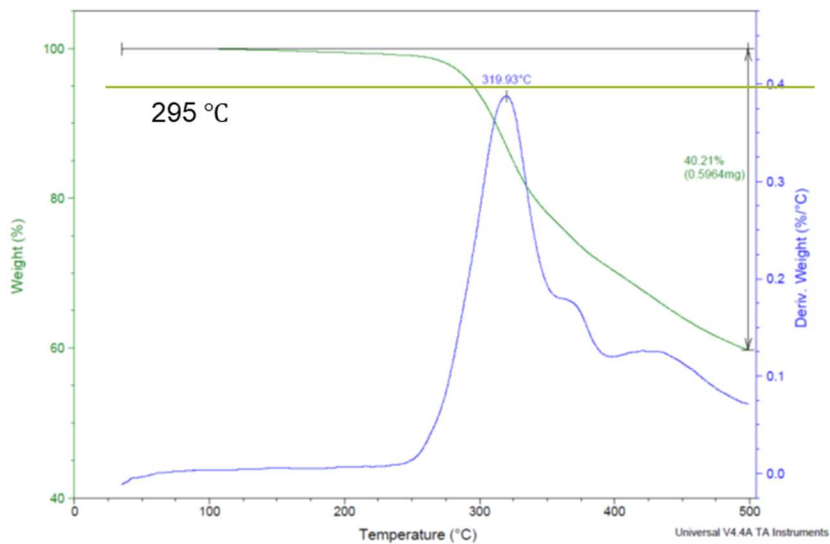


Figure 2.3.2 Result of thermogravimetric analysis for TTCN (N₂ gas, 10°C/min)

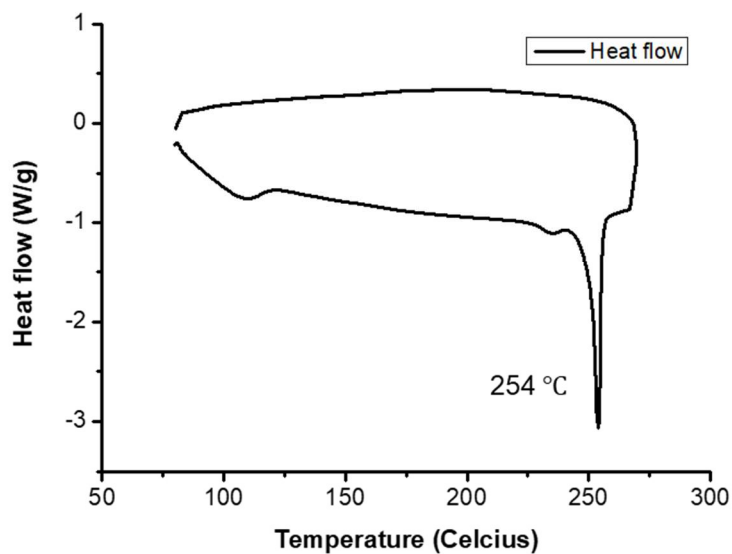


Figure 2.3.3 Result of differential scanning calorimetry for TTCN (N₂ gas, 10°C/min)

Computational prediction of HOMO/LUMO energy level

To investigate the correlation between the molecular structure and the photophysical properties, we performed molecular orbital calculations using density functional theory (DFT). The ground state geometries and molecular orbital distribution of these molecules were optimized in vacuum using the DFT/B3LYP method with a 6-311G(d,p) basis set in the Gaussian09 package.

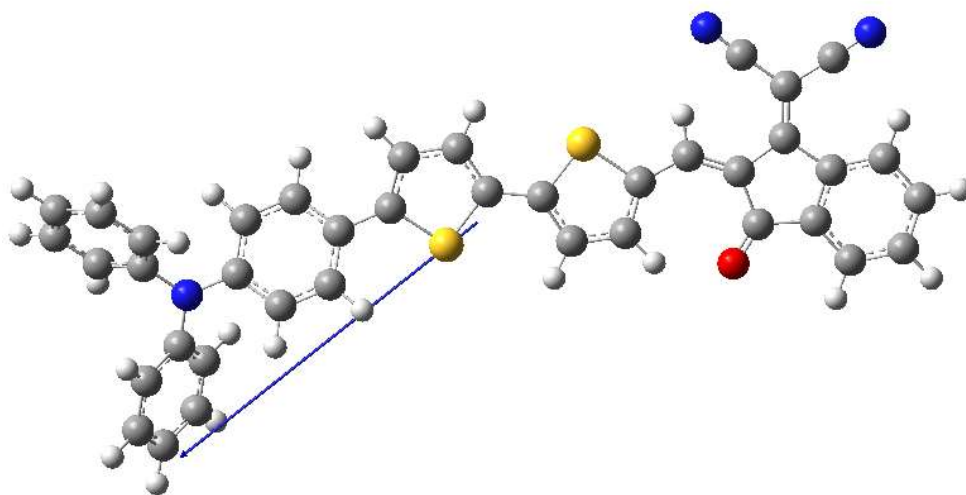


Figure 2.3.4 Calculated dipole moment of TTCN (9.87 debyes)

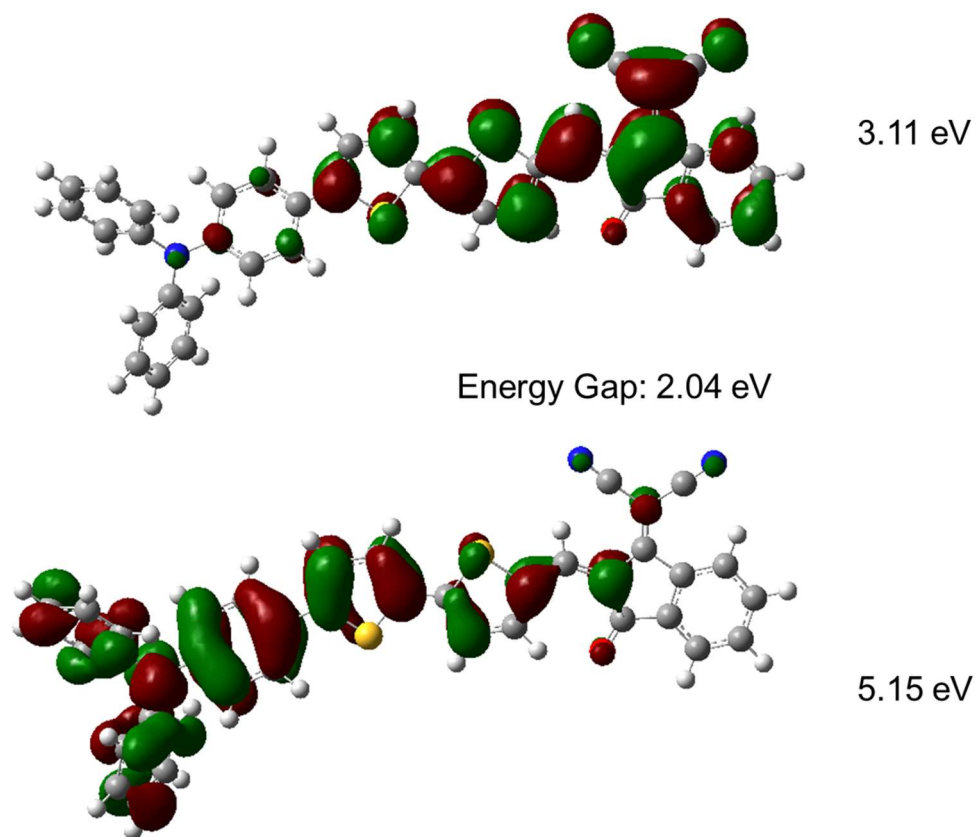


Figure 2.3.5 Theoretical molecular orbital distribution and energy level of TTCN's HOMO (downside) and LUMO (upside)

2.3.3 Results and discussion

Photophysical property

New D-A type electric field active electron donor material **TTNC** was synthesized following **Scheme 2.3.1**. Figure 2.3.6 shows the

ultraviolet-visible absorption spectrum of TTNC and photoluminescence spectrum of TTNC. TTNC shows a maximum absorption peak at 609 nm and 132 nm of fullwidth half maximum. There are 69% of photons in this range (from 500 nm to 750 nm) in the entire UV-Visible range (from 300 nm to 800 nm). Therefore, TTNC has a suitable absorption ability for the photovoltaic cell.

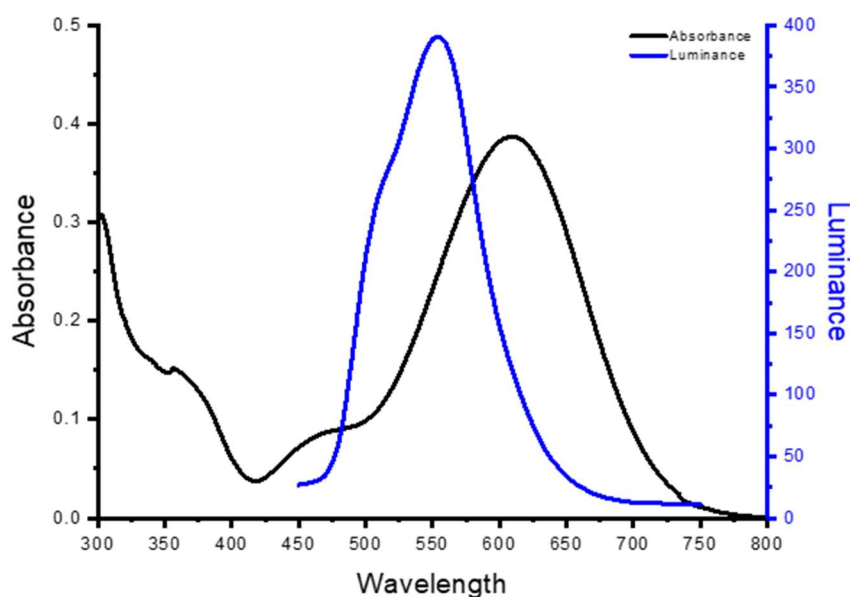


Figure 2.3.6 The absorption spectrum (black line) and the photoluminescence spectrum (blue line) of the TTNC. The TTNC is dissolved in MC.

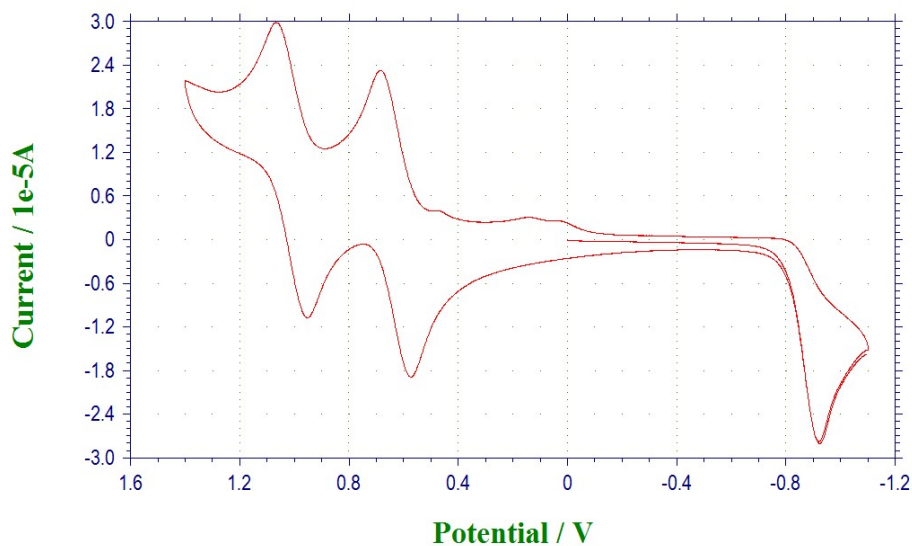


Figure 2.3.7 Cyclic voltammetry graph of TTNC in dichloromethane.

Figure 2.3.7 shows that TTNC has reversible oxidation and it implies that TTNC is stable for redox reaction at HOMO level. We found out the HOMO level (-5.36 eV) of TTNC and LUMO level (-3.66 eV) from result of cyclic voltammetry and absorption spectra. LUMO level of PC₇₀BM is known as -3.9 eV.² It means that TTNC has higher LUMO level than PC₇₀BM and there is no special problem to disturb electron flow from TTNC (electron donor material) to PC₇₀BM (electron acceptor material).

Photovoltaic property

We fabricated photovoltaic cells with a bulk heterojunction structure via a solution process. Table 2.3.1 shows several conditions of device fabrication.

Spin speed	Concentration (weight)	Blend ratio (weight)	J_{sc}	V_{oc}	FF	PCE
2000	20 mg/ml	1:4	4.3	0.60	0.33	0.85%
1000	20 mg/ml	1:4	2.4	0.48	0.28	0.33%
2000	20 mg/ml	1:1	3.7	0.46	0.33	0.55%
1500	20 mg/ml	1:1	3.1	0.54	0.30	0.49%
1000	20 mg/ml	1:1	3.3	0.56	0.29	0.54%

Table 2.3.1 Photovoltaic performance of TTNC devices before electric field assisted morphology modification

TTNC shows best performance, 0.85% of photon-current conversion efficiency at TTNC:PC₇₀BM = 1:4. Based on this result, we tried to apply electric field assist morphology modification. Figure 2.3.8 shows V-J curve of TTNC OPV devices with several electric field strength.

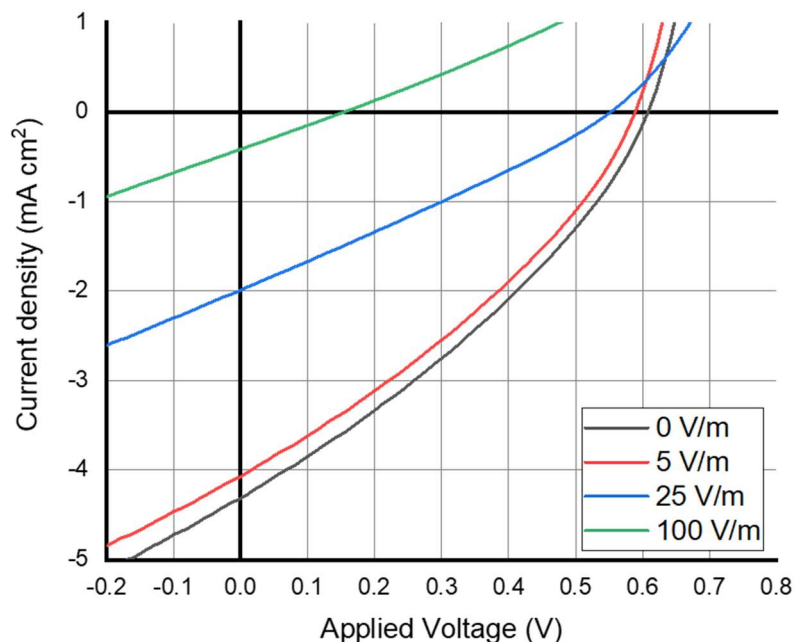


Figure 2.3.8 V-J curve with several different electric field strength

Electric field (V m^{-1})	V_{oc} (V)	J_{sc} (mA cm^{-2})	Fill factor	R_s (Ω)	R_p (Ω)	PCE (%)
0	0.6	-4.32	0.33	1415	4854	0.85
1.68×10^3	0.58	-4.07	0.33	983	3197	0.78
8.42×10^3	0.46	-2.01	0.29	1230	1995	0.26
3.37×10^4	0.15	-0.42	0.26	4174	30	0.02

Table 2.3.2 Photovoltaic properties of OPV device with electric field

Figure 2.3.8 and Table 2.3.2 show that open circuit voltage and current density of organic photovoltaic cells decreasing with electric field strength. Especially, parallel resistance (R_p) which

implies lack of exciton dissociation or bad electron transport, shows constantly going worse. Series resistance (R_s) only with $1.68 \times 10^3 \text{ V m}^{-1}$ of electric field shows improved electron transport.

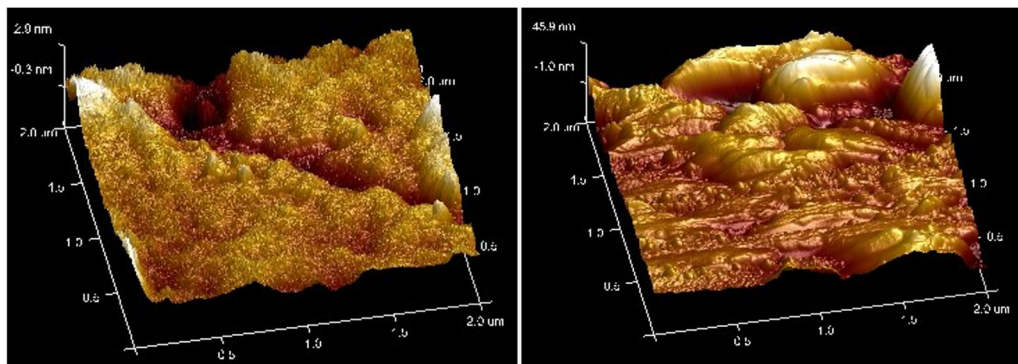


Figure 2.3.9 AFM height image of active layer of TTNC OPV a) without and b) with electric field during annealing procedure ($1.68 \times 10^3 \text{ V m}^{-1}$).

Figure 2.3.9 shows changes in morphology with or without electric field during the annealing procedure. The electric field makes the active layer rougher and it seems as a result of phase separation of general heavy molecules (PC_{70}BM) and electric field active molecules (TTNC).

2.3.4 Conclusion

We tried to control the morphology of the active layer for enhancing exciton dissociation and electron flow. Unfortunately, we could not achieve them because organic small molecules with a high dipole moment responses with an electric field too active. However, it is obvious that the electric field makes the morphology of the active layer. Therefore, organic small molecules with a small dipole moment will be candidates for controlling morphology through an electric field.

2.3.5 References and notes

1. C.-C. Lin, Y.-Y. Lin, S.-S. Li, C.-C. Yu, C.-L. Huang, S.-H. Lee, C.-H. Du, J.-J. Lee, H.-L. Chen and C.-W. Chen, *Energy & Environmental Science*, 2011, **4**, 2134-2139
2. Singh, S.P., Kumar, C.P., Sharma, G.D., Kurchania, R. and Roy, M.S., *Adv. Funct. Mater.*, 2012, **22**, 4087-4095
- 3.

Part 3. Organic thermoelectrics

3.1 Basic theories for the thermoelectric

The thermoelectric effect is a phenomenon in which the direct conversion of a temperature gradient to electric potential and vice versa. This phenomenon includes the Seebeck effect, the Peltier effect, and the Thomson effect. At first, the Seebeck effect, which makes the electric motive force from the temperature gradient via a thermocouple is reported by Thomas Johann Seebeck in 1822. The Peltier effect, which makes the temperature gradient from the electric motive force via a thermocouple, is reported by Jean Charles Athanase Peltier in 1836. Finally, William Thomson reported in 1857 that a single material with the temperature gradient shows extra thermal changes, not joule heating.¹³ These phenomena related to temperature difference and electromotive force have close intimacy and are called the thermoelectric

¹³ Thomson, W. 4. On a Mechanical Theory of Thermo-Electric Currents. Proc Royal Soc Edinb 3, 91–98 (1857).

effect.¹⁴

Researchers paid attention to the thermoelectric effect, especially the Seebeck effect, which makes electromotive force from the temperature gradient. Like a photovoltaic effect, the Seebeck effect can produce electrical power without the consumption of primary energy resources. Furthermore, the Seebeck effect makes it possible to recycle waste thermal energy. As written in the previous section about the photovoltaic effect, generating electrical power from the primary energy resource consumes nearly twice the amount which is generated. The rest of the energy that is not converted into electrical power is converted into heat energy and wasted. Under these circumstances, recycling wasted heat energy and converting it into electrical power may increase overall energy conversion efficiency. In addition, thermoelectric generators that produce electrical power through the thermoelectric effect require only a thermal energy gradient. It

¹⁴ DiSalvo, F. J. Thermoelectric Cooling and Power Generation. *Science* 285, 703–706 (1999)

means thermoelectric generators can be planted in a narrow space or closed space where light cannot be reached. Moreover, human consumption activities make thermal energy wanted or not, resulting in a thermal energy gradient.

Traditionally, researches on thermoelectric materials are focused on inorganic materials. These inorganic materials include bismuth telluride (Bi_2Te_3), silicon-germanium (SiGe), lead telluride (PbTe), and tin selenide (SnSe).¹⁵ Mostly due to bismuth telluride's high zT at 300 K, bismuth telluride becomes a common thermoelectric material for room temperature. (**Figure 3.1.1**)

However, inorganic materials have disadvantages on production cost and environmental disaffect. Organic thermoelectric materials, including polymers and small molecules, have emerged as new candidates. Thus they have a low figure of merit and power factors than inorganic thermoelectric materials.

¹⁵ Chen, X. et al. Thin Film Thermoelectric Materials: Classification, Characterization, and Potential for Wearable Applications. *Coatings* 8, 244 (2018).

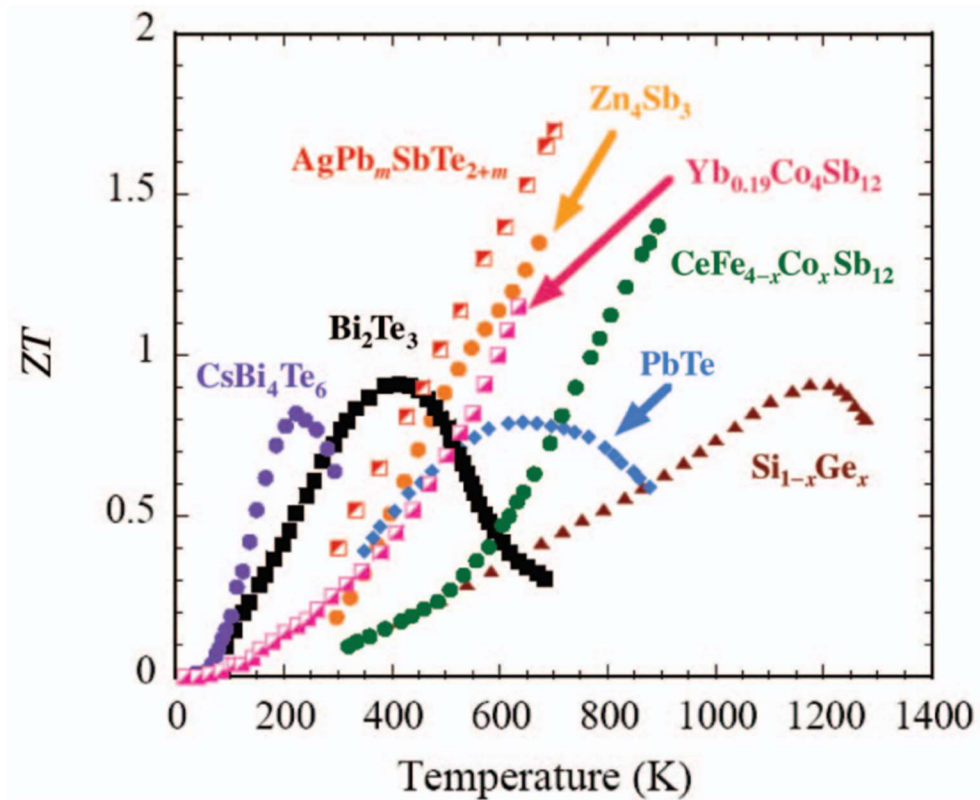


Figure 3.1.1 Figure of merit ZT shown as a function of temperature for several bulk thermoelectric materials ¹⁶ Bismuth telluride has the highest zT in the range from 300 K to 400 K

¹⁶ Tritt, T. M. & Subramanian, M. A. Thermoelectric Materials, Phenomena, and Applications: A Bird's Eye View. Mrs Bull 31, 188–198 (2006).

Type	TE material	α [$\mu\text{V/K}$]	σ [S/cm]	PF [$\mu\text{W/mK}^2$]	λ [W/mK]	ZT
P type	$\text{Sb}_{1.6}\text{In}_{0.15}\text{Te}_3$	124	500	-	0.9	0.27
	$\text{Mg}_{0.995}\text{Li}_{0.005}\text{Ag}_{0.97}\text{Sb}_{0.99}$	200	588	2300	0.9	0.75
	$\text{Mg}_{0.97}\text{Zn}_{0.03}\text{Ag}_{0.9}\text{Sb}_{0.95}$	85	952	690	1.25	0.28
	$\text{MgAg}_{0.97}\text{Sb}_{0.985}\text{Bi}_{0.005}$	255	285	1860	0.8	0.7
	$\text{Bi}_{0.38}\text{Sb}_{1.62}\text{Te}_3 + \text{Ge}_{0.3}\text{Mn}_{0.5}\text{Te}$	194	1100	43	1.28	1.22
	$\text{CuInTe}_2 + \text{Bi}_{0.4}\text{Sb}_{1.6}\text{Te}_3$	175	1250	40	1.1	1.15
	$\text{Bi}_{0.4}\text{Sb}_{1.59}\text{Ge}_{0.01}\text{Te}_3$	207	909	48	1.05	1.36
	$\text{Cu}_{0.002}\text{Bi}_{0.3}\text{Sb}_{1.495}\text{Te}_3$	150	1400	-	1	0.97
	$\text{Bi}_{0.5}\text{Sb}_{1.5}\text{Te}_{2.7}\text{Se}_{0.3}$	109	1250	-	0.96	0.48
	$\text{Bi}_{0.35}\text{Sb}_{1.65}\text{Te}_3$	270	285	-	0.9	0.8
	$\text{Bi}_{0.48}\text{Sb}_{1.52}\text{Te}_3 + 0.05 \text{ wt\% PbTe}$	177	1800	56	1.85	0.9
	$\text{Bi}_{0.4}\text{Sb}_{1.6}\text{Te}_3$ alloys + 5 wt% Te	155	880	21	1.4	0.48
	$(\text{BiSbTe}_{1.4}\text{Se}_{1.5}\text{Bi}_{0.2}\text{Ag}_{0.3})$	200	120	480	0.6	0.25
	$\text{Bi}_{0.48}\text{Sb}_{1.2}\text{Te}_3$	150	300	-	-	0.58
	$\text{Mg}_{0.995}\text{Yb}_{0.005}\text{Ag}_{0.97}\text{Sb}_{0.99}$	220	476	2180	0.81	0.8
	$\text{MgAg}_{0.97}\text{Sb}_{0.99}$	170	580	1620	0.8	0.55
	$\text{MgAg}_{0.97}\text{Sb}_1$	220	476	2280	0.88	0.78
	$\text{Mg}_{0.995}\text{Ca}_{0.005}\text{Ag}_{0.97}\text{Sb}_{0.99}$	225	416	2080	0.84	0.75
	$\text{Mg}_{0.97}\text{Zn}_{0.03}\text{Ag}_{0.9}\text{Sb}_{0.95}$	285	166	1250	0.62	1.1
	$\text{Bi}_{0.5}\text{Sb}_{1.5}\text{Te}_{3.2}$	224	800	-	0.65	1.2
$\text{Bi}_2\text{Te}_{2.99}\text{Se}_{0.6}$	-160	1200	31	1.3	0.7	
Bi_2Se_3	-105	526	575	1.2	0.14	
N type	$\text{Bi}_2\text{Te}_{2.7}\text{Se}_{0.3}$	-263	250	-	0.79	0.76
	$\text{Bi}_2\text{Te}_{2.7}\text{Se}_{0.3}$	-146	2250	49	2.09	0.81
	$\text{Bi}_2\text{Te}_{2.7}\text{Se}_{0.3} + 0.3 \text{ wt\% KI}$	-135	1350	26	1.45	0.51
	Bi_2Te_3	-105	1600	17.5	1.65	0.33
	$\text{Bi}_2\text{Te}_{2.7}\text{Se}_{0.3}$	-168	600	1650	0.73	0.68
	Bi_2Te_3	-105	1600	17.5	1.65	0.33

Figure 3.1.2 Recent trend in inorganic thermoelectric generators¹⁷

¹⁷ Soleimani, Z., Zoras, S., Ceranic, B., Shahzad, S. & Cui, Y. A review on recent developments of thermoelectric materials for room-temperature applications. *Sustain Energy Technologies Assessments* 37, 100604 (2020).

The earliest reference to the thermoelectric effect of the organic material can be found in a paper published in 1973. A. F. Garito and A. J. Heeger reported thermopower (the Seebeck coefficient) of organic material, tetrathiofulvalinium tetracyanoquinodimethane.¹⁸ In this report, tetrathiofulvalinium tetracyanoquinodimethane single crystal shows $-30 \mu\text{V/K}$ of the Seebeck coefficient at room temperature. However, the thermoelectric effect of organic material is used for analyzing a conducting mechanism or trait. It is not a report for the thermoelectric generator. However, it seems to be the first mention of the thermoelectric effect of the organic material. Similar to this report, DSeDTF-TCNQ and TSeF-TENQ were also reported. (**Figure 3.1.3**)

¹⁸ Chaikin, P. M., Kwak, J. F., Jones, T. E., Garito, A. F. & Heeger, A. J. Thermoelectric Power of Tetrathiofulvalinium Tetracyanoquinodimethane. *Phys Rev Lett* 31, 601–604 (1973)

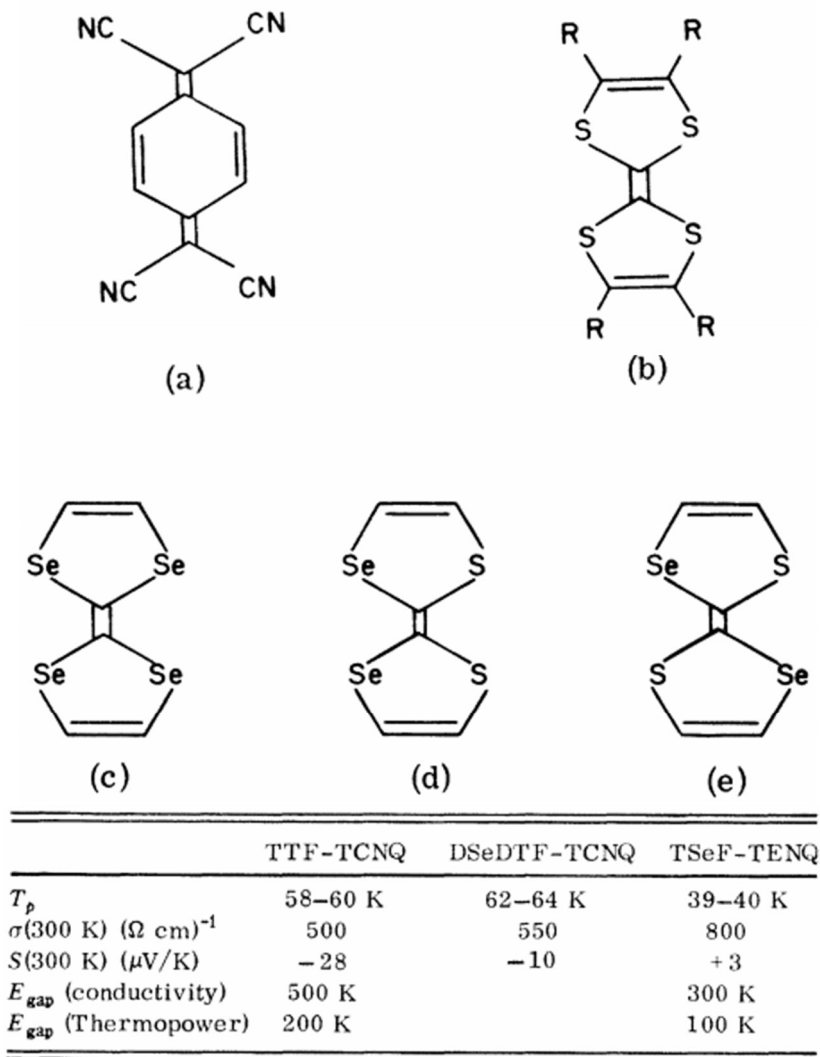


Figure 3.1.3 Chemical structure and thermoelectric performance. a) TCNQ, b) TTF, c) TSeF, d) cis-DSeDTF, and e) tran-DSeDTF¹⁹

¹⁹ Chaikin, P. M., Greene, R. L., Etemad, S. & Engler, E. Thermopower of an isostructural series of organic conductors. Phys Rev B 13, 1627–1632 (1975)

These reports showed that the potential for organic generators. However, organic materials generally have low electrical conductivity. It makes the organic thermoelectric generator has a high power factor hard. Furthermore, small molecules are lower than polymers. Therefore, the application of organic materials as a thermoelectric generator started with conductive polymers like PEDOT:PSS or polyacetylene.

3.1.1 Thermoelectric effect

The thermoelectric effect on thermoelectric generators means the Seebeck effect. Like as written in the previous section, the Seebeck effect is a phenomenon that produces electromotive force from a thermal gradient. Therefore, the evaluation of the thermoelectric performance on the thermoelectric generators is based on the Seebeck effect. The first index is the Seebeck coefficient ($\mu\text{V K}^{-1}$), which implies how much electromotive force is produced from each temperature difference. It can be measured directly from the thermoelectric device.

The second index is the power factor. The power factor is calculated from the Seebeck coefficient and the electrical conductivity of the thermoelectric device via the following equation.

$$P = \sigma S^2$$

P is the power factor in $\text{W m}^{-1} \text{K}^{-2}$. σ is the electrical conductivity in $\Omega^{-1} \text{m}^{-1}$. S is the Seebeck coefficient in V K^{-1} .

The power factor means the maximum electrical power which a

thermoelectric generator can produce with a temperature difference (K), regardless of how much thermal energy is transferred at the same time.

The third index is the figure of merit, zT .²⁰ zT is also a calculated value. The difference compared to the power factor is considering transferred thermal energy through the thermoelectric generator. The figure of merit for thermoelectric generator, zT , can be calculated via the following equation.

$$zT = \frac{\sigma S^2 T}{\kappa}$$

zT is a unitless figure of merit for the thermoelectric generator. T is the temperature in K. κ is the thermal conductivity of the thermoelectric generator.

zT shows the ratio of the produced power by thermoelectric generator and the transported thermal energy by the thermoelectric

20 Snyder, G. J. & Snyder, A. H. Figure of merit ZT of a thermoelectric device defined from materials properties. *Energy Environ Sci* 10, 2280–2283 (2017).

generator. Higher zT means that the thermoelectric generator can produce more electrical power at the same thermal energy gradient. However, the optimum efficiency (zT) condition and the optimum power output (power factor, σS^2) condition is not the same. (Figure 3.1.4) In organic semiconductors or organic hybrid system, measuring the thermal conductivity is challenging. Therefore, the power factor is more frequently used as a thermoelectric performance index.

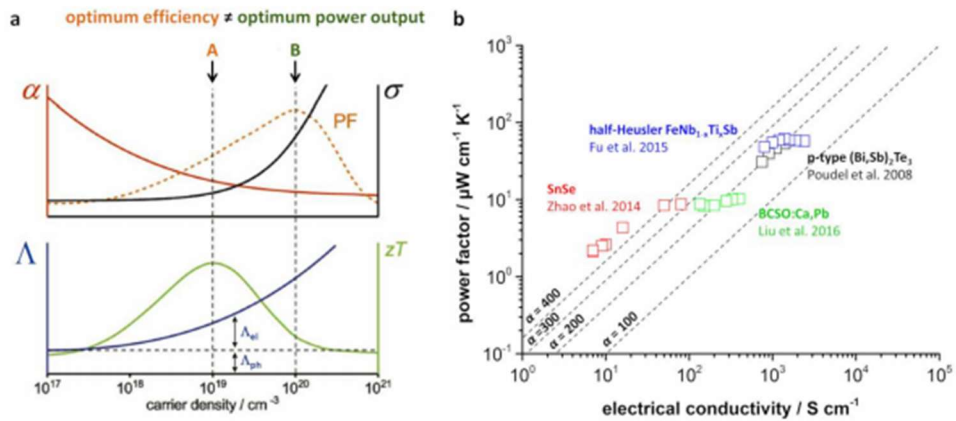


Figure 3.1.4 (a) Seebeck coefficient α , electrical conductivity σ , entropy conductivity Λ , and the resulting power factor $\sigma\alpha^2$ and zT value as a function of the charge carrier density; adapted from with permission from Elsevier; **(b)** Type-I Ioffe plot of various reported high- zT materials. Seebeck coefficient α is given in $\mu\text{V K}^{-1}$. Different data points for the same material

refer to different temperatures²¹

To achieve a high power factor or a high zT (figure of merit), we need to increase the Seebeck coefficient or electrical conductivity.

The Seebeck coefficient is determined by the energy gap between the Fermi level and conduction or valence band in the semiconductor. It can be expressed as the following equation.²²

$$S = -\frac{k}{e} \int \left(\frac{E - E_F}{kT} \right) \frac{\sigma(E)}{\sigma} dE$$

S is the Seebeck coefficient. k is the Boltzmann constant. e is the charge of an electron. T is the temperature. σ is the electrical conductivity. E is the energy level. E_F is the Fermi level.

In the semiconductor case, the electron flows only in one band (the conduction band or the valence band). Therefore, the heading

²¹ Wolf, M., Hinterding, R. & Feldhoff, A. High Power Factor vs. High zT —A Review of Thermoelectric Materials for High-Temperature Application. *Entropy* 21, 1058 (2019).

²² Fritzsche, H. A general expression for the thermoelectric power. *Solid State Communications* 9, 1813–1815 (1971).

equation can be expressed as the following equation for

$\int_{E_V}^{\infty} \sigma(E) dE = 0$ (case of the valence band conducting).

$$S = -\frac{k}{e} \int_{-\infty}^{E_V} \left(\frac{E - E_F}{kT} \right) \frac{\sigma(E)}{\sigma} dE$$

Let $\epsilon = E_V - E$, E_V is the energy level of the valence band edge.

$$S = -\frac{k}{e} \int_{-\infty}^{E_V} \left(\frac{E_V - E_F - \epsilon}{kT} \right) \frac{\sigma(\epsilon)}{\sigma} d\epsilon$$

$$S = -\frac{1}{eT} \int_{-\infty}^{E_V} (E_V - E_F - \epsilon) \frac{\sigma(\epsilon)}{\sigma} d\epsilon$$

$$S = \frac{1}{eT} \left[\int_{-\infty}^{E_V} (E_F - E_V) \frac{\sigma(\epsilon)}{\sigma} d\epsilon + \int_{-\infty}^{E_V} \epsilon \frac{\sigma(\epsilon)}{\sigma} d\epsilon \right]$$

$$S = \frac{1}{eT} \left[(E_F - E_V) \frac{1}{\sigma} \int_{-\infty}^{E_V} \sigma(\epsilon) d\epsilon + \int_{-\infty}^{E_V} \epsilon \frac{\sigma(\epsilon)}{\sigma} d\epsilon \right]$$

Because $\sigma = \int \sigma(E) dE$,

$$S = \frac{1}{eT} \left[(E_F - E_V) \frac{\int_{-\infty}^{E_V} \sigma(\epsilon) d\epsilon}{\int_{-\infty}^{E_V} \sigma(\epsilon) d\epsilon} + \int_{-\infty}^{E_V} \epsilon \frac{\sigma(\epsilon)}{\sigma} d\epsilon \right]$$

$$S = \frac{1}{eT} \left[(E_F - E_V) + \frac{1}{\sigma} \int_{-\infty}^0 \epsilon \sigma(E) d\epsilon \right]$$

The heading result shows that the Seebeck coefficient is determined by the energy difference between the Fermi level and the conducting energy level. (**Figure 3.1.5**) Similar to the case of the valence band conducting, the conduction band conducting is written by following. ($\epsilon = E - E_C$)

$$S = -\frac{1}{eT} \left[(E_C - E_F) + \frac{1}{\sigma} \int_0^{\infty} \epsilon \sigma(\epsilon) d\epsilon \right]$$

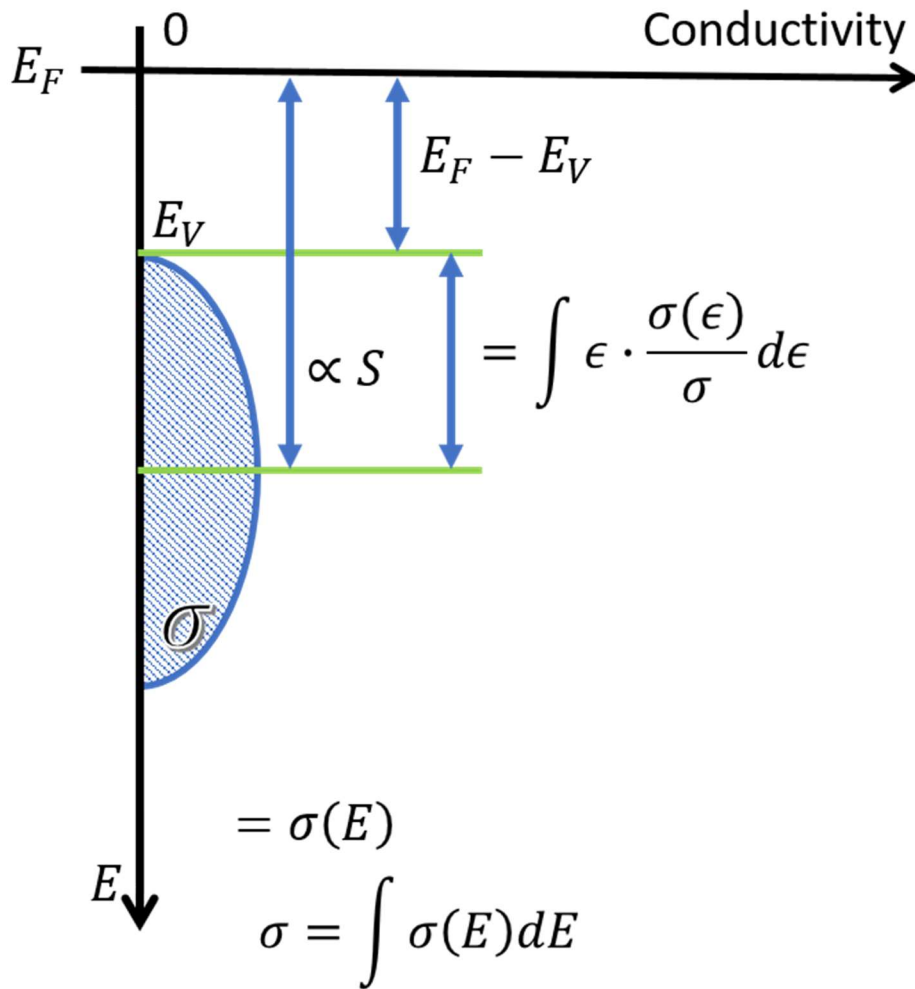


Figure 3.1.5 Schematic illustration of the relationship between the Seebeck coefficient and energy level.

From these relationships, we can suppose several methods for enhancing the Seebeck coefficient. First, increase the energy gap between the Fermi level and electron-conducting level. As shown in the heading equations, the Seebeck coefficient grows in

proportion to the energy gap between the Fermi level and electron-conducting level. Therefore, the low-lying valence band in the p-type semiconductor or the high-lying conduction band in the n-type semiconductor give a large Seebeck coefficient. (**Figure 3.1.6**)

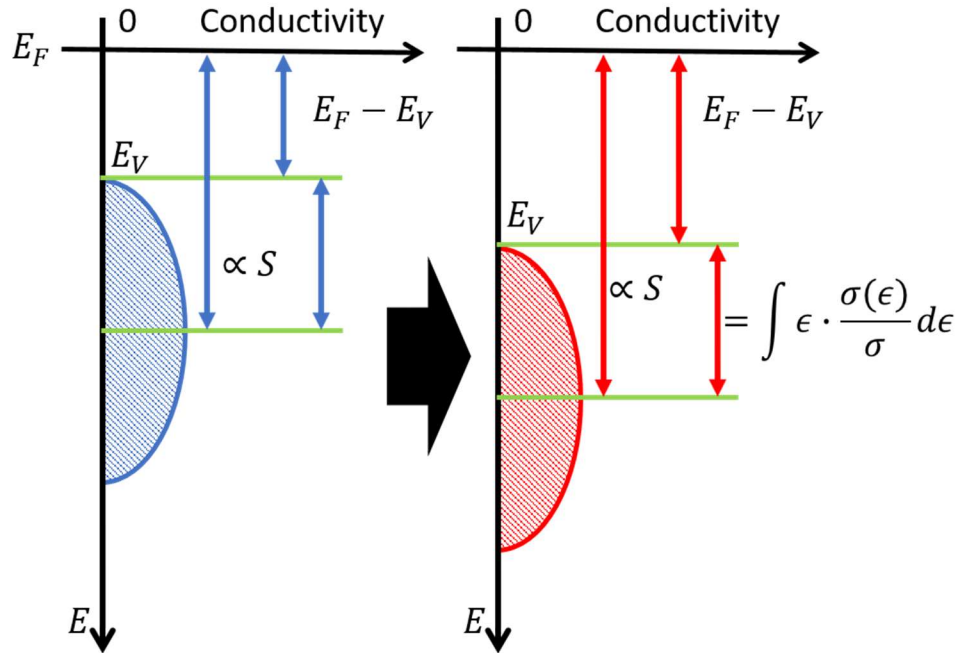


Figure 3.1.6 Energy diagram for the Seebeck coefficient's increment with increased energy gap between the Fermi level and the valence band level.

Second, modulate the proportion of electrical conductivity. As the equation related to the Seebeck coefficient, the proportion of electrical conductivity also affects the Seebeck coefficient. If the

thermoelectric generator has a high proportion at the close to the Fermi level, the Seebeck coefficient goes lower. Contrary, If the thermoelectric generator has a high proportion at the far from the Fermi level, the Seebeck coefficient goes higher. (**Figure 3.1.7**)

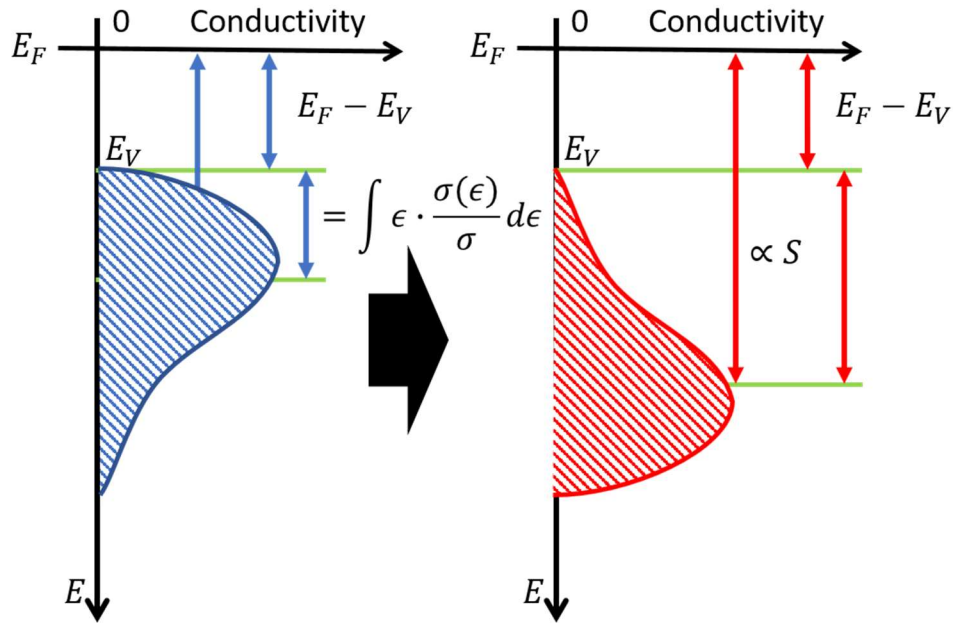


Figure 3.1.7 Energy diagram for the Seebeck coefficient's increment with the change of the electrical conductivity function.

3.1.2 Energy filtering effect

The energy filtering effect is suggested in the inorganic thermoelectric generator.²³ The energy filtering effect is the simple concept for increasing the Seebeck coefficient via modulating the charge carrier density.

In the previous section, the Seebeck coefficient is written in terms of electrical conductivity and the energy level. The energy filtering effect modulates both the energy level and electrical conductivity via the energy barrier, which interferes with electron flows. At first, two materials which have different conducting energy level is required for the occurrence of the energy filtering effect. One thermoelectric material that has a smaller energy gap from the Fermi level contributes dominantly to electron flows. The other

²³ A. Pakdel, Q. Guo, V. Nicolosi and T. Mori, *J Mater Chem A*, 2018, 6, 21341–21349; T. E. Humphrey, M. F. O’Dwyer, H. Linke, *J. Phys. D: Appl. Phys.* 2004, 38, 2051; Y. I. Ravich, in *CRC Handbook of Thermoelectrics* (Ed: D. M. Rowe), CRC Press, New York 1995, pp. 67–73

material that has a larger energy gap from the Fermi level contributes less. Electrons in a thermoelectric material mainly flow through a material that has a smaller energy gap. When these two materials consist of a composite layer, the energy barrier is created at the two materials' interface. This energy barrier interferes with the electron flow via blocking the transport of electrons, which have insufficient energy to overcome the energy barrier. Therefore, only electrons which have sufficient energy to overcome the energy barrier can be transferred. (Figure 3.1.8)

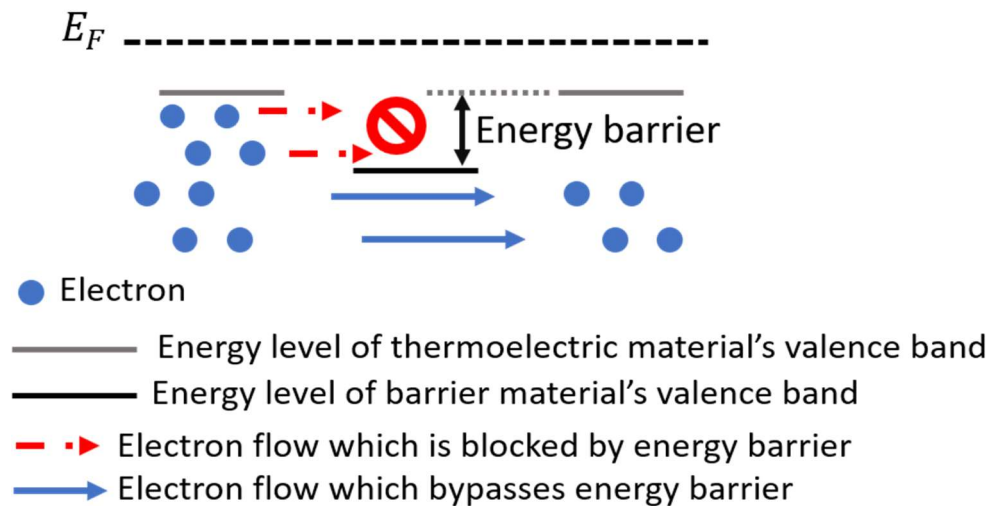


Figure 3.1.8 Schematic illustration of the mechanism of the energy filtering effect. This figure illustrates the case of p-type semiconductors. Therefore, electrons, which are located on a lower side, have larger energy.

Therefore, electrons, which have insufficient energy to overcome the energy barrier, are removed from the electron flow in the thermoelectric generator. It implies that the average energy of electrons, which participate in the electron flow, is increased. It results in an increment of the Seebeck coefficient.

Figure 3.1.9 shows changes in the electrical conductivity and the Seebeck coefficient that vary to the energy filtering ratio. An increment of the energy filtering ratio implies that the energy barrier makes more electrons blocked. It makes the average energy of electrons, which participate in the electron flow, larger and the number of electrons smaller. This electron flow restriction, which has small energy, produces a larger Seebeck coefficient and smaller electrical conductivity.

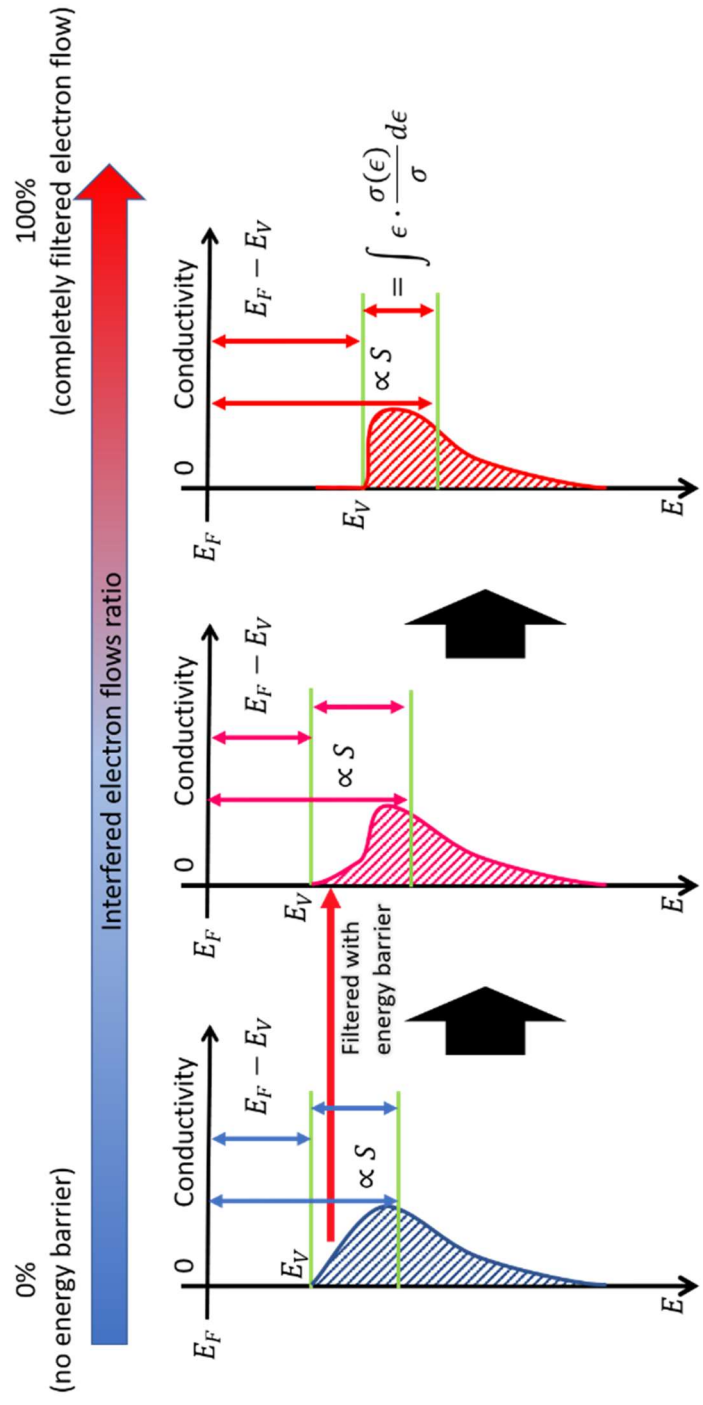


Figure 3.1.9 Energy diagram for the Seebeck coefficient's increment with the energy filtering effect

3.1.3 Organic thermoelectric generators

Researches on organic small molecule thermoelectric effect seem to have been reported in 2010 at first.²⁴ Kentaro Harada et al. fabricated an organic small molecule thermoelectric generator with pentacene and F₄-TCNQ. They fabricated F₄-TCNQ doped pentacene thermoelectric devices and planar heterojunction devices, which consist of F₄-TCNQ and pentacene. In F₄-TCNQ doped pentacene, the organic thermoelectric generator exhibits 400 $\mu\text{V}/\text{K}$ of maximum Seebeck coefficient at pure pentacene film and 2 $\mu\text{W}/\text{m}\cdot\text{K}^2$ of maximum power factor at a planar heterojunction structure of F₄-TCNQ and pentacene. (**Figure 3.1.10**) Kentaro Harada et al. show the potential of organic material-based thermoelectric generators. The pentacene thin film

²⁴ Harada, K., Sumino, M., Adachi, C. & Tanaka, S. Improved thermoelectric performance of organic thin-film elements utilizing a bilayer structure of pentacene and 2, 3, 5, 6-tetrafluoro-7, 7, 8, 8-tetracyanoquinodimethane (F₄-TCNQ) (2010).

shows a much higher Seebeck coefficient than general thermoelectric materials like Bi_2Te_3 . However, a single layer of crystalline pentacene has a very low electrical conductivity and it makes the power factor of pentacene thin-film very low. They modulate a concentration of $\text{F}_4\text{-TCNQ}$ in the pentacene: $\text{F}_4\text{-TCNQ}$ composite film to increase electrical conductivity. Similar to this study, many organic material based thermoelectric generators tried to overcome their low electrical conductivity.

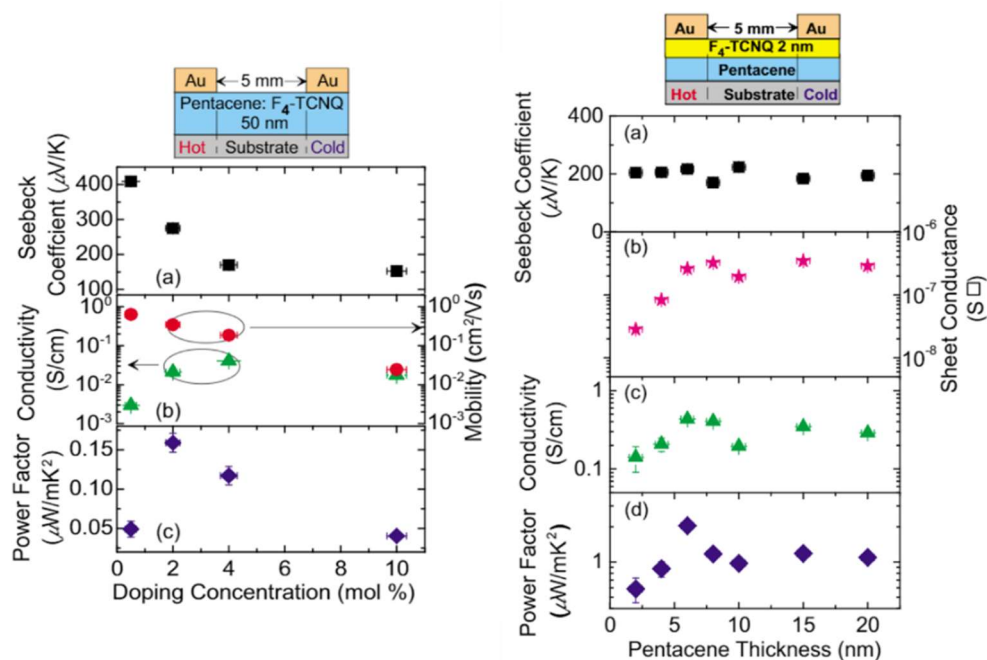


Figure 3.1.10 Structure and thermoelectric performance of an organic small molecule-based thermoelectric generator reported by Kentaro Harada et al. in 2010.

However, generally enhancing electrical conductivity cause a decrease of the Seebeck coefficient and vice versa. Therefore, recent researches are focused on suppress the side effect of enhancement of electrical conductivity or Seebeck coefficient.

	Conductivity ($\Omega^{-1} \text{cm}^{-1}$)	Seebeck coefficient ($\mu\text{V K}^{-1}$)	Power factor ($\mu\text{W m}^{-1} \text{K}^{-2}$)	Reference
C8C12-NDI/SWCNT	515.6	55.49	158.8	<i>J. Power Sources</i> , 2019, 412, 153 – 159
C8BTBT+TCNQ and SWCNTs	885.4	56.6	284.6	<i>J. Mater. Chem. A</i> , 2019, 7, 24982 – 24991
SWCNT/ZnTPP	926.7	46.9	203.8	<i>J. Power Sources</i> , 2019, 423, 152 – 158
SWCNTs/OSMS	189.4	75.9	108.4	<i>J. Mater. Chem. A</i> , 2018, 6, 8323 – 8330
SWCNT/Por-5F	982.4	53.3	279.3	<i>ACS Sustainable Chem. Eng.</i> , 2019, 7(13), 11832 – 11840
PhC ₂ Cu-1/SWCNT	666.2	55	200.2	<i>ACS Appl. Mater. Interfaces</i> , 2018, 10(6), 5603 – 5608
PDINE/SWCNT	500	52.4	112	<i>ACS Nano</i> , 2017, 11(6), 5746 – 5752
NDINE/SWCNT	400	60.2	135	<i>ACS Nano</i> , 2017, 11(6), 5746 – 5752
SWCNT/ADLA4	529.6	60.7	195.2	<i>ACS Appl. Mater. Interfaces</i> , 2019, 11(32), 29320 – 29329
CNT/PVDF+PEI	12.7	32.5	1.47	<i>Carbon</i> , 2016, 96, 778 – 781

Table 3.1.1 Recent researches on the carbon/polymer composite thermoelectric generators.

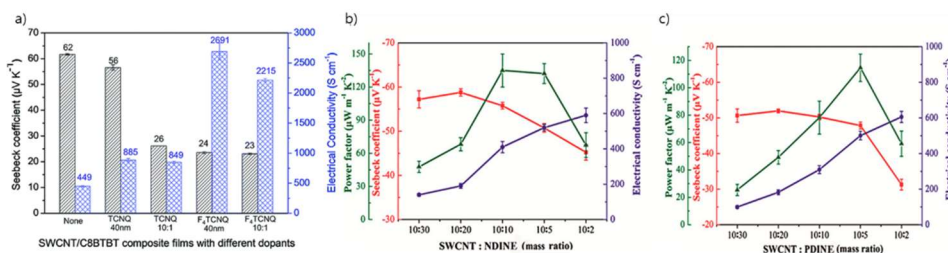


Figure 3.1.11 General relationships between the Seebeck coefficient and electrical conductivity²⁵

²⁵ *J. Mater. Chem. A*, **2019**, 7, 24982-24991 (a),
ACS Nano, **2017**, 11, 6, 5746–5752 (b, c)

3.2 Twisted small organic molecules for high thermoelectric performance of single-walled carbon nanotubes/small organic molecule hybrids through mild charge transfer interactions

3.2.1 Introduction

Single-walled carbon nanotubes (SWCNTs)/organic molecule hybrids have recently gained much attention as promising thermoelectric (TE) materials due to several advantages, such as light weight, flexibility, and solution processability.¹ The TE performance of a material is expressed by the dimensionless figure of merit, $zT = \sigma S^2 T / \kappa$, where S , σ , T , and κ are the Seebeck coefficient (V/K), electrical conductivity (S/cm), absolute temperature (K), and thermal conductivity (W/m·K), respectively.² In cases where measuring the thermal conductivity is challenging, the power factor (PF = σS^2) has been used as an

alternative TE parameter.²

Small organic molecules (SOMs) have been employed as a new type of component for SWCNTs/organic molecule hybrids,³⁻¹⁰ owing to their high Seebeck coefficient and low thermal conductivity compared to conducting polymers, such as poly(3,4-ethylenedioxythiophene)¹¹, polyaniline¹²⁻¹³, and polypyrrole¹⁴⁻¹⁵. Planar SOMs have been used as a representative component of SWCNTs/SOM hybrids because their planarity promotes non-covalent intermolecular interactions, such as π - π and charge-transfer interactions, with the SWCNTs.^{4, 6-7, 16} These interactions facilitate charge carrier transport between the SWCNTs and SOMs at the interfaces where energy difference between the highest occupied molecular orbital (HOMO) energy level of SOM and the valence band of SWCNTs can prevent low energy charge carrier transport (energy filtering effect), thus increasing the Seebeck coefficient.^{4, 17} Although the electrical conductivity of SWCNTs/planar SOM films is generally lower compared to that of pristine SWCNT films, the former exhibits superior PFs because the PF is proportional to the square of the Seebeck

coefficient. However, the aggregation of planar SOMs in SWCNTs/SOM films leads to a substantial deterioration in the electrical conductivity, and consequently, in the PF.^{3-4, 16, 18-19}

Therefore, in this study, we selected a twisted SOM, namely N,N-diphenyl-4'-(1,2,2-triphenylvinyl)-[1,1'-biphenyl]-4-amine

(TPETPA), for the following reasons. The twisted molecular structure of tetraphenylethylene (TPE) likely inhibits the aggregation of TPETPA molecules in the SWCNTs/TPETPA film.²⁰ Although the twisted structure of TPETPA would not be favourable for π - π interactions with the SWCNTs, the electron lone pair of the triphenylamine (TPA) unit of TPETPA is expected to induce mild charge transfer interactions with the antibonding π^* orbitals of the SWCNTs.²¹ Therefore, the SWCNTs/TPETPA films are expected to exhibit higher electrical conductivity than SWCNTs/planar SOM films because TPETPA would participate in efficient intermolecular interactions with the SWCNTs without forming TPETPA aggregates. In addition, the energy difference between the highest occupied molecular orbital (HOMO) energy level of TPETPA (5.05 eV) and the valence band of SWCNTs

(4.70 eV) would energy-filtering at the interfaces between TPETPA and the SWCNTs (Fig. S1), resulting in an increase in the Seebeck coefficient.^{3, 5, 16}

3.2.2 Experimental methods

Materials

All chemicals, such as 1,1,2,2-Tetraphenylethylene (TPE), triphenylamine (TPA), and hydrogen peroxide (H₂O₂, 34.5 wt%) were supplied by Alfa Aesar, Toyko Chemical Industry (TCI), and Samchun Co. Single-walled carbon nanotubes (SWCNTs, KH-SWCNT-HP) powder was purchased from KH chemicals (Korea).

Instruments

X-ray diffraction spectra of small organic molecules, SWCNTs, and SWCNTs/ small organic molecules were obtained using a SMART LAB (Rigaku) with a Cu K α radiation. Optical microscopy and a field-emission scanning electron microscopy (FE-SEM, JEOL JSM-6701F) were performed for analyzing the

morphology of SWCNTs and SWCNTs/small organic molecules. Raman spectra of SWCNTs and SWCNTs/small organic molecules were obtained using a Renishaw Invia Raman spectrometer with an Nd:YAG laser ($\lambda = 532$ nm). The charge carrier concentration and charge carrier mobility of SWCNTs and SWCNTs/small organic molecules were demonstrated using a Hall-effect measurement system (HMS-5000, Ecopia). Temperature-dependent resistance measurements for SWCNTs and SWCNTs/small organic molecules were performed with a van der Pauw method with liquid nitrogen. The energy levels of each material's valence band were obtained from photoelectron emission spectroscopy (Hitachi, High Tech AC-2)

Preparation of SWCNTs and SWCNTs/SOM films

SWCNTs powder (50 mg) was added into H₂O₂ (20 ml) solution and stirred at 334 K for 36 h. SWCNTs suspension was filtered through vacuum filtration apparatus, and the filtrate was washed with distilled H₂O (200 ml). SWCNTs solution was dispersed into tetrahydrofuran (THF, 100 ml) using a probe-type ultrasonicator

(Bandelin HD 2070, MS 72 tip, 90 % power, cycles of 0.9 s on/0.1 s off) for 6 h in an ice water bath. A solution of SWCNTs/SOM was prepared by adding various weight percentages of SOMs into the SWCNTs (fixed amount) solution. Sequentially, the SWCNTs/SOM solution was mixed using a shaker (with 100 rpm) for 3 h. The glass substrate ($20 \times 20 \times 7$ mm) was washed with distilled H₂O and isopropyl alcohol (IPA) for 15 min in a bath-type sonicator (Branson 5510), respectively, and dried in a vacuum oven for 12 h. A solution (1 mL) of SWCNTs (or SWCNTs/SOM) was dropped onto the UV/ozone cleaned glass and annealed for 30 min at 393K. The washed SWCNTs/SOM films were prepared by dipping SWCNTs/SOM films into 20 ml dichloromethane (DCM) solution for 1, 3, 5, 10, 30, and 60 min, respectively. Then, the films were dried in air condition at 353 K for 1 h.

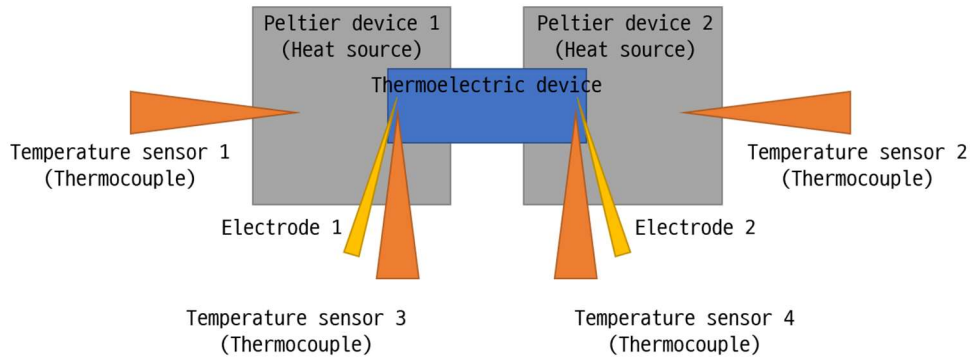
Preparation of organic thin films

A solution of 1.38 mg of each SOM (TPE, TPA, TPE+TPA, and TPETPA) dissolved in 1 ml of THF was dropped on the glass

substrate (20 mm × 20 mm) which was heated to 120°C and dried for 30 min. The glass substrates were prepared by the same procedure as in preparation of SWCNTs/SOM films.

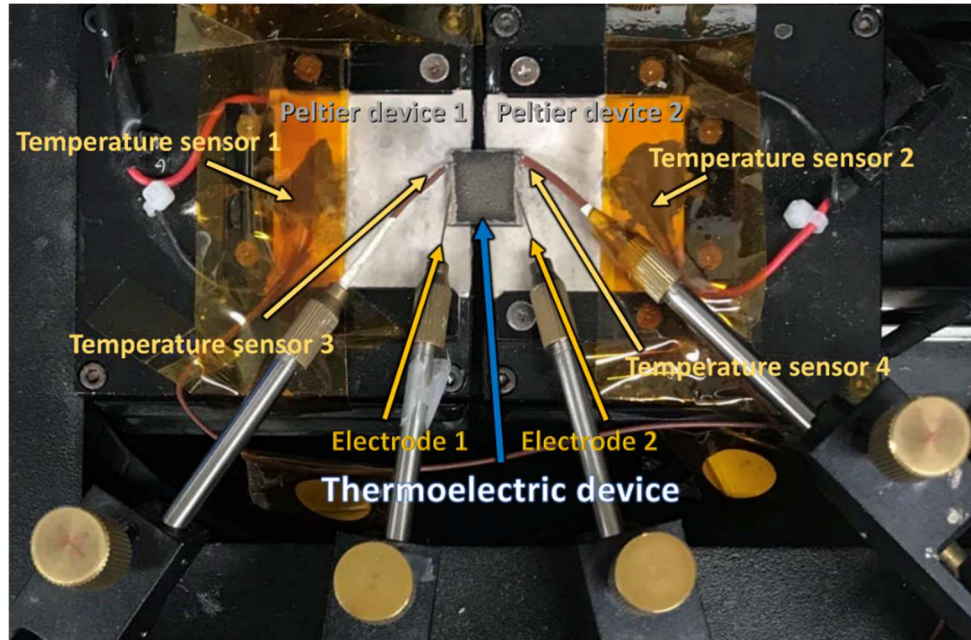
Measurement of thermoelectric properties

The temperature differences of 2, 4, 6, and 8 K were induced to the films with two sheets of the Peltier device controlled by Keithley 2604B as the power source and the source meter. The temperature of the sample's surface was measured by a Keithley 2700 multimeter system. A Keithley 6485 picoammeter and a Keithley 2182A nanovoltmeter were utilized to measure the current and the potential difference between two electrodes on the sample.



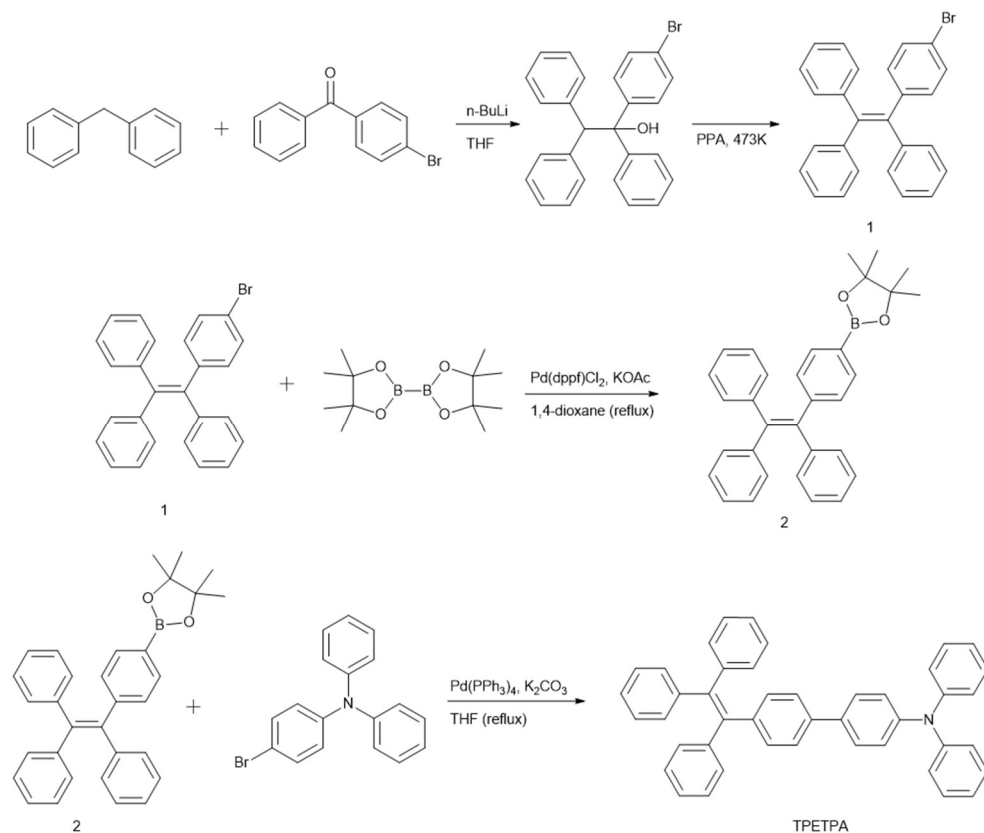
Scheme 3.2.1 Schematic illustration of the thermoelectric effect or thermoelectric generator performance measurement system.

Temperature values are measured by temperature sensors 1-4 using a Keithley 2700 multimeter system. Electrodes 1-2 are connected to the internal switching system for the measurement of potential and current with Keithley 6485 and Keithley 2182A. Two sheets of Peltier devices are functioned as a heat source (temperature controller) and they are controlled by Keithley 2640B with the feedback signals from temperature sensors through Keithley 2700.



Scheme 3.2.2 Picture of the thermoelectric effect or thermoelectric generator performance measurement system

Synthesis of TPETPA



Scheme 3.2.3 Synthetic scheme of TPETPA

1 (Bromo-TPE) Diphenylmethane (4.2 g, 25 mmol) in 100 ml of THF solution was cooled to 0°C. *n*-Butyl lithium (22 mmol, 2.5M in THF) was added to the diphenylmethane solution. After 30 minutes of stirring, 4-bromobenzophenone (5 g, 19 mmol) was added. After 12 h, crude (4-bromophenyl)-1,2,2-triphenylethan-1-ol (white powder, 6 g, 73%) was obtained by filtering. This crude

product was added to 100 ml of the polyphosphoric acid solution and heated to 200°C for 12 h. 100 ml of water added to the reaction pot and stirring 2 h. Finally, **1 (Bromo-TPE)**, 5.75 g, 77%) was gained by filtering. ¹H-NMR (300MHz, Acetone-D₆): 6.98 (d, J = 8 Hz, 2H), 7.05 -7.15 (m, 15H), 7.31 (d, J = 8 Hz, 2H)

2 (TPE-B-pin) Compound **1** (5.92 g, 14.4 mmol), bis(pinacolato) diboron (5.48g, 21.5 mmol), [1,1'-bis(diphenylphosphino)ferrocene] palladium(II) dichloride (1 g, 1.2 mmol), and potassium acetate (5.6 g, 57.6 mmol) solve in the 100 ml of 1,4-dioxane. The reaction mixture was refluxed overnight. After heating, the reaction mixture was separated with DI water and MC. The extracted solution was dried with magnesium sulfate anhydrous and filtered through Celite. Then the reaction mixture was purified with column chromatography with hexane and ethyl acetate. After vacuum drying, compound **2** was gained (**TPE-B-pin**, 5.62g, 84.8%). ¹H-NMR (400MHz, CDCl₃): 1.53 (s, 12H), 6.95-7.04 (m, 8H), 7.04-7.10 (s, 9H), 7.52 (d, J = 8 Hz, 2H)

TPETPA Compound **2** (2.5 g, 5.4 mmol) and 4-bromo triphenylamine (1.4 g, 4.2 mmol), tetrakis(triphenylphosphine)palladium(0) (240 mg, 0.2 mmol), and potassium carbonate (3.5 g, 25 mmol) solve in 100 ml of THF and 30 ml of DI water. The reaction mixture was refluxed in overnight. After heating, the reaction mixture was separated with DI water and MC. The extracted solution was dried with magnesium sulfate anhydrous and filtered through Celite. Then the reaction mixture was purified with column chromatography with hexane and ethyl acetate. After vacuum drying, an orange-colored solid (**TPETPA**, 1.4 g, 58%) was gained. ¹H-NMR (400 MHz, Acetone-D₆): 7.00-7.15 (m, 25H), 7.28 (d, J = 4 Hz, 2H), 7.30 (d, J = 4 Hz, 2H), 7.42 (d, J = 8 Hz, 2H), 7.54 (d, J = 12 Hz, 2H) ¹³C-NMR (400 MHz, Acetone-D₆): δ 147.62, 147.22, 143.75, 143.69, 142.33, 141.11, 140.67, 138.14, 134.19, 131.61, 131.09, 131.03, 129.36, 127.73, 127.68, 127.62, 127.34, 126.49, 126.45, 126.39, 125.43, 124.29, 123.61, 123.09

3.2.3 Results and discussion

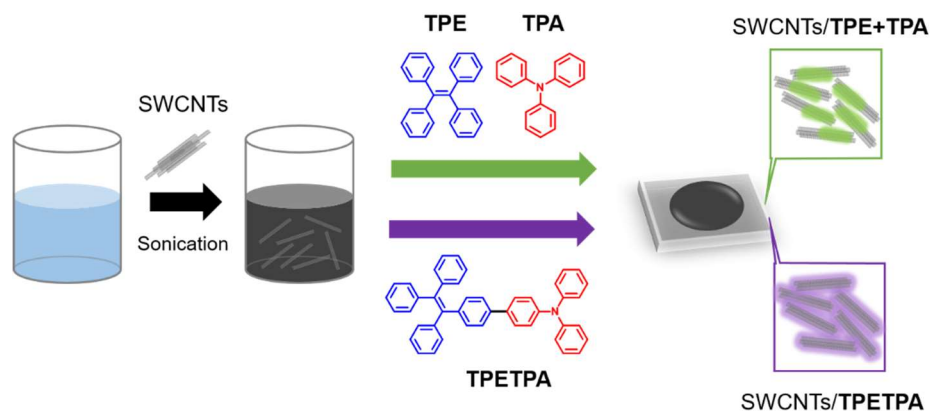


Fig. 3.2.1 Schematic illustration of the fabrication of the SWCNTs/TPE+TPA and SWCNTs/TPETPA hybrid films

To verify our hypotheses, we fabricated SWCNTs/TPE+TPA and SWCNTs/TPETPA hybrid TE films on a glass substrate, as shown in Fig. 3.2.1. Intermolecular interactions between the SOMs (TPE, TPA, and TPETPA) and the SWCNTs were investigated by obtaining photoluminescence (PL) spectra of TPE, TPA, and TPETPA films with and without SWCNTs (Fig. 3.2.2). The addition of SWCNTs to the TPE film induced partial quenching of its PL intensity, indicating weak intermolecular interactions between TPE and SWCNT bundle.^{5, 22-23} The SWCNTs/TPA and SWCNTs/TPETPA films exhibited complete quenching of the PL

intensities of the TPA and TPETPA films, respectively, These PL data suggest that the TPEPTA molecules were largely adsorbed on the SWCNTs surface and/or underwent stronger intermolecular interactions with SWCNTs than TPE, presumably due to the TPA moiety. As shown in Fig. 3.2.3, the X-ray diffraction (XRD) pattern of the TPE+TPA film exhibited diminished TPA diffraction peaks and noticeably decreased TPE diffraction peaks. Furthermore, the XRD pattern of the SWCNTs/TPE+TPA film was similar to that of the SWCNTs film (Fig. 3.2.4 (b)). These results imply that amorphous aggregates of TPE+TPA are possibly formed in SWCNTs/TPE+TPA because TPE likely interacts more favourably with TPA than with SWCNTs. Therefore, the SWCNTs/TPE+TPA film can be used as a control sample for the SWCNTs/TPETPA film to examine the effect of intermolecular interactions between TPETPA and the SWCNT bundles on the TE performance.

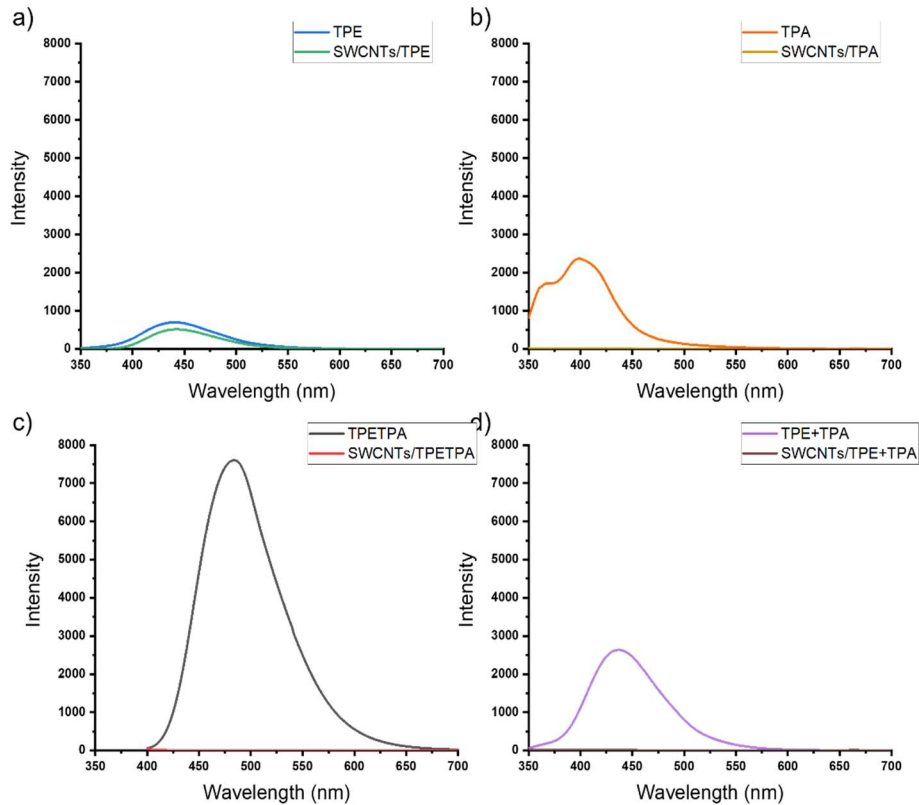


Fig. 3.2.2 The emission intensity of a) TPE, SWCNTs/TPE, b) TPA, SWCNTs/TPA, c) TPETPA, SWCNTs/TPETPA, and d) TPE+TPA, SWCNTs/TPE+TPA in thin film state. The blend ratio of SWCNTs/SOM is 13.8% (the mass fraction providing the maximum power factor). Excitation wavelengths are 385 nm for TPETPA and 332 nm for TPA, TPA, TPE+TPA.

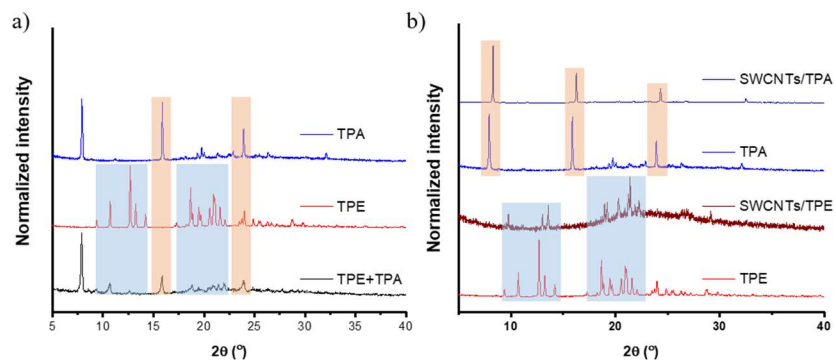


Fig. 3.2.3 Two sets of X-ray diffraction (XRD) spectra: a) XRD spectra of TPA, TPE, and TPE+TPA in film state, b) XRD spectra of SWCNTs/TPA, TPA, SWCNTs/TPE, and TPE in film state

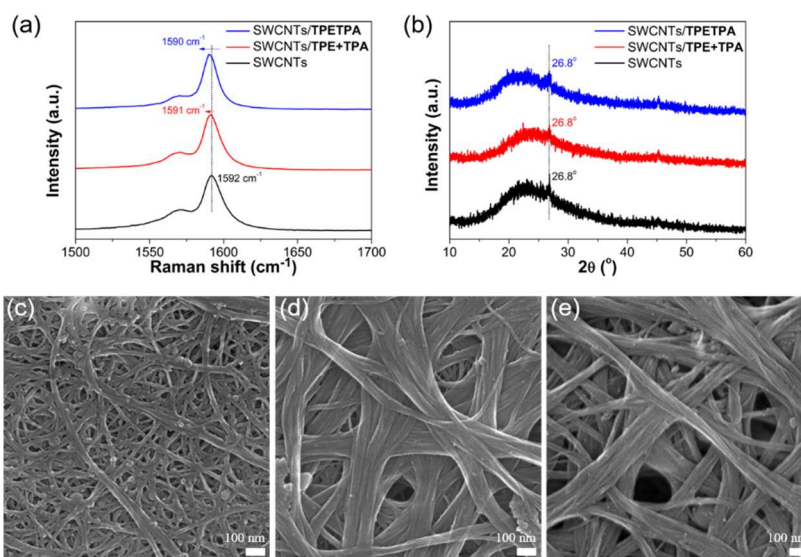


Fig. 3.2.4 Two sets of X-ray diffraction (XRD) spectra: a) XRD spectra of TPA, TPE, and TPE+TPA in film state, b) XRD spectra of SWCNTs/TPA, TPA, SWCNTs/TPE, and TPE in film state

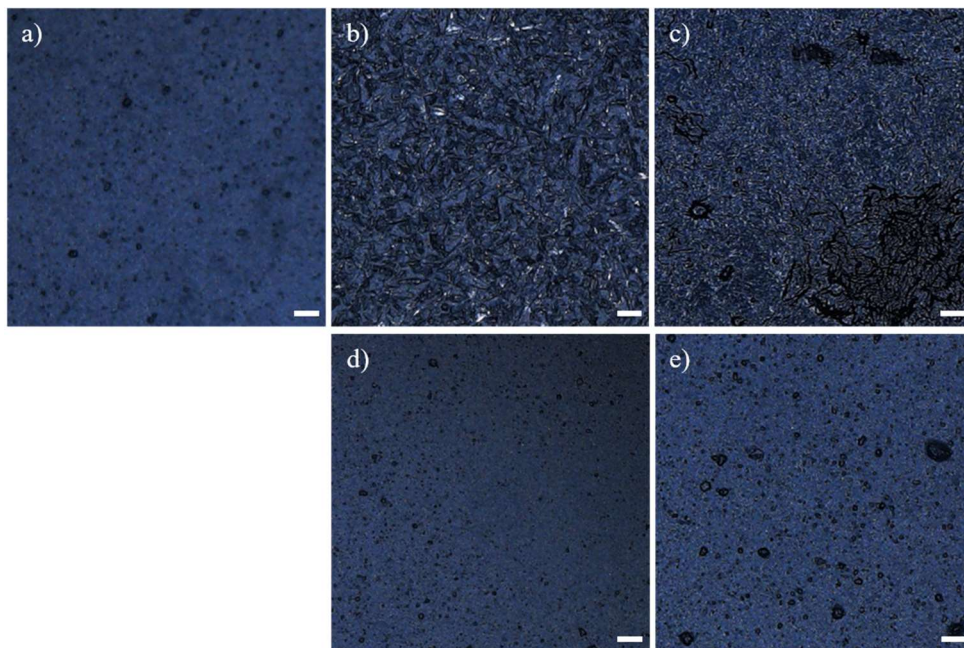


Fig. 3.2.5 Optical microscopic images of a) SWCNTs, b) SWCNTs/TPE, c) SWCNTs/TPA, d) SWCNTs/TPE+TPA and e) SWCNTs/TPETPA. The scale bar is 100 μm .

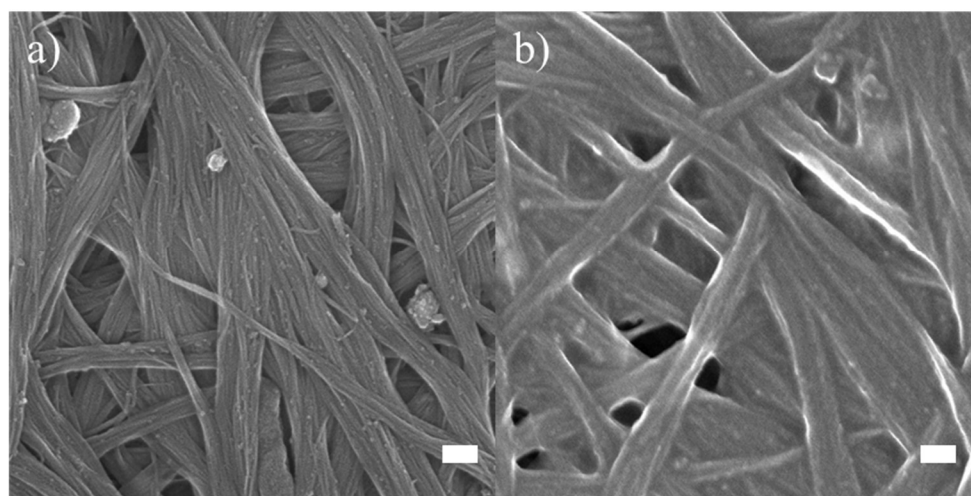


Fig. 3.2.6 FE-SEM images of (a) SWCNTs/TPE+TPA and (b) SWCNTs/TPETPA films. The scale bar is 100 nm. The mass fraction of TPE+TPA (or TPETPA) is 56.9 wt%.

Raman spectroscopy was used to characterise the charge transfer interactions between the SWCNTs and TPETPA (or TPE+TPA). The G-band of the pristine SWCNTs was observed at 1592 cm^{-1} (Fig. 3.2.4(a)), which is related to C=C stretching in the graphitic sheet.²⁴ The G-band of SWCNTs/TPE appeared at the same position as that of the pristine SWCNTs, while SWCNTs/TPA gave rise to a down-shifted G-band at 1590 cm^{-1} (Fig. S4). This shift was attributed to electron transfer from the lone pair of electrons of TPA to the antibonding π^* orbitals of the SWCNTs, confirming that charge transfer interactions occur between TPA and SWCNTs.^{21, 25} As shown in Fig. 3.2.4(a), the G-band of SWCNTs/TPETPA (1590 cm^{-1}) was down-shifted to a greater extent than that of SWCNTs/TPE+TPA (1591 cm^{-1}), indicating that intermolecular interactions (i.e. charge transfer interactions) are stronger within the former hybrid film.

XRD and field-emission scanning electron microscopy (FE-SEM) analyses were performed to investigate the structure and morphology of the SWCNTs/TPE+TPA and SWCNTs/TPETPA films. As shown in Fig. 3.2.4(b), the SWCNTs gave rise to a

diffraction peak at 26.83° along the (002) plane, which is a fingerprint of the inter-graphitic layer spacing.²⁶ The diffraction patterns corresponding to the pristine SWCNTs were the same in SWCNTs/TPE+TPA and SWCNTs/TPETPA as those of pristine SWCNTs, indicating that the hybridisation of SWCNTs with TPETPA (or TPE+TPA) did not affect the π - π stacking between individual SWCNTs in the bundle. In addition, the diagnostic peaks for TPE and TPA appeared in the SWCNT/TPE and SWCNT/TPA diffraction pattern (Fig. 3.2.3), while those of the TPE+TPA film were not visible in the SWCNTs/TPE+TPA diffraction pattern (Fig. 3.2.4(b)). These results imply that TPE and TPA interact with each other to form amorphous aggregates of TPE+TPA in the presence of SWCNTs. This was corroborated by the optical microscopic images, wherein TPE or TPA aggregates were observed on the surfaces of the SWCNTs of SWCNT/TPE and SWCNT/TPA, while the optical image of SWCNTs/TPE+TPA was similar to that of the pristine SWCNTs (Fig. 3.2.5). FE-SEM images revealed that the addition of TPETPA (or TPE+TPA) increased the SWCNT bundle diameter, indicating that the

adsorption of TPETPA (or TPE+TPA) enhanced interconnection between the SWCNT bundles (Fig. 3.2.4(c)–(e) and Fig. 3.2.6). As shown in Fig. 3.2.7, the Seebeck coefficients of the SWCNTs/TPE and SWCNTs/TPA films were similar over the entire mass fraction range of each SOM, while the electrical conductivities of SWCNTs/TPE film were relatively higher than those of SWCNTs/TPA film. As a result, the SWCNTs/TPE@13.8wt% film exhibited increased PF compared to SWCNTs/TPA@13.8wt% film. These results suggested that a twisted molecule (TPE) can be used as a component for efficient SWCNTs/SOM TE hybrid materials. The TE performance of SWCNTs/TPETPA film can be further improved due to enhanced intermolecular interactions between them.

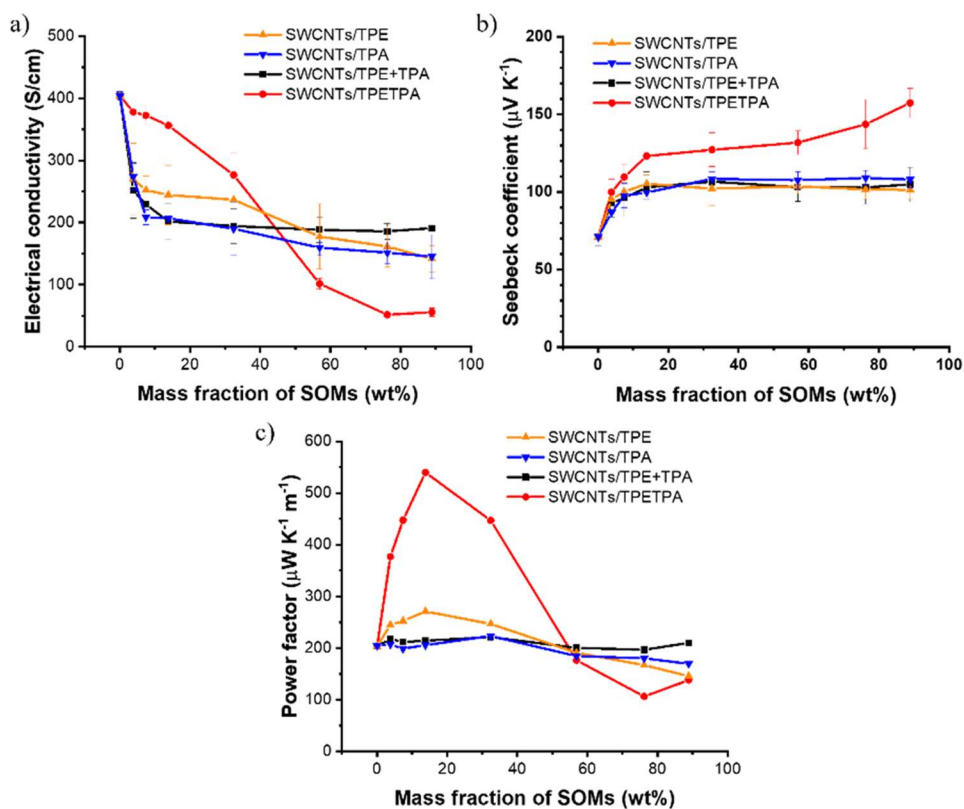


Fig. 3.2.7 TE properties of the SWCNTs/TPE, SWCNTs/TPA, SWCNTs/TPE+TPA, and SWCNTs/TPETPA films: (a) Electrical conductivity, (b) Seebeck coefficient, and (c) PF. The solid lines are eye visual guides

The relationship between the TE properties of the pristine SWCNTs, SWCNTs/TPE+TPA, and SWCNTs/TPETPA films, and their SOM mass fraction was evaluated (Fig. 3.2.8). The Seebeck coefficient increased from $71.0 \pm 5.5 \mu\text{V/K}$ in the pristine SWCNTs to $103.1 \pm 10.1 \mu\text{V/K}$ in SWCNTs/TPE+TPA@13.8 wt%, while the electrical conductivity decreased from $404.1 \pm 6.9 \text{ S/cm}$ (pristine SWCNTs) to $201.8 \pm 28.7 \text{ S/cm}$ (SWCNTs/TPE+TPA@13.8 wt%). Above a mass fraction of 13.8 wt%, the Seebeck coefficient and electrical conductivity values of SWCNTs/TPE+TPA plateaued (Fig. 3.2.8(a-b)). However, the SWCNTs/TPETPA films exhibited different trends. At a TPETPA mass fraction of 13.8 wt%, the Seebeck coefficient of SWCNTs/TPETPA increased to $123.2 \pm 6.8 \mu\text{V/K}$, and the electrical conductivity decreased to $356.2 \pm 17.8 \text{ S/cm}$. Above 13.8 wt% TPETPA, the Seebeck coefficient of SWCNTs/TPETPA further increased to $157.0 \pm 9.5 \mu\text{V/K}$ (SWCNTs/TPETPA@88.9 wt%), while the electrical conductivity decreased to $55.7 \pm 6.9 \text{ S/cm}$. Thus, the SWCNTs/TPEPTA film provided the highest PF value of $539.8 \mu\text{W/m}\cdot\text{K}^2$ at 13.8 wt%, which is 266% higher than

that of the SWCNTs film ($203.9 \mu\text{W}/\text{m}\cdot\text{K}^2$). The PF ($221.1 \mu\text{W}/\text{m}\cdot\text{K}^2$) of SWCNTs/TPE+TPA was similar to that of the pristine SWCNTs. The PF value of SWCNTs/TPETPA was higher than that of SWCNTs/TPE+TPA as a result of enhanced electrical conductivity and the higher Seebeck coefficient of the former, at a mass fraction of 13.8 wt% (the mass fraction providing the maximum power factor). Notably, the electrical conductivity of the SWCNT/TPETPA films exhibited a dramatic decrease upon the addition of more than 13.8 wt% of TPETPA, and the Seebeck coefficient increased continuously with increasing TPETPA content. In case of SWCNTs/TPE+TPA, the electrical conductivity decreased and the Seebeck coefficient increased until a TPE+TPA mass fraction of 13.8 wt%. Therefore, the TE properties of SWCNTs/TPETPA (or TPE+TPA) films can be divided into two regions: up to 13.8 wt% of SOMs (region I) and over 13.8 wt% of SOMs (region II), as shown in Fig. 3.2.8.

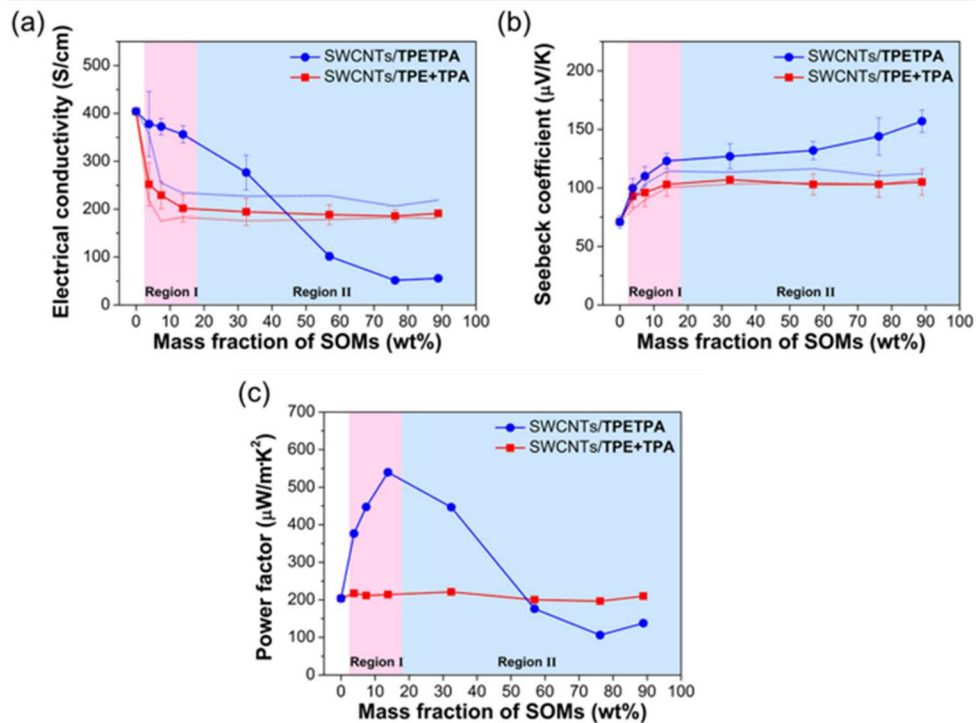


Fig. 3.2.8 TE properties of the pristine SWCNTs, SWCNTs/TPE+TPA, and SWCNTs/TPETPA films: (a) Electrical conductivity, (b) Seebeck coefficient, and (c) PF. The red line corresponds to the SWCNTs/TPE+TPA film and the blue line the SWCNTs/TPETPA. Power factor was calculated from average values of the Seebeck coefficient and electrical conductivity of the SWCNTs/TPE+TPA and SWCNTs/TPETPA films. Dotted lines are electrical conductivities and Seebeck coefficients of washed SWCNTs/TPE+TPA and SWCNTs/TPETPA films obtained by dipping into dichloromethane (20 ml) bath for 60 min.

As mentioned above, intermolecular interactions, including charge transfer and π - π interactions, between SOMs and SWCNT bundles enhance the TE performance of SWCNT/SOM films. At a high mass fraction of TPETPA (or TPE+TPA) in region II, SWCNTs/TPETPA (or TPE+TPA) films would inevitably contain excess TPETPA (or TPE+TPA), as observed in the SEM images of SWCNTs/TPETPA (or TPE+TPA)@56.9 wt% (Fig. 3.2.6). The contrast in the TE performance trends of the two hybrid films in the two regions can be attributed to the differences in the intermolecular interactions between the SWCNTs and the two types of SOMs. To gain insight into the TE characteristics in each region, we dipped the SWCNTs/TPETPA and SWCNTs/TPE+TPA films into a dichloromethane (good solvent) bath to remove excess TPETPA (or TPE+TPA) (Fig. S8). The resultant films are referred to as washed SWCNTs/TPETPA and SWCNTs/TPE+TPA films, respectively. The electrical conductivities and Seebeck coefficients of the two washed films were measured (red and blue dotted lines in Fig. 3.2.8). When the mass fraction of TPETPA (or

TPE+TPA) was less than 13.8 wt% (region I), the electrical conductivities and Seebeck coefficients of both washed hybrid films were lower than those of their untreated counterparts. During the washing process, excess TPETPA (or TPE+TPA) molecules weakly bound to the SWCNTs are desorbed from the bundles and removed from the SWCNTs/SOM film, which likely disrupts the bundle networks, leading to decreased electrical conductivities and Seebeck coefficients in region I. Washed SWCNTs/TPETPA films displayed higher electrical conductivities at TPETPA mass fractions above 40 wt%, but lower Seebeck coefficients above 13.8 wt% TPETPA, compared to that of their unwashed counterparts. However, the electrical conductivities and Seebeck coefficients of the washed SWCNTs/TPE+TPA films were similar to those of their unwashed counterparts at TPE+TPA mass fractions above 13.8 wt%. As a result, in case of SWCNTs/TPETPA films, the variations in the electrical conductivities and Seebeck coefficients before and after washing process were larger than SWCNTs/TPE+TPA films. These results suggest that TPETPA exerts a greater effect on charge

carrier transport than TPE+TPA. We assumed that energy-filtering between TPEPTA and SWCNTs occurs more effectively than between TPE+TPA in region II. It could be attributed to mild charge transfer interactions between TPETPA and SWCNTs, which can facilitate charge carrier transport between them. Note that the SWCNTs exhibited stronger charge transfer interactions with TPETPA than with TPE+TPA, as revealed by Raman spectroscopy.

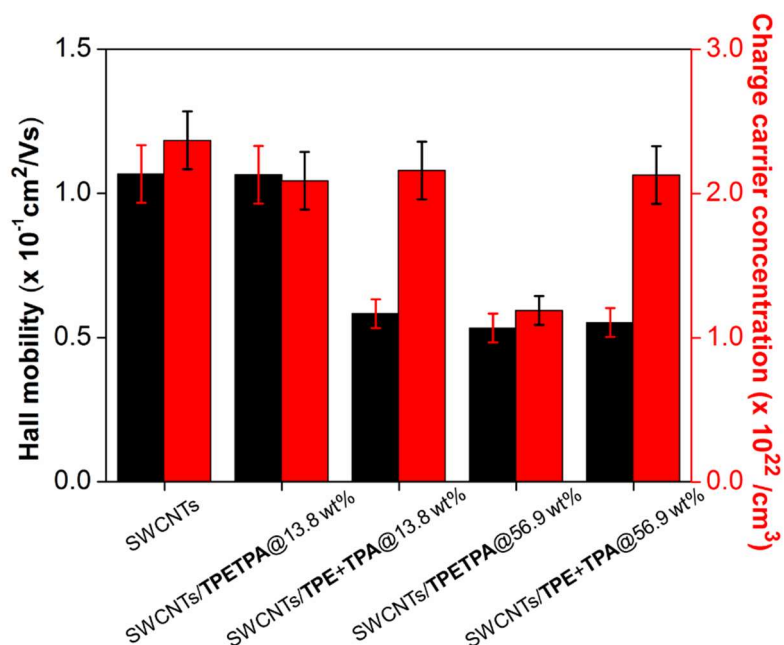


Fig. 3.2.9 Hall mobilities and charge carrier concentrations of the pristine SWCNTs, SWCNTs/TPE+TPA, and SWCNTs/TPETPA films.

To get insight into energy-filtering effect in the two hybrid films, we obtained the Hall mobility and charge carrier concentration of the SWCNTs, SWCNTs/TPE+TPA, and SWCNTs/TPETPA using a Hall effect measurement system (Fig. 3.2.9). The Hall mobility of SWCNTs/TPETPA@13.8 wt% ($1.06 \times 10^{-1} \text{ cm}^2 \text{ V}^{-1} \text{ s}^{-1}$) was similar to that of the pristine SWCNTs ($1.07 \times 10^{-1} \text{ cm}^2 \text{ V}^{-1} \text{ s}^{-1}$) but higher than that of SWCNTs/TPE+TPA@13.8 wt% ($0.58 \times 10^{-1} \text{ cm}^2 \text{ V}^{-1} \text{ s}^{-1}$). The charge carrier concentration of SWCNTs/TPETPA@13.8 wt% ($2.09 \times 10^{22} \text{ cm}^{-3}$) was lower than those of the pristine SWCNTs ($2.37 \times 10^{22} \text{ cm}^{-3}$) and SWCNTs/TPE+TPA@13.8 wt% ($2.16 \times 10^{22} \text{ cm}^{-3}$), indicating that charge carrier scattering between SWCNTs and TPETPA occurs more than between SWCNTs and TPE+TPA.¹⁷ Therefore, SWCNTs/TPETPA exhibited higher electrical conductivity and Seebeck coefficients than SWCNTs/TPE+TPA in region I, resulting in higher PF values. The SWCNTs/TPETPA film exhibited dramatic decreases in Hall mobility and charge carrier concentration at a mass fraction of 56.9 wt% ($0.53 \times 10^{-1} \text{ cm}^2 \text{ V}^{-1} \text{ s}^{-1}$ and $1.19 \times 10^{22} \text{ cm}^{-3}$, respectively). However, the charge carrier

concentration of SWCNTs/TPE+TPA@56.9 wt% ($2.13 \times 10^{22} \text{ cm}^{-3}$) was comparable to that of SWCNTs/TPE+TPA@13.8 wt% ($2.16 \times 10^{22} \text{ cm}^{-3}$). This result indicates that excess TPE+TPA does not participate in charge carrier transport, resulting in the saturation of the Seebeck coefficient of SWCNTs/TPE+TPA in region II. As mentioned above, the energy difference between the valence band of SWCNTs and the HOMO energy level of TPEPTA (or TPE+TPA) can induce energy filtering at the interfaces, resulting in larger Seebeck coefficient of SWCNT/TPETPA than SWCNTs/TPE+TPA and lower charge carrier concentration of SWCNTs/TPETPA than SWCNTs/TPE+TPA.

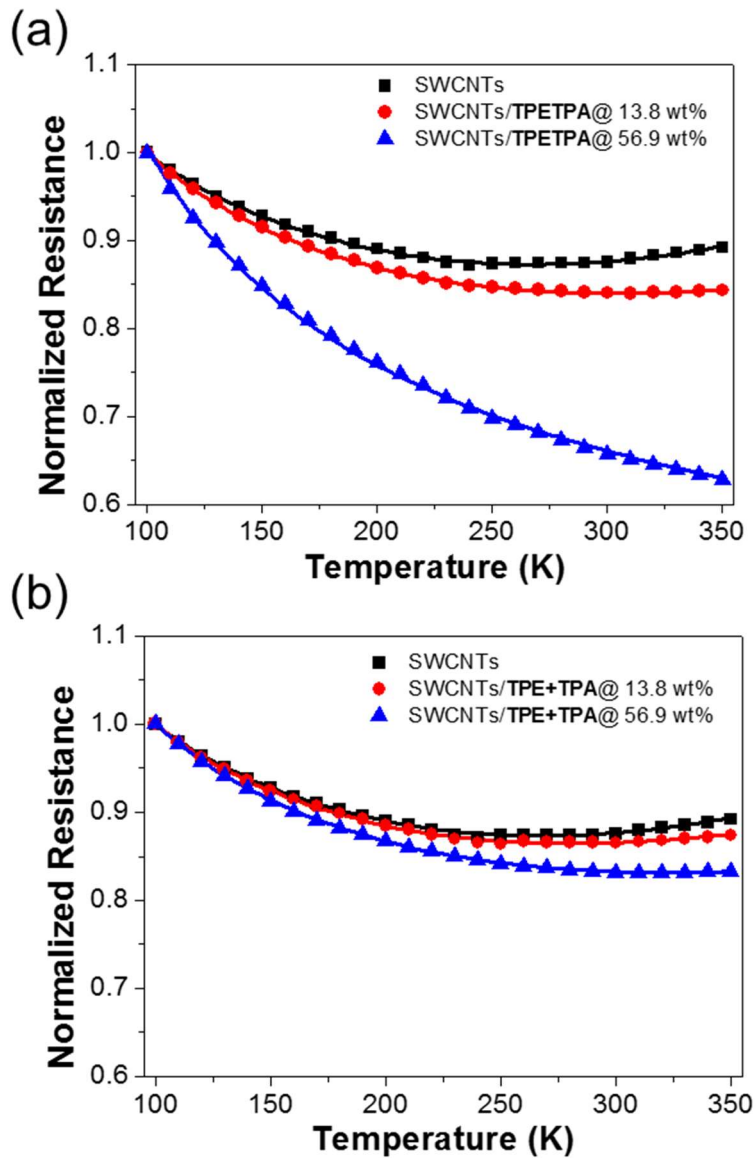


Fig. 3.2.10 Normalised temperature-dependent resistances of (a) the pristine SWCNTs and SWCNTs/TPETPA films, and (b) SWCNTs and SWCNTs/TPE+TPA films. The solid lines represent best-fit lines and details are described in the supporting information.

To gain a deeper insight into the energy filtering effect of the hybrid films, their charge carrier transport behaviour was evaluated by measuring temperature-dependent resistances. Fig. 3.2.10 shows the normalised temperature-dependent resistances of the SWCNTs, SWCNTs/TPE+TPA, and SWCNTs/TPETPA. The normalised resistance of the pristine SWCNTs film decreased with increasing temperature from 100 to 250 K. At temperatures above 250 K, the normalised resistance of the SWCNTs film increased, indicating metallic conduction. This result was well fitted to the heterogeneous model²⁷⁻²⁸ in which metallic conduction and variable-range hopping (VRH) conduction coexist, as described in Equation 1:

$$R(T) = \alpha R_m e^{-\frac{T_m}{T}} + \beta R_s e^{\left(\frac{T_0}{T}\right)^{1/D+1}} \quad (\text{Eq. 1})$$

where α and β are geometry factors related to the relative contributions of metallic and VRH conduction, respectively; R_m and R_s are intrinsic resistances; T_m and T_0 are the characteristic temperatures (K) for metallic and VRH conduction, respectively; and T and D are the absolute temperature and dimensionality for

hopping in VRH conduction, respectively. In the heterogeneous model, conductive crystalline regions are separated by relatively poorly conducting disordered regions.²⁷⁻²⁹ The normalised temperature-dependent resistances of SWCNTs/TPETPA@13.8 wt% and SWCNTs/TPE+TPA@13.8 wt% were also well fitted to the heterogeneous model, and provided relatively smaller temperature-normalised resistance slopes (K^{-1}) than those of the SWCNTs in the temperature range of 250 to 350 K. Therefore, the αR_m values of SWCNTs/TPETPA@13.8 wt% and SWCNTs/TPE+TPA@13.8 wt% are smaller than that of the SWCNTs, indicating a lesser contribution from metallic conduction in the hybrid films. This is caused by the adsorption of TPETPA (or TPE+TPA) onto the SWCNT bundles, which leads to increased charge carrier transport between them. (Table 3.2.1)³⁰⁻³¹

The SWCNTs/TPE+TPA@56.9 wt% film still exhibited metallic conduction in the 300–350 K range, while VRH conduction was well fitted for SWCNTs/TPETPA@56.9 wt% in the range of 100–350 K. In addition, SWCNTs/TPETPA@13.8 wt% showed a relatively smaller temperature-resistance slope compared to that of

SWCNTs/TPE+TPA@13.8 wt%, in the range of 250 to 350 K. These results confirm that energy filtering between SWCNTs and TPETPA occurs more efficiently than it does between SWCNTs and TPE+TPA.^{29, 31} It can be ascribed to the fact that mild charge transfer interactions between TPETPA and the SWCNTs can facilitate charge carrier transport between them, which leads to more effective energy filtering effect in SWCNTs/TPETPA compared to that in SWCNTs/TPE+TPA. This is supported by the T_0 values of SWCNTs/TPETPA@13.8 wt% and @56.9 wt%, which were higher than those of SWCNTs/TPE+TPA@13.8 wt% and @56.9 wt%. Therefore, the former exhibited more effective energy-dependent charge carrier scattering than the latter, resulting in higher Seebeck coefficients.³¹⁻³²

Based on these charge carrier transport results, we suggest distinct charge transport characteristics of the SWCNTs, SWCNTs/TPETPA, and SWCNTs/TPE+TPA, as shown in Fig. 3.2.11. Upon hybridisation of the SWCNTs with TPE+TPA, charge carrier transport between the SWCNT bundles (SWCNTs) is dominant because TPE+TPA interact poorly with the SWCNTs.

In the case of the SWCNTs/TPETPA film, mild charge transfer interactions induce favourable charge carrier transport between the SWCNTs and TPETPA. Therefore, energy-filtering occurs more efficiently in the SWCNTs/TPETPA film than in the SWCNTs/TPE+TPA film, which leads to a higher Seebeck coefficient in the former. Consequently, TPETPA significantly increased the Seebeck coefficient of the SWCNTs/TPETPA film and minimised the decrease in the electrical conductivity, thus providing the highest PF values among the tested SWCNT/SOM hybrid TE materials (Table 3.2.2). Based on the previous reports on in-plane thermal conductivity values of SWCNTs and SWCNTs/organic molecule hybrids (Table 3.2.3), ZT of SWCNTs/TPETPA@13.8wt% could be in a range from 0.026 to 0.61 at 300 K.

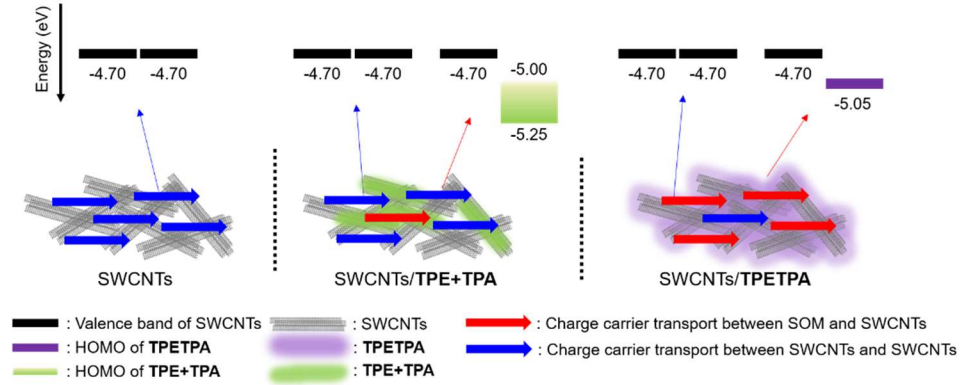


Fig. 3.2.11 Schematic illustration of charge carrier transport behaviour in the pristine SWCNTs (left), SWCNTs/TPE+TPA (middle), and SWCNTs/TPETPA (right) films.

Films	Fitting parameters				
	αR_m^b	βR_s^b	$T_m (K)$	$T_0 (K)$	D
Pristine SWCNTs	2.35	0.55	1189.19	21.28	2
SWCNTs/TPE+TPA @13.8 wt%	1.49	0.53	1077.89	24.66	2
SWCNTs/TPETPA @13.8 wt%	1.13	0.49	1021.08	36.73	2
SWCNTs/TPE+TPA @56.9 wt%	1.00	0.49	1041.55	37.47	2
SWCNTs/TPETPA @56.9 wt% ^a	-	0.25	-	258.77	2

Table 3.2.1 Fitting parameters of normalised temperature-dependent resistances of the pristine SWCNTs, SWCNTs/TPE+TPA, and SWCNTs/TPETPA films. a) Normalised temperature dependent resistance of SWCNTs/TPETPA@56.9 wt% film was well fitted with the VRH conduction model. b) Normalised value

Sample	Electrical conductivity (S/cm)	Seebeck coefficient ($\mu\text{V/K}$)	Power factor ($\mu\text{W/m}\cdot\text{K}$)	Reference
SWCNTs/ C ₈ C ₁₂ -NDI ^{a)}	515.6	55.49	158.8	33
TCNQ ^{c)} doped SWCNTs/C ₈ BTBT ^{b)}	885.4	56.6	284.6	34
SWCNTs/ZnTPPD ^{d)}	926.7	46.9	203.8	35
SWCNTs/TCzPy ^{e)}	189.4	75.9	108.4	36
SWCNTs/Por-5F ^{f)}	982.4	53.3	279.3	37
SWCNTs/ PhC ₂ Cu ^{g)}	666.2	55	200.2	38
SWCNTs/HAT6 ^{h)}	1286.9	56.5	408.2	39

Table 3.2.2 TE performance of previously reported p-type SWCNTs/SOMs hybrids

- a) Naphthalenediimide with branched alkyl chain; b) 7,7,8,8-Tetracyanoquinodimethane; c) 2,7-Dioctyl[1]benzothieno[3,2-b][1]benzothiophene; d) Zinc Porphyrin ; e) 1,3,6,8-tetrakis(3,6-di-tert-butyl-9H-carbazol-9-yl)pyrene; f) 5,10,15,20-Tetrakis(perfluorophenyl)porphyrin; g) Copper-phenylacetylide; h) 2,3,6,7,10,11-hexakis(hexyloxy)triphenylene

Sample	In-plane thermal conductivity (S/cm)	Reference
SWCNTs	20	40
SWCNTs	24	41
SWCNTs	35	42
SWCNTs/P3HT	0.43	43
SWNT/Flavin derivative	62.1	44
SWCNT/PEDOT:PSS	0.25	45

Table 3.2.3 In-plane thermal conductivity of SWCNTs and SWCNTs/organic molecule-based TE hybrids

3.2.4 Conclusion

In conclusion, we have demonstrated that the hybridisation of SWCNTs with a twisted SOM, such as TPETPA, significantly improved the TE performance of the resultant hybrid film. Mild charge transfer interactions between the SWCNT bundles and TPETPA facilitated charge carrier transport between them, thereby increasing the Seebeck coefficient and minimising the trade-off reduction in electrical conductivity of the SWCNTs/TPETPA film. Thus, SWCNTs/TPETPA@13.8 wt% exhibited a dramatic increase in the Seebeck coefficient ($123.2 \pm 6.8 \mu\text{V/K}$) and a slight decrease in electrical conductivity ($356.2 \pm 17.8 \text{ S/cm}$) compared to the values obtained for the pristine SWCNTs film ($71.0 \pm 5.5 \mu\text{V/K}$ and $404.1 \pm 6.9 \text{ S/cm}$, respectively). The PF of the SWCNTs/TPETPA@13.8 wt% film was $539.8 \mu\text{W/m}\cdot\text{K}^2$, which is 266% larger than that of the pristine SWCNTs film ($203.9 \mu\text{W/m}\cdot\text{K}^2$). This is the highest PF value among the SWCNTs/SOM-based TE films known to date. Our findings suggest that twisted SOMs are a promising alternative to planar

SOMs in the development of high-performance SWCNTs/SOM-based TE materials.

In this work, we achieve a considerable enhancement in the power factor from $203.9 \mu\text{W}\cdot\text{K}^{-2}\cdot\text{m}^{-1}$ to $539.8 \mu\text{W}\cdot\text{K}^{-2}\cdot\text{m}^{-1}$ at SWCNTs/TPETPA (13.8 wt%) with blending glassy like amorphous organic material TPETPA and SWCNTs. This significant enhancement in the power factor is achieved by an increment of the Seebeck coefficient ($71 \mu\text{V}\cdot\text{K}^{-1}$ to $123 \mu\text{V}\cdot\text{K}^{-1}$, +72.4%) with a little decrement of the electrical conductivity ($404 \Omega^{-1}\cdot\text{cm}^{-2}$ to $356 \Omega^{-1}\cdot\text{cm}^{-2}$, -11.9%). It results from glass-like amorphous TPETPA, which binds SWCNTs and filters electron flow by its low-lying energy level through the entire composite film. Therefore, we find out that glass-like amorphous organic material is more proper to thermoelectric for the organic hybrid system.

3.2.5 References and notes

1. J. L. Blackburn, A. J. Ferguson, C. Cho and J. C. Grunlan,

- Adv. Mater.*, 2018, **30**, 1704386
2. G. J. Snyder and E. S. Toberer, *Nat. Mater.*, 2008, **7**, 105-114
 3. X. Yin, Y. Peng, J. Luo, X. Zhou, C. Gao, L. Wang and C. Yang, *J. Mater. Chem A*, 2018, **6**, 8323-8330
 4. T.-h. Kim, J. G. Jang and J.-I. Hong, *J. Mater. Chem C*, 2020, **8**, 12795-12799.
 5. J. G. Jang, S. Y. Woo, H. Lee, E. Lee, S. H. Kim and J.-I. Hong, *ACS Appl. Mater. Interfaces*, 2020, **12**, 51387-51396
 6. J. Tan, Z. Chen, D. Wang, S. Qin, X. Xiao, D. Xie, D. Liu and L. Wang, *J. Mater. Chem A*, 2019, **7**, 24982-24991
 7. Y. Chen, S. Qu, W. Shi, Q. Yao and L. Chen, *Carbon*, 2020, **159**, 471-477
 8. Y. Zhang, Q. Zhang and G. Chen, *Carbon Energy*, 2020, **2**, 408-436
 9. C.-J. Yao, H.-L. Zhang and Q. Zhang, *Polymers*, 2019, **11**, 107
 10. Z. Sun, J. Li and W. Y. Wong, *Macromol. Chem. Phys.*, 2020, **221**, 2000115

- 11.L. Zhang, Y. Harima and I. Imae, *Org. Electron.*, 2017, **51**, 304-307
- 12.J. Chen, L. Wang, X. Gui, Z. Lin, X. Ke, F. Hao, Y. Li, Y. Jiang, Y. Wu and X. Shi, *Carbon*, 2017, **114**, 1-7
- 13.Q. Yao, L. Chen, W. Zhang, S. Liufu and X. Chen, *Acs Nano*, 2010, **4**, 2445-2451
- 14.S. Wang, Y. Zhou, Y. Liu, L. Wang and C. Gao, *J. Mater. Chem C*, 2020, **8**, 528-535.
- 15.J. Wu, Y. Sun, W.-B. Pei, L. Huang, W. Xu and Q. Zhang, *Synth. Met.*, 2014, **196**, 173-177
- 16.X. Li, Z. Yu, H. Zhou, F. Yang, F. Zhong, X. Mao, B. Li, H. Xin, C. Gao and L. Wang, *ACS Sustain. Chem. Eng.*, 2021, **9**, 1891-1898
- 17.C. Gayner and Y. Amouyal, *Adv. Funct. Mater.*, 2020, **30**, 1901789
- 18.Y. Zhou, X. Yin, Y. Liu, X. Zhou, T. Wan, S. Wang, C. Gao and L. Wang, *ACS Sustain. Chem. Eng.*, 2019, **7**, 11832-11840.
- 19.Y. Zhou, Y. Liu, X. Zhou, Y. Gao, C. Gao and L. Wang, *J.*

- Power Sources*, 2019, **423**, 152-158.
- 20.R. Isci, E. Tekin, K. Kaya, S. P. Mucur, S. F. Gorkem and T. Ozturk, *J. Mater. Chem C*, 2020, **8**, 7908-7915.
- 21.C. Gao, Y. Liu, Y. Gao, Y. Zhou, X. Zhou, X. Yin, C. Pan, C. Yang, H. Wang and G. Chen, *J. Mater. Chem A*, 2018, **6**, 20161-20169.
- 22.J. Zou, L. Liu, H. Chen, S. I. Khondaker, R. D. McCullough, Q. Huo and L. Zhai, *Adv. Mater.*, 2008, **20**, 2055-2060
- 23.P. J. Goutam, D. K. Singh and P. K. Iyer, *J. Phys. Chem. C*, 2012, **116**, 8196-8201
- 24.R. Saito, M. Hofmann, G. Dresselhaus, A. Jorio and M. Dresselhaus, *Adv. Phys.*, 2011, **60**, 413-550
- 25.R. Rao, N. Pierce and A. Dasgupta, *Appl. Phys. Lett.*, 2014, **105**, 073115
- 26.Z. Li, C. Lu, Z. Xia, Y. Zhou and Z. Luo, *Carbon*, 2007, **45**, 1686-1695
- 27.A. Kaiser, G. Düsberg and S. Roth, *Phys. Rev. B* 1998, **57**, 1418
- 28.A. B. Kaiser and V. Skakalova, *Chem. Soc. Rev.*, 2011, **40**, 143

3786-3801

- 29.H. Li, S. Liu, P. Li, D. Yuan, X. Zhou, J. Sun, X. Lu and C. He, *Carbon*, 2018, **136**, 292-298.
- 30.E. Kymakis and G. A. Amaratunga, *J. Appl. Phys.*, 2006, **99**, 084302
- 31.H. Li, Y. Liang, S. Liu, F. Qiao, P. Li and C. He, *Org. Electron.*, 2019, **69**, 62-68
- 32.J.-H. Hsu, W. Choi, G. Yang and C. Yu, *Org. Electron.*, 2017, **45**, 182-189
- 33.F. Liu, X. Zhou, C. Pan and L. Wang, *J. Power Sources*, 2019, **412**, 153-159
- 34.J. Tan, Z. Chen, D. Wang, S. Qin, X. Xiao, D. Xie, D. Liu and L. Wang, *J. Mater. Chem. A*, 2019, **7**, 24982-24991
- 35.Y. Zhou, Y. Liu, X. Zhou, Y. Gao, C. Gao and L. Wang, *J. Power Sources*, 2019, **423**, 152-158
- 36.X. Yin, Y. Peng, J. Luo, X. Zhou, C. Gao, L. Wang and C. Yang, *J. Mater. Chem. A*, 2018, **6**, 8323-8330
- 37.Y. Zhou, X. Yin, Y. Liu, X. Zhou, T. Wan, S. Wang, C. Gao and L. Wang, *ACS Sustain. Chem. Eng.*, 2019, **7**, 11832-144

38. N. Feng, C. Gao, C.-Y. Guo and G. Chen, *ACS Appl. Mater. Interfaces*, 2018, **10**, 5603-5608
39. X. Li, Z. Yu, H. Zhou, F. Yang, F. Zhong, X. Mao, B. Li, H. Xin, C. Gao and L. Wang, *ACS Sustain. Chem. Eng.*, 2021, **9**, 1891-1898
40. A. Duzynska, A. Taube, K. Korona, J. Judek and M. Zdrojek, *Appl. Phys. Lett.*, 2015, **106**, 183108.
41. T. Ma, Z. Liu, J. Wen, Y. Gao, X. Ren, H. Chen, C. Jin, X.-L. Ma, N. Xu and H.-M. Cheng, *Nat. Commun.*, 2017, **8**, 1-9
42. J. Hone, M. Whitney, C. Piskoti and A. Zettl, *Phys. Rev. B*, 1999, **59**, R2514
43. C. Bounioux, P. Díaz-Chao, M. Campoy-Quiles, M. S. Martín-González, A. R. Goni, R. Yerushalmi-Rozen and C. Müller, *Energy Environ. Sci.*, 2013, **6**, 918-925.
44. W. Huang, F. Toshimitsu, K. Ozono, M. Matsumoto, A. Borah, Y. Motoishi, K.-H. Park, J.-W. Jang and T. Fujigaya, *Chem. Commun.*, 2019, **55**, 2636-2639.

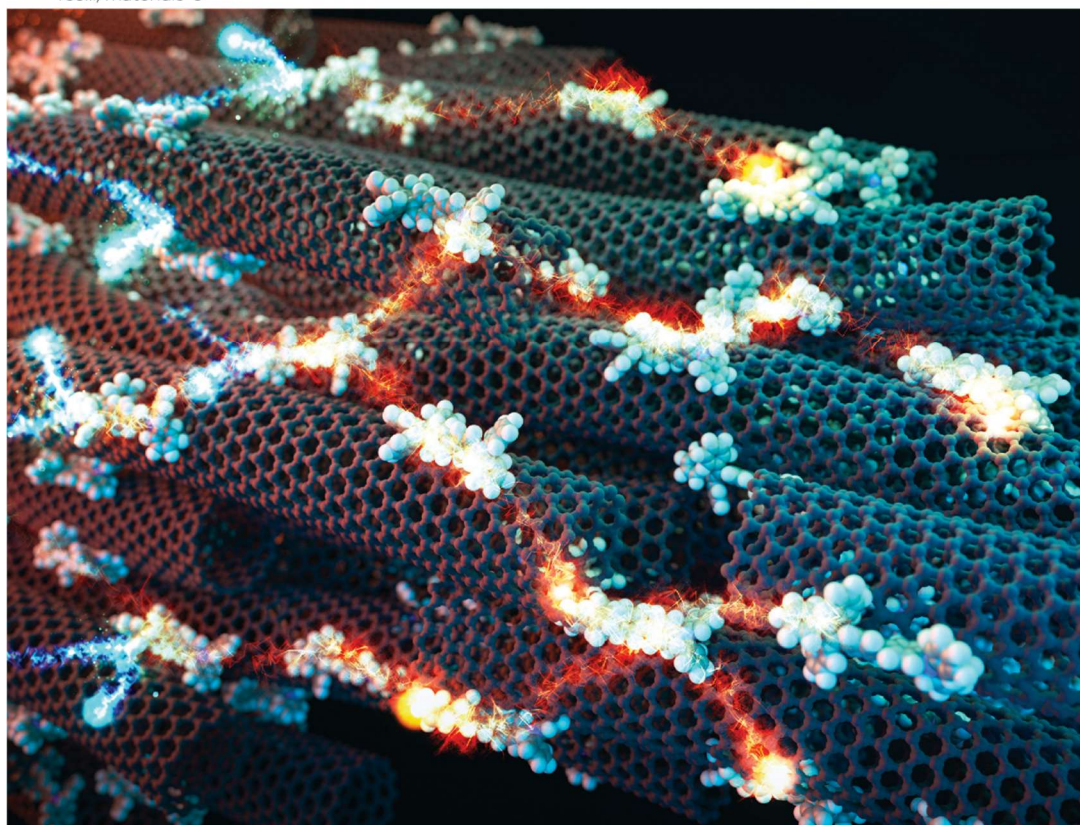
45.Q. Jiang, X. Lan, C. Liu, H. Shi, Z. Zhu, F. Zhao, J. Xu and
F. Jiang, *Mater. Chem. Front.*, 2018, **2**, 679-685.

Volume 9
Number 27
21 July 2021
Pages 8361–8706

Journal of Materials Chemistry C

Materials for optical, magnetic and electronic devices

rsc.li/materials-c



ISSN 2050-7526



COMMUNICATION

Sung Hyun Kim, Jong-In Hong *et al.*
Twisted small organic molecules for high thermoelectric performance of single-walled carbon nanotubes/small organic molecule hybrids through mild charge transfer interactions

3.3 Effect of covalent functionalizing on CNT surface in thermoelectric effect

3.3.1 Introduction

Thermoelectric generators (TEGs) have some advantages compared to other energy harvesting or recycling technologies like solar cells and wind power. First, TEGs require only a temperature difference without any other spatial occupancy, environmental conditions. It implies that TEGs can apply to anywhere with localized heat energy, even underground, where light cannot reach or closed area, where there is not enough wind force. Second, TEGs directly convert thermal energy to electrical energy. It means TEGs can recycle waste heat into usable energy. For example, combustion engines produce mechanical power, including excess waste heat. This heat flows away into the environment without any role. However, TEGs can harvest waste heat into storable and useful electrical energy.

Generally, the effectiveness of TEGs are showed in the figure of

merit, $zT = \sigma S^2 T / \kappa$, S is the Seebeck coefficient, which called thermopower ($V \cdot K^{-1}$), σ is the electrical conductivity ($\Omega^{-1} m^{-1}$), T is the absolute temperature (K), and κ is the thermal conductivity ($W \cdot m^{-1} K^{-1}$). Especially, σS^2 is called the power factor, and it is another effectiveness index for TEGs when thermal conductivity is not available to measure, especially like the thin film, which is not firm to stand-alone without substrate. Similar to this work, many kinds of research¹ on organic or organic hybrid TEGs, which are based on non-polymeric organic material, have difficulties for measuring its thermal conductivity, and they used the power factor as an effectiveness index instead of zT .²⁻⁶

The hybridization of SWCNTs with organic materials attracts attention in organic electronics due to its high electrical conductivity compared to organic materials.⁷⁻¹⁰ Furthermore, in respect of thermoelectric, SWCNTs also have a lower Seebeck coefficient than organic materials. Therefore, hybridizing with organic materials which have a higher Seebeck coefficient and a lower electrical conductivity than SWCNTs will modulate the

Seebeck coefficient and the electrical conductivity to enhance the thermoelectric performance of them.

As mentioned previously, the power factor on TEGs has two parameters (the electrical conductivity, the Seebeck coefficient). We can improve the power factor by increasing the electrical conductivity or the Seebeck coefficient of TEGs. In inorganic TEGs, several reports improve the Seebeck coefficient through the energy filtering effect^{11,12}, which improves the Seebeck coefficient with a little decreased electrical conductivity.

We previously reported the effect of the energy barrier difference between SWCNTs and organic materials on the energy filtering effect.¹³ And in previous section, we shows the relationships between electron flow pathway and energy filtering effect. In this study, we tried to directly enforce electron flow pathway with covalent bond for enhancing the Seebeck coefficient and power factor.

3.3.2 Experimental methods

Materials

All chemicals, such as 2,5-dibromothiophene, 2-bromo-3-hexylthiophene and tetrahydrofuran (THF) were supplied by Alfa Aesar, Toyko Chemical Industry (TCI), Sigma-Aldrich, and Samchun Co. Multi-walled carbon nanotubes (MWCNTs, CNT MR99) powder was purchased from Carbon Nano-material Technology Co. Ltd (Korea).

Instruments

Raman spectra of MWCNTs and MWCNTs/small organic molecules were obtained using a Renishaw Invia Raman spectrometer with an Nd:YAG laser ($\lambda = 532$ nm). Keithley 6485 picoammeter, a Keithley 2182A nano voltmeter, Keithley 2604B and Keithley 2700 multimeter system were used for measuring thermoelectric performance.

Preparation of MWCNTs and MWCNTs/organic composite films

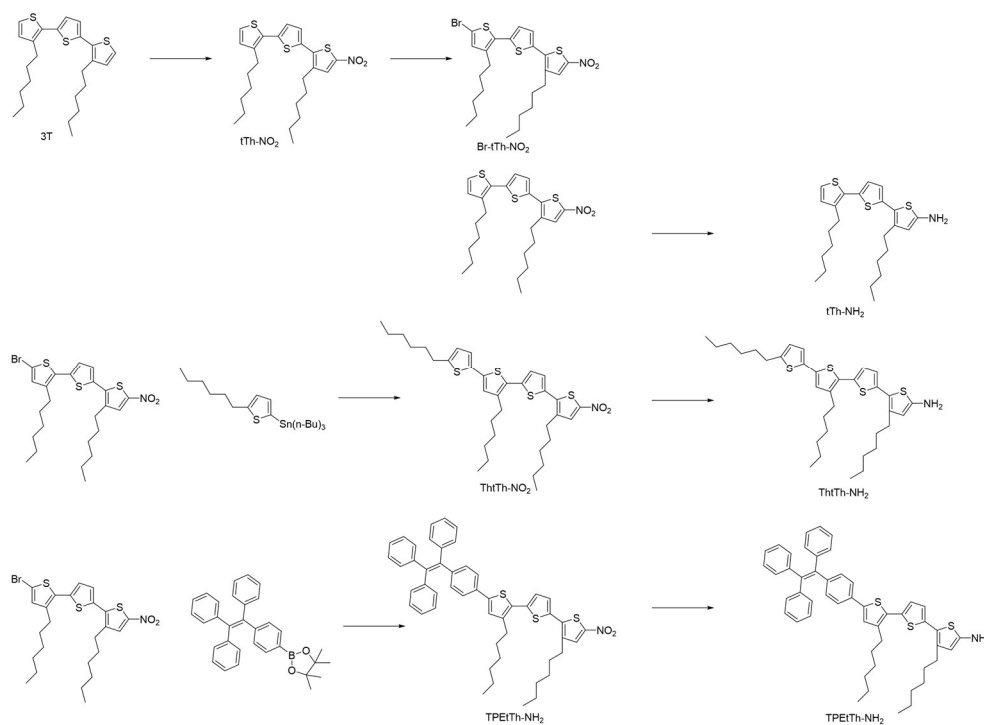
MWCNTs powder (20 mg) was added into THF (20 ml) solution and stirred under r.t. for 2 hours. Sequentially, the MWCNTs/small

organic molecule was mixed using a shaker (with 100 rpm) for 3 hours. The glass substrate ($20 \times 20 \times 7$ mm) was washed with distilled H₂O and isopropyl alcohol (IPA) for 15 min into a bath-type sonicator (Branson 5510), respectively, and dried in a vacuum oven for 12 hours. The solution (1 mL) MWCNTs (or MWCNTs/small organic molecules) was dropped on the UV/ozone cleaned glass and annealed for 30 min under 120 °C.

Measurement of thermoelectric properties

We gave the temperature difference of 2, 4, 6, and 8 K to the composite films with two sheets of the Peltier device controlled by Keithley 2604B as the power source and the source meter. We measured the temperature of the sample's surface with the Keithley 2700 multimeter system. For the precise value of the potential difference between two electrodes on the sample and current, we utilized Keithley 6485 picoammeter and a Keithley 2182A nano voltmeter.

Synthesis



Scheme 3.3.1 Synthesis of tTh-NH₂, ThtTh-NH₂, and TPEtTh-NH₂

3T was synthesized according to known Suzuki reaction.¹⁴

tTh-NO₂ 3T (300 mg, 0.72 mmol) is solved in 10 ml of MC solution and 10 ml of acetic anhydride at cooled to 0°C. 450 μ l of acetic acid 10 : nitric acid 1 solution was added and stirred overnight. Reaction was quenched with distilled water and crude product was purified with chromatography. Finally, tTh-NO₂ (309

mg, 93%) was gained.

Br-tTh-NO₂ tTh-NO₂ (96 mg, 0.20 mmol) is solved in 1 ml of THF solution. NBS (41 mg, 0.229 mmol) is added to THF solution. Reaction mixture is vigorously stirred during 2 h. Product (110 mg, 97%) is gained after purification through column chromatography.

ThtTh-NO₂ Br-tTh-NO₂ (50 mg, 0.009 mmol) and 2-hexyl-5-tributylstannyl thiophene (50 mg, 0.11 mmol) is solved in 100 ml of toluene. Pd(PPh₃)₄ (5 mg, 0.005 mmol) was added to solution. Reaction pot is refluxed during overnight. Product (58 mg, 86%) is gained after column chromatography.

TPEtTh-NO₂ TPE-boronic acid pinacol ester (51 mg, 0.111 mmol) and Br-tTh-NO₂ (50 mg, 0.09 mmol) is solved in 100 ml of THF. Pd(PPh₃)₄ (5 mg, 0.005 mmol) and potassium bicarbonate (37 mg, 0.444 mmol) was added to solution. Reaction pot is refluxed during overnight. Product (30 mg, 41%) is gained after column chromatography.

tTh-NH₂, **ThtTh-NH₂**, **TPEtTh-NH₂** was synthesized according to reference 16 and its crude product is directly used.

3.3.3 Results and discussion

Thermoelectric devices were fabricated as procedure written in experimental section and measured. Figure 3.3.1 shows the thermoelectric performance of MWCNT/organic material composite film.

In Figure 3.3.1, the Seebeck coefficient decreased with an increased ratio of organic materials which have primary amine as an end group. It is expected result which implies that the primary amine group acts as a negative dopant. There almost no difference between **tTh-NH₂**, **ThtTh-NH₂**, and **TPEtTh-NH₂** on the Seebeck coefficient and electrical conductivity, but **tTh-NH₂** shows a slightly larger decrement of the Seebeck coefficient and increment of electrical conductivity in doped condition. It seems the result of small steric hindrance and molecular weight of **tTh-NH₂**.

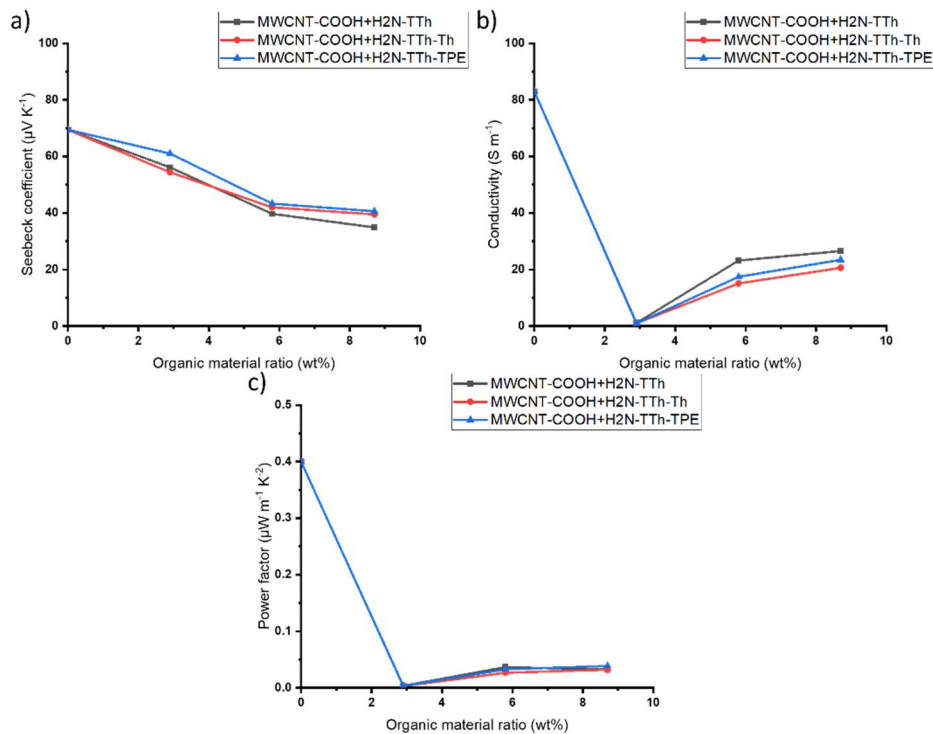


Figure 3.3.1 The thermoelectric properties of pure MWCNTs and MWCNT/organic material composite film vary with the organic material blend ratio in the composite films. a) the Seebeck coefficient, b) the electrical conductivity, and c) the power factor.

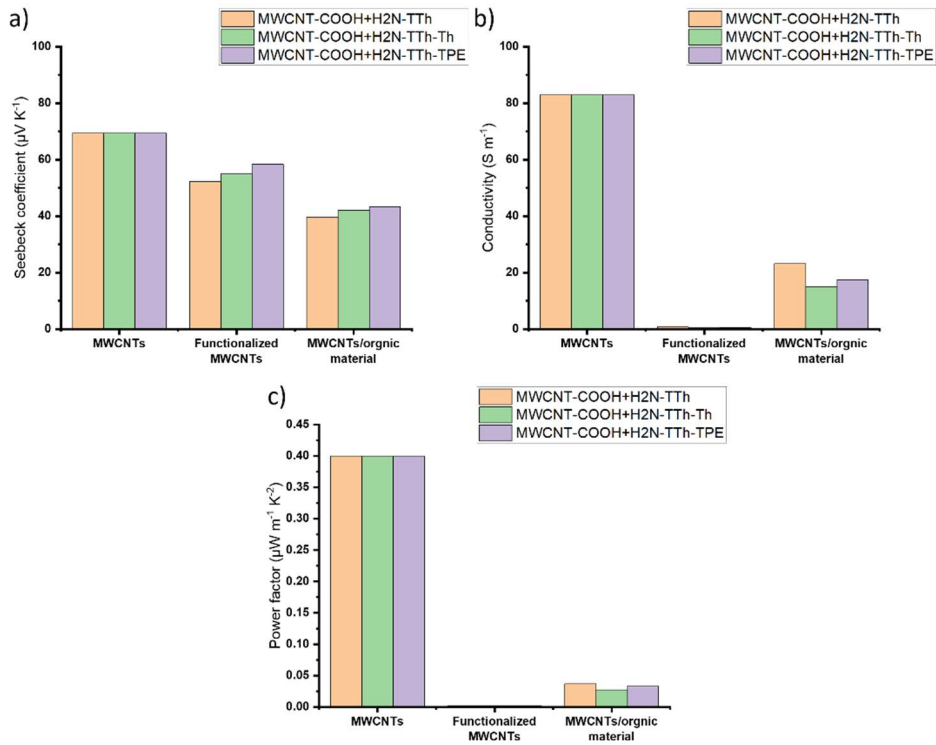


Figure 3.3.2 The thermoelectric properties of pure MWCNTs, functionalized MWCNTs, and MWCNT/organic material composite film. a) the Seebeck coefficient, b) the electrical conductivity, and c) the power factor.

We expected that the case of covalently bonded materials shows an increment in the Seebeck coefficient and suppressed decrement in electrical conductivity. However, the case of covalently bonded materials exhibit dramatically decreased electrical conductivity and suppressed decrement in the Seebeck coefficient, shown in

Figure 3.3.2. To explain this phenomenon, we calculate weighted mobility using Eq. 3.3.1.¹⁵

$$\mu_w = \frac{3h^3\sigma}{8\pi e(2m_e k_B T)^{3/2}} \left[\frac{\exp\left[\frac{|S|}{k_B/e} - 2\right]}{1 + \exp\left[-5\left(\frac{|S|}{k_B/e} - 1\right)\right]} + \frac{\frac{3}{\pi^2} \frac{|S|}{k_B/e}}{1 + \exp\left[5\left(\frac{|S|}{k_B/e} - 1\right)\right]} \right]$$

Eq 3.3.1 Weighted mobility equation. S is the Seebeck coefficient, k_B is Boltzmann constant, h is Planck constant, σ is electrical conductivity.

	Weighted mobility (cm ² V ⁻¹ s ⁻¹)	Carrier concentration (cm ⁻³)
MWCNT	0.049	1.09 × 10 ²⁰
MWCNT-TTh	0.025	8.34 × 10 ¹⁹
MWCNT-TTh-Th	0.010	9.62 × 10 ¹⁹
MWCNT-TTh-TPE	0.024	1.04 × 10 ²⁰
MWCNT+H2N-TTh	0.034	1.49 × 10 ²⁰
MWCNT+H2N-TTh-Th	0.028	1.39 × 10 ²⁰
MWCNT+H2N-TTh-TPE	0.024	1.30 × 10 ²⁰

Table 3.3.1 Calculated weighted mobility and carrier concentration.

MWCNT/organic material composite shows increased carrier concentrations as molecular weight and decreased carrier mobilities as a steric hindrance of organic material. It means carrier concentration affected by organic material's primary amine

group as a negative dopant. However, the case of covalently bonded materials shows a different trend. Carrier concentration is increased by organic material's conjugation length and carrier mobility is dramatically decreased only when the organic material have an alkyl chain end group. It implies that covalently bonded material transfer electrons through covalent bond and covalently bonded organic material act as an energy filter. However, despite the controlled electron flow pathway, lowered Seebeck coefficient implies that the negative doping effect of secondary amine is larger than the energy filtering effect of organic material.

3.3.4 Conclusion

Covalently bonded compounds enable controlling of the electron transfer pathway. However, the amide group between CNTs and organic semiconductor materials disturbs electron flows between CNTs and organic semiconductor materials and lowers the Seebeck coefficient with negative doping.

This study reveals that the amide bond with relatively large

electron density is not appropriate for increasing the Seebeck coefficient in covalently bonded CNTs/organic semiconductor hybrid materials.

3.3.5 References and notes

1. Lindorf, M. et al. Organic-based thermoelectrics. *J Mater Chem A* 8, 7495–7507 (2020).
2. An, C. J., Kang, Y. H., Song, H., Jeong, Y. & Cho, S. Y. High-performance flexible thermoelectric generator by control of electronic structure of directly spun carbon nanotube webs with various molecular dopants. *J Mater Chem A* 5, 15631–15639 (2017).
3. Wan, C. et al. Flexible n-type thermoelectric materials by organic intercalation of layered transition metal dichalcogenide TiS_2 . *Nat Mater* 14, 622–627 (2015).
4. Yao, Q., Wang, Q., Wang, L. & Chen, L. Abnormally enhanced thermoelectric transport properties of SWNT/PANI hybrid films by the strengthened PANI molecular ordering. *Energ*

- Environ Sci 7, 3801–3807 (2014).
5. Cho, C. et al. Completely Organic Multilayer Thin Film with Thermoelectric Power Factor Rivaling Inorganic Tellurides. *Adv Mater* 27, 2996–3001 (2015).
 6. Park, T., Park, C., Kim, B., Shin, H. & Kim, E. Flexible PEDOT electrodes with large thermoelectric power factors to generate electricity by the touch of fingertips. *Energ Environ Sci* 6, 788–792 (2013).
 7. Nakai, Y. et al. Giant Seebeck coefficient in semiconducting single-wall carbon nanotube film. *Appl Phys Express* 7, 025103 (2014).
 8. Zhao, W. et al. Flexible carbon nanotube papers with improved thermoelectric properties. *Energ Environ Sci* 5, 5364–5369 (2011).
 9. Jiang, Q. et al. High-performance hybrid organic thermoelectric SWNTs/PEDOT:PSS thin-films for energy harvesting. *Mater Chem Frontiers* 2, 679–685 (2018).
 10. Toshima, N. et al. Novel Hybrid Organic Thermoelectric Materials: Three-Component Hybrid Films Consisting of a

Nanoparticle Polymer Complex, Carbon Nanotubes, and Vinyl Polymer. *Advanced Materials* 27, 2246–2251 (2015).

11. B. Paul, A. K. V and P. Banerji, *J Appl Phys*, 2010, 108, 064322.
12. A. Pakdel, Q. Guo, V. Nicolosi and T. Mori, *J Mater Chem A*, 2018, 6, 21341–21349.
13. Kim, T., Jang, J. G. & Hong, J.-I. Enhanced thermoelectric performance of SWNT/organic small molecule (OSM) hybrid materials by tuning of the energy level of OSMs. *J Mater Chem C* 8, 12795–12799 (2020).
14. J-I Hong et al. Effect of the π -linker on the performance of organic photovoltaic devices based on push-pull D- π -A molecules, *New J. Chem.*, 42, 11458-11464 (2018)
15. G. J. Snyder et al., Weighted Mobility, *Adv. Mater.*, 32, 2001537 (2020)
16. Y. Chen et al., Synthesis, characterization and optical limiting property of covalently oligothiophene-functionalized graphene material, *Carbon*, 47(13), 3113-3121 (2009)

국문 초록

에너지 수확을 위한 유기 반도체

물질의 활용

유기반도체는 저렴한 제작 공정 비용, 다양한 구조를 위한 변형의 용이함과 합성물의 균일성 등의 특성으로 인해 지난 수십년간 무기반도체와 함께 다양한 연구가 이루어져왔다. 본 논문에서는 이러한 유기반도체의 활용 중에서 재생가능한 에너지원으로서 활용할 수 있는 유기태양전지와 유기열전소자에 사용되는 유기반도체 물질과 그 소자에 관한 연구를 다루고 있다.

1장에서는 재생가능한 에너지의 개발 필요와 태양전지를 제외한 주요 재생가능한 에너지의 추세를 간략히 서술하였다.

2장에서는 유기태양전지용 유기반도체 물질에 대하여 고찰하였다. 첫 번째 부분에서는 유기태양전지에 대한 배

경을 서술하였다. 유기태양전지의 구동 메카니즘과 각 단계에 영향을 주는 요인과 이를 조절하는 방법과 이유를 서술하였다. 또한 유기태양전지의 효율과 특성의 측정방법 및 해석에 대하여 다루고 있다. 두 번째 부분에서는 광자-전자 변환 효율을 높이기 위해 전자 주개-전자 받개-전자 주개 구조로 유기반도체 물질이 보다 많은 광자를 흡수할 수 있도록 하며 원활한 전자 전달을 위하여 분자간 상호작용이 잘 일어나도록 전체적으로 평탄한 구조의 물질에 대하여 연구하였다. 세 번째 부분에서는 전기장을 활용하여 유기태양전지를 구성하는 활성층의 내부 배열을 조절하여 보다 원활한 엑시톤의 분리와 전자 전달을 이루고자 하였다. 이에 쌍극자 모멘트가 큰 물질을 설계하여 사용하였고 전기장에 의해 유기반도체 물질의 배열이 변함을 확인하였다. 하지만 자유롭게 움직일 수 있는 단분자 물질의 특성으로 인해 전기장에 의한 변화가 활성층 내의 상분리를 제어할 수 없어 유기단분자 용액공

정에서는 적합하지 않음을 발견하였다.

3장에서는 유기열전소자용 탄소나노튜브와 유기반도체 물질의 하이브리드 필름에 대하여 연구하였다. 첫 번째 부분에서는 열전 효과의 배경과 열전 효과의 향상을 위해 주로 사용되는 현상인 에너지 필터링 효과와 유기열전소자의 연구 경향에 대하여 간략하게 서술하였다. 두 번째 부분에서는 유기반도체 물질에 따른 탄소나노튜브-유기반도체 하이브리드 필름에서의 제베크 계수(Seebeck coefficient)와 전기 전도도(electrical conductivity), 역률(power factor)의 변화를 연구하였다. 탄소나노튜브-유기반도체 하이브리드 필름에서는 유기반도체 물질의 형상과 탄소나노튜브와의 상호작용이 제베크 계수 등에 중요한 영향을 미치는 것을 확인하였다. 특히 탄소나노튜브와 유기반도체의 상호작용이 강한 경우, 소자의 전자 전달 경로에 큰 영향을 줄 수 있기 때문에 탄소나노튜브와 유기반도체의 상호작용이 약한 경우에 비하여 약 2배의 제베크

크 계수($157 \mu\text{V}\cdot\text{K}^{-1}$)와 역률($539.8 \mu\text{W}\cdot\text{K}^{-2}\cdot\text{m}^{-1}$)을 나타내었다. 세 번째 부분에서는 유기반도체 물질이 탄소나노튜브에 결합하는 방식에 따라 제베크 계수와 전기 전도도, 역률에 미치는 영향에 대해서 연구하였다. 유기반도체의 1차 아민기와 탄소나노튜브의 카복실기를 아미드기의 공유결합으로 연결한 화합물과 유기반도체와 탄소나노튜브의 혼합물과 비교하였다. 탄소나노튜브와 유기반도체를 공유 결합으로 연결하는 것으로 전자 수송 경로를 제어하는 것은 달성하였으나, 아미드 결합으로 인해 제베크 계수가 오히려 감소하게 되었다. 이에 탄소 물질과 유기반도체를 공유결합으로 연결하여 제베크 계수를 향상시키기 위해서는 탄소 물질과 유기반도체를 이어주는 구조로 아미드 결합과 같은 전자가 다소 풍부한 구조가 적합하지 않음을 알 수 있었다.

Keywords : 에너지 수확, 열전 발전기, 태양전지, 유기반도체

학 번 : 2011-20304